

SEGMENTATION AND DETECTION OF ABNORMALITIES IN BRAIN MR IMAGES

Ph.D. THESIS

by

SWETA TRIPATHI



**DEPARTMENT OF ELECTRICAL ENGINEERING
INDIAN INSTITUTE OF TECHNOLOGY ROORKEE
ROORKEE-247667 (INDIA)
OCTOBER, 2018**

SEGMENTATION AND DETECTION OF ABNORMALITIES IN BRAIN MR IMAGES

A THESIS

*Submitted in partial fulfilment of the
requirements for the award of the degree*

of

DOCTOR OF PHILOSOPHY

in

ELECTRICAL ENGINEERING

by

SWETA TRIPATHI



**DEPARTMENT OF ELECTRICAL ENGINEERING
INDIAN INSTITUTE OF TECHNOLOGY ROORKEE
ROORKEE-247667 (INDIA)
OCTOBER, 2018**

**©INDIAN INSTITUTE OF TECHNOLOGY ROORKEE, ROORKEE-2018
ALL RIGHTS RESERVED**



INDIAN INSTITUTE OF TECHNOLOGY ROORKEE ROORKEE

CANDIDATE'S DECLARATION

I hereby certify that the work which is being presented in the thesis entitled “**SEGMENTATION AND DETECTION OF ABNORMALITIES IN BRAIN MR IMAGES**” in partial fulfilment of the requirements for the award of the Degree of Doctor of Philosophy and submitted in the Department of Electrical Engineering of the Indian Institute of Technology Roorkee, Roorkee is an authentic record of my own work carried out during a period from July, 2011 to October, 2018 under the supervision of Dr. R. S. Anand, Professor and Dr. E. Fernandez, Associate Professor, Department of Electrical Engineering, Indian Institute of Technology Roorkee, Roorkee.

The matter presented in this thesis has not been submitted by me for the award of any other degree of this or any other Institute.

(**SWETA TRIPATHI**)

This is to certify that the above statement made by the candidate is correct to the best of our knowledge.

(R. S. Anand)
Supervisor

(E. Fernandez)
Supervisor

Date: _____

The Ph.D. Viva-Voce Examination of **Ms. Sweta Tripathi**, Research Scholar, has been held on.....

Chairman, SRC

Signature of External Examiner

This is to certify that the student has made all the corrections in the thesis.

Signature of Supervisor(s)

Head of the Department

ABSTRACT

Magnetic Resonance Imaging (MRI) technique is a non-invasive diagnostic tool which plays a crucial role in the main stream of anatomical studies and pathological planning of brain abnormalities when compared to other available techniques like Computed Tomography (CT), because of its excellent soft tissue contrast and multi-planer acquisition capabilities. It is the best neuro-imaging tool for in vivo projections of structural aberrations like diffused brain differences, structural alterations etc. It is used for visualization and quantitative analysis of the area inside the tissue. Brain Hemorrhage, Brain Infarction and Brain Tumor are the most common brain deformities, leading to high morbidity and mortality worldwide. Albeit, multitude MRI pulse sequences are there (like T1, T2, proton density, FLAIR, DWI, ADC, FAT saturation etc.) each of them keeping their unique characteristic to discern tissue composition but the basic MR sequences namely T1-weighted, T2-weighted and DWI furnish relevant texture and intensity information of Hemorrhage, Infarct and Tumors. The lesion may have homogeneous or heterogeneous texture, both having different signal characteristics i.e. hypointensity, hyperintensity or isointensity. Lesions are characterized in accordance to their location and aetiology (underlying causes). The T1 and T2 characteristics of the phases of hemorrhage and infarction namely Early Hyperacute, Late Hyperacute, Acute, Subacute and Chronic are different depending on the aging of hematoma with time. Also, the degree of enhancement of tumors for the same class and for different class of tumor depends on MR acquisition and its morphology. Any diminutive change resulting from any kind of disease or insult can cause serious further implications. Compression or dilation from the normal anatomy due to accumulation of blood or due to necrosis by the disruption of atrioventricular blood flow, leads to cerebrovascular problems. So, the pulse sequences (T1-weighted, T2-weighted, DWI etc.) are considered in order to get information about parenchymal issues such as: obliteration of the gyri-sulci pattern, asymmetry, abnormal distinction between gray-white matter, hyper/hypo dense abnormalities in brain parenchyma, hydrocephalus or intraventricular blood in ventricular system, extra cranial soft tissue swelling, fracture, normal air content of the sinuses and the mastoid in bone.

Segmentation of abnormalities in brain MR images is a crucial step for surgical and treatment planning. There are various methods reported in literature for segmentation and classification of brain lesions on brain MR image. Segmentation procedure focused either on similarity criterion like thresholding, watershed, Region Growing, and region splitting and merging or on discontinuity criterion like edge-based methods. In another kind of spatially guided approach where spatial relationship between pixels is used for segmentation are region

(like region growing, split and merge, hybrid growing merging) and energy-based techniques (like active contour, graph based, watershed, marker-based watershed). The level set formulation of the active contour model is further categorized as region-based approach and edge-based approach. Besides edge-based active contour models, region-based models try to detect every region of interest (ROI) in the given image by combining the region-based information into their energy functional. In literature, these models have been found to be superior than the edge-based active contour models because of their unrestricted position of the initial contour and automatic detection of estimated boundaries. Also, these models have shown effective reasonable segmentation because of global energy minimization based on the statistical properties inside and outside the evolving contour which provide driving force during the evolution of the deformable shapes and keeps the regularity of the active contour. The methods reported in literature namely Chan- Vese (CV), Region Scalable Fitting (RSF) and Local Gaussian Distribution Fitting (LGDF) are region-based active contour method. The CV model provides better performance than the previous models because of its nature to acquire a large convergence rate. Though, image segmentation using the CV model depends on the placement of initial contour, Region Scalable Fitting (RSF) energy function obtains information relating to intensity of the local regions at an established scale in order to estimate the two fitting functions and forces the curve towards the calculated contour of the object. The regularity term available in this model is used to control the length of the object boundaries and prevents the over-segmentation. In LGDF model, the local image intensities are described by gaussian distributions with different means and variances where circular initial level set function is used which then evolve to the object boundary. Above discussed methods are sensitive to initialization of contour and noise.

Image features are useful in identification, representation and description purpose. Several researchers in past have given the methods of texture feature extraction from various medical image datasets. Intensity Based Features (IBF), Gray Level Difference Matrix(GLDM), Laplacian of Gaussian Features (LoG), Rotation Invariant Circular Gabor Features (RICGF), Rotation Invariant Local Binary Patterns (RILBP), Gray Level Difference Statistics (GLDS), Neighbourhood Gray Tone Difference Matrix (NGTDM), Laws Textures Energy Measure (Laws TEM), Fractal Dimension Texture Analysis (FDTA), Statistical Feature Matrix (SFM), Fourier Power Spectrum (FPS), Local Binary Pattern (LBP) and Gaussian Pyramid based Local Binary Pattern (GPLBP) are mostly used feature extraction techniques applied in classification of input dataset into two class or multiclass objects.

As dimensionality of the feature set increases, the amount of data needed to give reliable analysis grows exponentially. Feature selection is essentially helpful in dealing over-fitting problem and in reducing the training time. Many methods are reported in literature for feature reduction for instance Principal Component Analysis (PCA), Linear Discriminant Analysis (LDA), Minimum Redundancy Maximum Relevance (mRMR) and Locally Linear Embedding (LLE). These are used to select most relevant attribute to form an optimal subset from the original feature pool.

Final diagnosis of lesion is done through classification models. There are many methods available in the literature for detection of normal and abnormal brain as well as for multiclass classification of lesions using MR images. It has been recognized and emphasized time and again that early and correct classification of pathology can reduce casualty in emergency conditions. The multiclass classification studies reported in literature are based on Support Vector Machine (SVM), Deep Neural Network (DNN), Artificial Neural Networks (ANN), or hybrid methods using Genetic Algorithms (GA) like GA-ANN, GA-SVM.

Although MR images of brain furnishes evident visualization of the brain anatomy, the insight picture details such as detection of lesion is not very clear or definite. Consequent problems arising during the identification of lesion on MR images are: artifacts developed due to change in its orientation relative to patient posture, inadequate segmentation of homogeneous, heterogeneous, diffused lesion bearing weak or false edges and classification of lesion; have to be dealt. For that purpose, this research work is basically directed to develop a CAD system constituting segmentation and classification algorithms for identification of abnormality on brain MR images, thereby, aiding the radiologist in decision making process. In this research work two major objectives have been considered:

The first objective of this research is to develop a method for segmentation of MR images to extract region of interest (ROI).

The second objective is to develop a classification scheme based on artificial intelligence techniques for diagnosing critical MR brain abnormalities like Brain Hemorrhage, Infarct and Tumor, which are leading causes of rising incidence in mortality among adults and children.

In order to achieve the first objective of the present work, Modified Region Based Active Contour (MRBAC) is proposed to delineate region of interest in brain MR images. The proposed method utilizes the advantages of Local Gaussian Distribution Fitting (LGDF) energy model along with coping up with the difficulties handled by the method. The performance of conventional active contour method relies on factors such as: appropriate and accurate contour

initialization, presence of intensity inhomogeneities and weak boundaries, sensitivity to noise and optimal configuration of contour propagation controlling parameters. Although LGDF method can discern well between two similar intensity regions; however, if the contour initialization is not accurate enough it can introduce many local minima resulting in improper segmentation. The proposed method is based on the LGDF method with the variation at the initialization step so that it does not get trapped at local minimum. Here, contour of specified shape (circular or rectangular) has not been taken but of optimal shape which is user defined has been used and it is said to be as zero level set. This reduces the number of iterations resulting in reduction of computational cost of the system.

The developed MRBAC method is tested on 118 images out of which 34 images are taken of brain hemorrhage, 27 images are taken of brain infarct and 57 images are taken of brain tumor. Different performance metrics such as True Positive, False Positive, Accuracy, Jaccard Similarity Index, Dice Coefficient and Hausdorff Distance are computed for quantitative analysis. Accuracy is the proportion of pixel contained within the correctly extracted regions obtained by the test methods out of all the pixels of manually delineated region. DC and JSI are the similarity matrices and their values should be higher. HD values are used to measure the structural difference between the two objects and its value should be low signifying better segmentation. It has been observed that the result of the proposed segmentation provides higher segmentation accuracy in all the three abnormalities when compared with other state of the art methods like Region Growing and Distance Regularized Level Set Evolution (DRLSE) segmentation methods. It also provides better values of other averaged performance measures such as JSI, DC and HD.

In order to achieve the second objective of the present work, Pattern Recognition tool in Neural Network (NN) Toolbox (of MATLAB®) has been used for the classification of selected anomalies from MRI image of the brain. In this work, two different classifiers named as Fusion Network are proposed: first one is for two class classification of data into normal and pathological brain and second one is for multiclass classification of data into Normal, Tumor, Hemorrhage and Infarct brain abnormalities in MR images.

For first classifier model, input samples of 488 images (230 normal brain, 258 pathological brain MRI) are taken. To classify these samples into normal and pathological brain, total 1861 features have been calculated. These features include 5 First Order Statistical features, 26 Haralick Spatial Gray Level Dependence Matrices (SGLDM) features, 4 Gray Level Difference Statistics (GLDS), 5 Neighbourhood Gray Tone Difference Matrix (NGTDM), 4 Statistical Feature Matrix (SFM), 6 Laws Texture Energy Measures (TEM), 4 Fractal Dimension

Texture Analysis (FDTA), 2 Fourier Power Spectrum (FPS), 361 Local Binary Pattern and its variants (LBP^{u2} , LBP^{ri} , LBP^{riu2}) and 1444 Gaussian Pyramid based Local Binary Pattern with its variants (LBP^{u2} , LBP^{ri} , LBP^{riu2}). Dimensionality of these features is reduced to 500 from 1861 by using Minimum Redundancy Maximum Relevance (mRMR) method which assigns rank to each feature according to its relevance in classification between different class. Original dataset of 488 images is divided into two parts one is training data (TR data) and other is testing data (TE data) in the ratio of 70% to 30% respectively. After normalization, feature set from training data is presented to ten individual two-layer feedforward neural network with 6 neurons in hidden layer having sigmoidal activation function and 2 neurons in output layer having SoftMax activation function. Same feature set is presented to proposed Fusion Network classifier which is an ensemble of all ten individual neural networks. The network is trained with scaled conjugate gradient backpropagation method. Individual as well as proposed Fusion Network Classifier is tested using 30 % of original data (TE data). The accuracy of proposed Fusion Network classifier comes out to be 94.5% for classification of normal and pathological brain.

For second classifier model, input samples of 510 images (176 Normal brain, 123 Tumor brain, 107 Hemorrhagic brain and 104 Infarct brain MRI) are taken. To classify these samples into Normal, Hemorrhage, Infarct and Tumor brain, total 1861 features have been extracted from all classes of brain MR images. Using mRMR method, these features are then reduced to 500 most relevant feature set which have important role in discriminating input data between all four class. All 510 images of dataset are partitioned in to training data (TR data) and testing data (TE data) in the same ratio as previous i.e. 70% to 30%. Feature set obtained from training data is presented to ten separate two-layer feedforward neural network with 6 neurons in hidden layer having sigmoidal activation function and 4 neurons in output layer having SoftMax activation function. Same feature set is presented to proposed Fusion Network classifier which is a combination of all ten individual neural networks. The network is trained with scaled conjugate gradient backpropagation method. All separate neural networks as well as proposed Fusion Network Classifier is tested using 30 % of TE data. The accuracy of proposed Fusion Network classifier comes out to be 92.8% for multiclass classification of Normal, Tumor, Hemorrhage and Infarct brain MR images.

ACKNOWLEDGEMENT

I express my sincere gratitude to my supervisors Dr. R.S. Anand, Professor and Dr. E. Fernandez, Associate Professor, Department of Electrical Engineering, Indian Institute of Technology Roorkee, Roorkee, India for their guidance and suggestions of this study. I am extremely privileged to have such supervisors who are always ready to support me for everything all along the completion of my Ph.D. They will always be my motivation throughout my life.

I wish to sincerely acknowledge the contributions of Dr. Harish Bhatia, Director and Mr. Fredrick Singh, Senior MRI Technician DOON MRI & Diagnostic, for their constructive suggestions and guidance during the course of work. I am indebted by their help as the data base provided by them, was the basic raw material for my present thesis work.

A special thanks to Dr. Karan Singh, Dev Hospital, Roorkee for his unconditional motivation and selfless support at all times.

I express my sincere thanks to the members of my research committee, Dr. G. N. Pillai, Dr. Indra Gupta and Dr. Manoj Mishra for their valuable suggestions during the constructive discussions. Special thanks to Dr. Vinod Kumar, Dr. Sharmili Das, Dr. Ambalika Sharma, Prof. M. K. Vasanta and Dr. Vinay Pant for making this research process a successful endeavor. I would like to thank Head of the Department and other faculty members of the Department of Electrical Engineering for their support and providing the excellent facilities during this research work at Indian Institute of Technology Roorkee, Roorkee.

I was blessed with a lot of sincere and caring friends who play a major role in boosting my morale during the lows. I would give a special acknowledgement and thanks to my fellow researchers namely Dr. Deep Gupta, Dr. Arun Balodi, Dr. Nishant Jain, Mr. Yogesh Sariya, Ms. Smita Mondal and Dr. Priyanka Singh whose devotion, sincerity and work ethics were commendable. I also sincerely acknowledge research aid provided in form MHRD scholarship and assistantship by Department of higher education, Ministry of Human Resource Development, Government of India.

I have special thanks for Mr. Souri Sengupta, Registrar, Amity University Haryana who steered my path with intellectual as well as emotional support all throughout my journey.

I am extremely thankful to Mr. Hemant Dev Mishra, Research Lead- Evalueserve. and Mrs. Sumedha Tripathi, Joint Manager- Suez India Pvt Ltd for unconditional support during the course of work.

I am grateful to my parents Shri S. R. Tripathi and Smt. Pushpa Tripathi and my younger brothers Mansagar Tripathi and Aditya Narayan Tripathi who have provided me moral and emotional support throughout this period. I am also grateful to my husband Mr. Manoj Pandey and other family members and friends who have supported me along the way. A sincere thanks to my adorable daughter Nitya, who patiently bore the pain of separation from the parent during the course of my work.

Finally, I am thankful to all merciful almighty who bestowed his wisdom and blessings all throughout my research work.

(Sweta Tripathi)

TABLE OF CONTENTS

Abstract	i
Acknowledgement	vii
List of Figures	xiii
List of Tables	xv
List of Abbreviations	xvii
INTRODUCTION	1
1.1 Background	1
1.2 Medical Imaging Modalities: A Brief Overview	1
1.3 Magnetic Resonance Imaging (MRI)	3
1.3.1 MRI Suite.....	3
1.3.2 Types of Sequence and its Reading.....	6
1.3.3 Safety and Precautionary Aspects.....	7
1.4 Medical Conditions in Brain:	
Study of Three Common Diseases under MR Imaging	8
1.4.1 Brain Hemorrhage on Magnetic Resonance (MR) Images.....	8
1.4.2 Types of Hemorrhage.....	9
1.4.3 Classification of Hemorrhage.....	9
1.4.4 Role of MR in Case of Hemorrhage.....	12
1.4.5 Mimics in Hemorrhage.....	13
1.4.6 Brain Infarction on Magnetic Resonance (MR) Images.....	13
1.4.7 Mimics in Infarct.....	15
1.4.8 Brain Tumors on Magnetic Resonance (MR) Images.....	15
1.5 Need for Abnormal MR Brain Detection	17
1.6 Need for Segmentation	17
1.7 Need of Classification	18
1.8 Organization of Thesis	19
1.9 Research Contribution	20
LITRATURE REVIEW	23
2.1 Introduction	23
2.2 Image Segmentation Methods	23
2.3 Feature Extraction Methods	31
2.4 Feature Selection Methods	34
2.5 Classification Methods	36
2.6 Conclusion	39
2.7 Objectives of the Present Study	40
METHODOLOGY	41
3.1 Introduction	41
3.2 Acquisition of Data	41
3.2.1 Brain Image Acquisition and Assessment Criteria for DOON MRI & Diagnostic Dataset.....	43
3.2.2 Dataset Source and Details.....	44
3.3 Proposed Methodology	44

3.3.1	Modified Region Based Active Contour (MRBAC) for Morbid Brain Segmentation	44
3.3.2	Development of a Classification System for Multiclass Brain Lesion Classification	46
3.4	Conclusion	48
MODIFIED REGION BASED ACTIVE CONTOUR		49
4.1	Introduction	49
4.2	Categorization of Various Segmentation Schemes	50
4.2.1	Segmentation Based on Thresholding	51
4.2.2	Edge-Based Segmentation	51
4.2.3	Region-Based Segmentation.....	52
4.2.4	Watershed Transform-Based Segmentation	53
4.2.5	Hybrid Segmentation	54
4.3	Active Contour Based Segmentation	55
4.3.1	Parametric Active Contour Models	55
4.3.2	Geometric Active Contour Models.....	57
4.4	Edge Based Active Contour Models using DRLSE Approach	58
4.5	Region Based Active Contour Models	62
4.6	Proposed Modified Region Based Active Contour (MRBAC) Method	66
4.7	Assessment Criteria.....	70
4.7.1	True Positive (TP) Ratio.....	71
4.7.2	False Positive (FP) Ratio	71
4.7.3	Accuracy (ACC).....	71
4.7.4	Jaccard Similarity Index (JSI)	71
4.7.5	Dice Coefficient (DC)	72
4.7.6	Hausdroff Distance (HD).....	72
4.8	Experimentation	72
4.9	Results and Discussions.....	73
4.9.1	Experiment No. 1:.....	73
4.9.2	Experiment No. 2:.....	78
4.9.3	Experiment No. 3:.....	82
4.10	Conclusion	87
FEATURE EXTRACTION AND DISEASE CLASSIFICATION		89
5.1	Introduction	89
5.2	Dataset	89
5.3	Feature Extraction.....	91
5.3.1	Intensity Based Features (IBFs) or First Order Statistics Features (FOS Features).....	91
5.3.2	Spatial Gray Level Dependence Matrices Features (SGLDM features).....	93
5.3.3	Gray Level Difference Statistics Features (GLDS Features).....	95
5.3.4	Neighborhood Gray Tone Difference Matrix Features (NGTDM Features)	95
5.3.5	Statistical Feature Matrix (SFM Features).....	96
5.3.6	Laws Textures Energy Measure Features (Laws TEM Features).....	96
5.3.7	Fractal Dimension Texture Analysis (FDTA Features)	96
5.3.8	Fourier Power Spectrum Features (FPS Features).....	97
5.3.9	Local Binary Pattern Features (LBP Features)	97
5.4	Gaussian Pyramid.....	98
5.4.1	Gaussian Pyramid Based LBP Features.....	99

5.5	Feature Management and Feature Selection.....	101
5.5.1	Normalization of Calculated Features	101
5.5.2	Feature Selection	101
5.6	Lesion Classification Module.....	102
5.7	Assessment Criteria.....	103
5.8	Experimentation	105
5.9	Results and Discussions.....	106
5.9.1	Experiment No. 1:.....	106
5.9.2	Experiment No. 2:.....	109
5.10	Conclusion	112
CONCLUSIONS AND FUTURE SCOPE.....		113
6.1	Conclusions.....	113
6.2	Scope for Future Work	116
PUBLICATIONS FROM THE RESEARCH WORK		119
REFERENCES.....		121
APPENDIX.....		143

LIST OF FIGURES

Figure 1.1	Basic instrumentation of MR imaging system	4
Figure 1.2	T2 and T1-weighted MR Brain images of a patient in axial (a, b) and sagittal (c) planes respectively.	5
Figure 1.3	Comparative visual demarcation between most frequently used sequences i.e. T1, T2, FLAIR and DWI in MR Brain images of a patient. (a) Sagittal T1 for evaluating midline structures (b) Axial T1 for evaluating anatomic detail (c) axial T1 with contrast for evaluating BBB breakdown (d) Axial T2 for looking at areas of edema and pathology (e) Coronal FLAIR for evaluating edema with CSF (f) Axial DWI for stroke imaging, abscess, cellular tumors.	6
Figure 1.4	Hemorrhage (ICH) classification on the basis on site of occurrence and basis of underlying causes leading to its development.	10
Figure 1.5	MR brain Images of tumor patients in axial, sagittal and coronal planes.	16
Figure 3.1	Research methodology	42
Figure 4.1	Level set evolution and the corresponding contour propagation: (a) Topological view of level set $\emptyset(x, y)$ evolution, (b) The changes on the zero-level set $C: \emptyset(x, y) = 0$	57
Figure 4.2	Different possible cases of contour position	63
Figure 4.3	Comparative visual analysis of segmentation result of different tumor MR image obtained by (a) original image (b) ground truth marked by radiologist (c) segmented by Region Growing method (d) segmented by DRLSE method (e) segmented by proposed MRBAC method	74
Figure 4.4	Box plot of True Positive (TP), False Positive (FP), Accuracy (ACC), Jaccard Similarity Index (JSI), Dice Coefficient (DC) and Hausdorff Distance (HD) measurements of all the Tumor MR images shown in Figure 4.3 by proposed MRBAC, Region Growing and DRLSE segmentation methods	77

Figure 4.5	Comparative visual analysis of segmentation result of different Infarct MR Image obtained by (a) original image (b) ground truth marked by radiologist (c) segmented by Region Growing method (d) segmented by DRLSE method (e) segmented by proposed MRBAC method	79
Figure 4.6	Box plot of True Positive (TP), False Positive (FP), Accuracy (ACC), Jaccard Similarity Index (JSI), Dice Coefficient (DC) and Hausdorff Distance (HD) measurements of all the Infarct MR images shown in Figure 4.5 by proposed MRBAC, Region Growing and DRLSE segmentation methods	81
Figure 4.7	Comparative visual analysis of segmentation result of different Hemorrhage MR image obtained by (a) original image (b) ground truth marked by radiologist (c) segmented by Region Growing method (d) segmented by DRLSE method (e) segmented by proposed MRBAC method	83
Figure 4.8	Box plot of True Positive (TP), False Positive (FP), Accuracy (ACC), Jaccard Similarity Index (JSI), Dice Coefficient (DC) and Hausdorff Distance (HD) measurements of all the Hemorrhage MR images shown in Figure 4.7 by proposed MRBAC, Region Growing and DRLSE segmentation methods	86
Figure 5.1	Proposed multi lesion classification scheme	90
Figure 5.2	Proposed CAD system with Fusion network for classification of brain lesion MR images	104

LIST OF TABLES

Table 1.1	Comparison between various MR sequences.	7
Table 1.2	Evolution of intraparenchymal hematoma.	11
Table 3.1	Acquisition protocol of 2D brain tumor, brain hemorrhage, brain infarct acquired from DOON MRI & Diagnostic	45
Table 3.2	Acquisition of 2D MRI database of normal and abnormal brain images acquired from DOON MRI & Diagnostic	46
Table 3.3	Acquisition of 2D MRI database of brain tumor, brain hemorrhage, brain infarct acquired from DOON MRI & Diagnostic	47
Table 4.1	Performance measures obtained by different segmentation methods for MR images of tumor shown in Figure 4.3	75
Table 4.2	Averaged performance measures obtained by different segmentation methods for all MR images of tumor	76
Table 4.3	Comparative performance of segmentation approach with averaged number of iteration and averaged computation time for all tumor images	78
Table 4.4	Performance measures obtained by different segmentation methods for MR images of infarct shown in Figure 4.5	80
Table 4.5	Averaged performance measures obtained by different segmentation methods for all MR images of infarct	80
Table 4.6	Comparative performance of segmentation approach with averaged number of iteration and averaged computational time for all infarct images	82
Table 4.7	Performance measures obtained by different segmentation methods for MR images of hemorrhage shown in Figure 4.7	84
Table 4.8	Averaged performance measures obtained by different segmentation methods for all MRI images of hemorrhage	85
Table 4.9	Comparative performance of segmentation approach with averaged number of iteration and averaged computational time for all hemorrhage images	87
Table 5.1	Details of features extracted for classification model	100

Table 5.2	Performance of 10 neural networks individually for two class classification	107
Table 5.3	Confidence level of 10 NNs and the proposed CAD system for two class classification	108
Table 5.4	Confusion matrix of the proposed fusion network implemented in testing of dataset for two class classification	108
Table 5.5	Performance of 10 neural networks individually for multiclass classification	110
Table 5.6	Confidence level of 10 NNs and the proposed CAD system for multiclass classification	111
Table 5.7	Confusion matrix of the proposed fusion network implemented in testing of dataset for multiclass classification	112

LIST OF ABBREVIATIONS

ACC	Accuracy
ACM	Active Contour Model
ANN	Artificial Neural Networks
ARP	Average Retrieval Precision
ARR	Average Retrieval Rate
AS	Astrocytoma
AVG	Average
AVM	Arteriovenous Malformation
BCFCM	Bias Corrected Fuzzy C-Means
BPDFHE	Brightness Preserving Dynamic Fuzzy Histogram Equalization
BPNN	Back Propagation Neural Network
CAD	Computer Aided Design
CCA	Curvilinear Component Analysis
CL	Confidence Level
CLAHE	Contrast Limited Adaptive Histogram Equalization
CSF	Cerebrospinal fluid
CT	Computed Tomography
DAVF	Dural Arteriovenous Fistula
DC	Dice Coefficient
DICOM	Digital Imaging and Communications in Medicine
DRLSE	Distance Regularized Level Set Evolution
DTCWT	Dual Tree Complex Wavelet Transform
DWI	Diffusion Weighted Imaging
EBACM	Edge Based Active Contour Model
EEG	Electroencephalograph

FCM	Fuzzy C- Means
FD	Fractal Dimension
FDTA	Fractal Dimension Texture Analysis
FOS	First Order Statistics
FP	False Positive
FP-ANN	Feed Forward Back Propagation Artificial Neural Network
FPS	Fourier Power Spectrum
FVF	Fluid Vector flow
GA	Genetic Algorithm
GAC	Geodesic Active Contour
GBM	Glioblastoma Multiforme
GBMs	Glomerular Basement Membranes
Gd	Gadolinium
GLCM	Grey Level Co-occurrence Matrix
GLDS	Gray Level Difference Statistics
GM	Grey Matter
GMM	Gaussian Mixture Model
GP	Gaussian Pyramid
GVF	Gradient Vector Flow
HD	Hausdorff Distance
HI	Hemorrhagic Infarct
IBFs	Intensity Based Features
ICH	Intracerebral Hemorrhage
IFS	Intuitionistic Fuzzy Set

IVH	Intraventricular Hemorrhage
JSI	Jaccard Similarity Index
KG	Knowledge Guided
k-NN	k-Nearest Neighbour
LBP	Local Binary Pattern
LBP ^{u2}	Uniform Local Binary Pattern
LBP ^{ri}	Rotation Invariant Local Binary Pattern
LBP ^{riu2}	Rotation Invariant Uniform Local Binary Pattern
LDA	Linear Discriminant Analysis
LGDF	Local Gaussian Distribution Fitting
LSF	Level Set Function
LTCoP	Local Ternary Co-occurrence Patterns
MED	Childhood Tumor Medulloblastoma
MEN	Meningioma
MRBAC	Modified Region Based Active Contour
MRF	Markov Random Field
MRI	Magnetic Resonance Imaging
mRMR	Minimum Redundancy Maximum Relevance
NGTDM	Neighborhood Grey Tone Difference Matrix
NN	Neural Network
NNC	Neural Network Classifier
PCA	Principal Component Analysis
PD	Proton Density
QC	Quadrigeminal Plate Cistern

RBACM	Region Based Active Contour Model
RF	Random Forest
ROI	Region of Interest
RSF	Region Scalable Fitting
SAR	Specific Absorption Rate
SC	Suprasellar Cistern
SFM	Statistical Feature Matrix
SGLDM	Spatial Gray Level Dependence Matrices
SOM	Self-Organizing Map
STD	Standard Deviation
STIR	Short-tau Inversion Recovery
SVM	Support Vector Machine
TE	Echo Time
TEM	Textures Energy Measure
TI	Inversion Time
TP	True Positive
TR	Repetition Time
TE Data	Testing Data
TR Data	Training Data
US	Ultrasound
WM	White Matter
WPT	Wavelet Packet Transform

CHAPTER 1

INTRODUCTION

1.1 Background

Strokes (resulting from hemorrhage/infarct) and tumor are the leading cause of morbidity and mortality worldwide [1]. The distinction between a tumor and stroke is so fine that at times tumors masquerades itself as strokes leading to false diagnosis [2]. Imaging is an effective tool for early detection. In numerous cases it can detect abnormalities such as cancerous and non-cancerous masses, calcification and other suspicious anomalies well before they become palpable. Moreover, implementation of imaging is not restricted to diagnosis alone. Increasingly, open access surgery is being replaced by minimum invasive procedures and image guided intervention is becoming common.

Magnetic Resonance Imaging (MRI) is a noninvasive diagnostic tool and it finds greater usage in the main stream anatomical studies and pathological planning as compared to its equally available counterpart modalities like Computed Tomography (CT) on account of its excellent soft tissue contrast and multi-planer acquisition capabilities. The human brain in itself is a very complex heterogeneous organ at various spatial scales. Its understanding is limited by the potential of the observer. Even though MRI shows prominent features of the anomaly in image form, its interpretation is still critical, dependent on variability in the observer's perspective. Also, image artefact due to hardware /software malfunction can result in a confusing artifactual MR image. Various ongoing research on the day to day basis in development in the Computer aided design (CAD) tools still needs to be robust and reliable in order to reduce the fatality. Any diminutive misread change can have fatal consequences and this anatomical deviation in an image is influenced by the factors like; artifacts, disease or noise. Therefore, discrimination between normal tissue and pathology has crucial diagnostic merit. Segmentation and classification play a critical role in tackling this big issue.

This chapter focuses on the introduction of one of the fundamental structural imaging tools, that is, MRI, its advantages over other modalities, its application, scope and limitations in three widely common pathologies namely hemorrhage, infarct and tumor.

1.2 Medical Imaging Modalities: A Brief Overview

Over the years, vast development has been made in tomographic imaging modalities such as CT, MRI, Ultrasound, PET etc. and is used as medical diagnostic tools for visualization and

quantitative analysis of the region of the tissue. Any diagnosis is based on the perception of these images obtained by different imaging modalities in a subconscious way, which can be stated that it is a conclusion drawn upon what we see, understand and interpret. These biomedical imaging are grouped into structural or functional imaging tools; consisting of MRI, CT, US, Projectional X-ray (CR, DSA, Mammography) under structural category and FMRI, Nuclear medicine (PET, SPECT) under functional category.

In order to detect the presence of lesion anywhere in human body by any kind of radiological imagery (CT/MR/US), the first thing to look at is, that there must be detectable difference in signal intensities with sufficient contrast resolution in between the disease affected part and the normal part in an image. Secondly, the image should have sufficient spatial resolution so that if the lesion is small and occupying only a part of a pixel, then it does not go undetected if the average mean intensity of the lesion occupying the pixel is comparable with the intensity of consecutive pixel. This effect is known as partial volume effect. The above stated issues, namely, sufficient contrast resolution and sufficient spatial resolution are easily dealt by MR imaging. It is therefore very precise in diagnosing a pathology as it can detect up to 1 mm of size in a pathology. Thus, it can detect subtle anatomical structures and pathology. MRI has tremendous array of tool to vary parameters that can be adjusted to change this nature of image in order to successfully visualize lesion.

In CT there is no such parameter assigned for adjusting spatial resolution. It is relatively fixed from image to image. Similarly, nothing can be done to change intrinsic contrast of that image. Although contrast agent can be injected which can highlight certain areas, but the nature of the image remains the same. There is no choice of parameter in CT /US or other modality which can be used by the technician accordingly to increase contrast but MRI can change the very nature of the image, having several different images (T1, T2, FLAIR, ADC, DWI etc.) with dramatic different levels of contrast.

Both CT and MRI have multi planer imaging capability; however, CT uses high range of radiation which is potentially harmful while MRI poses no risk of irradiation to the human tissue. MRI is useful for delineating soft tissue structures. It easily identifies the flow of blood through certain blood vessels and organs, acknowledging issues with blood circulation, for instance, blockages to be identified. Thus, it can generate highly detailed images for virtually any part of the body tissue, that is dependent on the magnetic properties of nuclei of human cells. Usually for bony structures, CT is the preferred imaging modality as it provides sufficiently accurate details. Also, if time is a decisive factor, then the choice is CT as it is usually completed within

5 minutes while MRI scanning typically runs for about 30 minutes. Thus, the choice of any imaging technique depends on the factors like availability, cost effectiveness, time efficiency, utility in type of tissue to be imaged etc.

1.3 Magnetic Resonance Imaging (MRI)

1.3.1 MRI Suite

MRI plays a prominent role in clinical research and diagnostics. MRI utilizes high magnetic field, electric field gradients, radio waves and a dedicated computer system to create imagery vital for diagnosis and treatment. This technique exploits magnetic property (nuclear spin) of hydrogen nuclei (proton) available in abundance within the human tissue. Other nuclei, which can be imaged in human MRI are- ^{13}C , ^{19}F , ^{31}P , ^{23}Na . Although often the above stated protons are not imaged as they are sparse in biological tissues and they require dedicated RF chain tuned to their resonance frequency.

The basic instrumentation of MRI system is shown in Figure 1.1. Different manufacturers of MRI suite are governed by DICOM standard which provides the framework to process data accurately and accept data from any MRI machine. The fundamental components of MRI Suite consist of a large magnet for generation of uniform static magnetic field, smaller electromagnetic gradient coils with its electronics for acquiring images, a radio transceiver (radio frequency system), data acquisition system and a processing system with a dedicated computer system. The processing system is responsible for correlation between signal generation and its procurement, for image formation and display. Many imaging systems work at fixed field strength which is in units of Tesla (1Tesla (T) =104 Gauss (G)). The strength of the magnetic field is responsible for precession frequency of the atomic nuclei (protons) as well as the net magnetization at thermal equilibrium. The field strength B_0 of the large magnet which encloses the whole human ranges from 0.5T to 9T. It produces a very high field which is homogeneous in nature by aligning the hydrogen protons of the body. Hence it polarizes the nuclear spins of the body. Three gradient coils are used for signal localization in x, y, z directions, have strength of magnitudes G_x , G_y and G_z respectively. The gradient field strength is generally less than 1G/cm. Its main purpose is to change B_0 as a function of position. The main field modified by gradient coils is given by formula $B = (B_0 + G_x x + G_y y + G_z z) \hat{z}$. These gradient coils got two main functions. First one is to improve the homogeneity of B_0 (correct the magnetic imperfection by adjusting currents) by applying magnetic field at 3 orthogonal direction through the process known as shimming, so that the image has better S/N ratio and better resolution. Secondly, by varying current in three different axis, larmor frequency can be produced which is dependent on position. The RF system

consist of transmitter coil accountable for generating a rotating magnetic field (B_1) in a pulse sequence for instigating the spin system and a receiver coil which changes the precessing magnetization into an electrical signal thereby detecting transverse magnetization. These coils generate the oscillating magnetic field which resonates with the nuclei, thereby producing a torque on protons which tips the magnetization out of equilibrium into the transverse plane. These coils play a very significant role in the formation of MR images [3, 4].

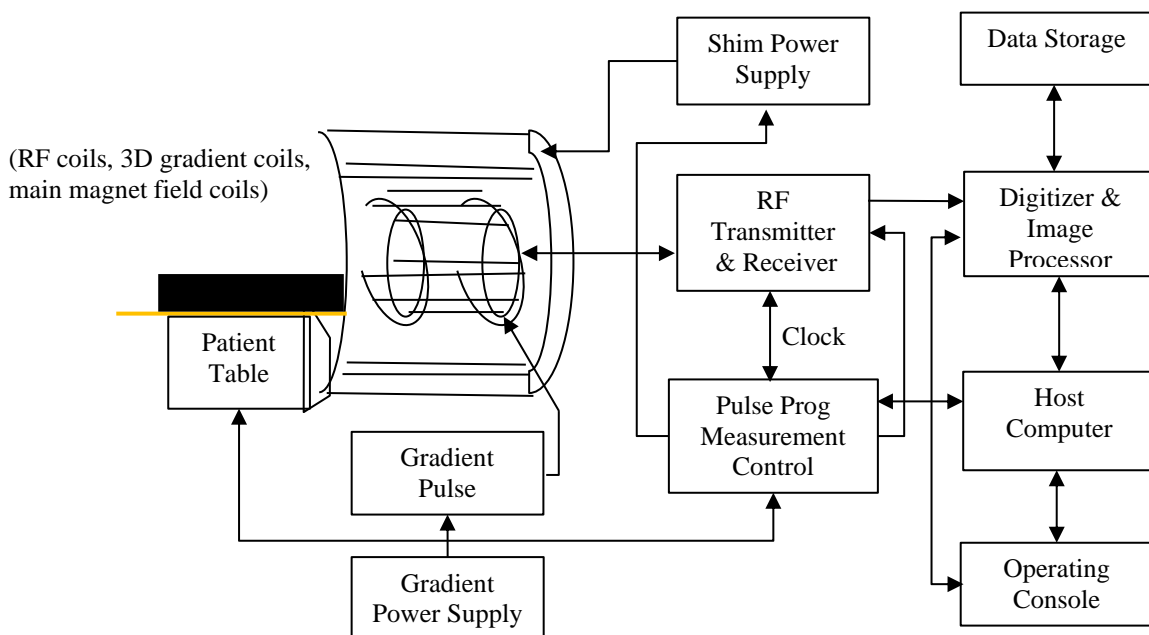


Figure 1.1: Basic instrumentation of MR imaging system

A human subject is placed in a consistent strength magnetic field, B_0 . It becomes temporarily magnetized as the protons in the body aligns with the magnetic field building the net macroscopic magnetic moment M parallel to B_0 . When a RF transverse pulse is activated perpendicularly to B_0 , it leads to the resonant excitation of the magnetic moment precessing into the perpendicular plane. As soon as the RF perturbation is removed, all the nuclear spins return from this state of imbalance to thermodynamic equilibrium known as relaxation by emitting EM energy or NMR signal. The NMR phenomenon occurs when there is exchange of energy between two systems at resonance. Two types of relaxation happen after excitation namely, longitudinal T_1 relaxation time and T_2 transverse relaxation time. During T_1 relaxation (or spin-lattice interaction), thermal equilibrium is established due to the exchange of energy between spins and surrounding lattice. T_1 relaxation time required for regaining longitudinal magnetization following an exponential curve after RF pulse is applied. T_2 is a transverse relaxation (or spin-spin interaction) leads to the accumulative phase loss of spin or loss of coherence, causing transverse magnetization decay.

In humans T1-weighted images are used to evaluate the gross anatomy and structure of brain though it can be used for pathology, if combined with contrast enhancement. T2-weighted images are particularly useful for pathological investigations. They are used to detect intra parenchymal signal abnormalities. MRI contrast agents such as Gadolinium (Gd) work through shortening of T1 relaxation time of nearby located protons. T1 shortens with an increase in rate of stimulated emission from high energy states to low energy states. The images obtained are called post contrast T1-weighted images [5, 6].

Different tissue variables which are intrinsic in nature, are spin density, (T1 and T2) relaxation times, T2* and flow and spectral shifts are used to construct images. Other variables dependent on instrument are TR (Repetition Time), TE (Echo Time), TI (Inversion Time), θ (Rotation angle) and T2*. By changing the scanner parameters, contrast is affected in-between different types of body tissue or between other properties, as in fMRI and diffusion MRI [4, 7, 8].

Thus, tissue contrast in between different structures, is enhanced with the change (deviation) in signal intensity in the MR Image, and these intensity descriptors in MRI are referred as hyper intense (bright), iso-intense (minimal change), and hypo-intense (dark). Figure 1.2(a) shows an abnormal T2-weighted image. It can be seen clearly that the gray matter is brighter than the white matter, CSF in the suprasellar cistern (SC) and quadrigeminal plate cistern (QC) is bright. The lesion i.e. suprasellar epidermoid mass (outlined by the arrow) is hyperintense in nature though some area of the mass share signal characteristic that are similar to CSF, therefore it can be characterized isointense with respect to CSF. Figure 1.2(b) shows a non-contrast T1-weighted image in which the lesion (marked by arrow) is hypointense. Since gray matter is darker than white matter, the CSF and globes are dark as well as no enhancing vessel and dura matter is

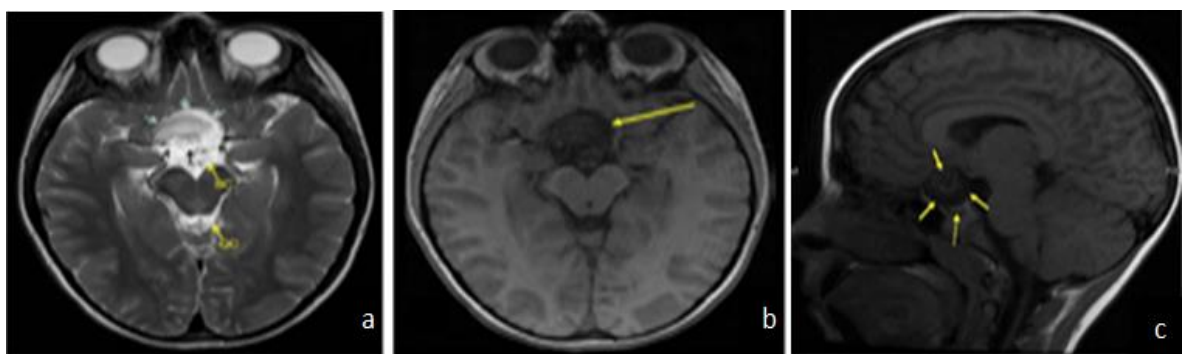


Figure 1.2: T2 and T1-weighted MR Brain images of a patient in axial (a, b) and sagittal (c) planes respectively

seen, it gives confirmation that image is T1-weighted. The same epidermoid mass (solid arrows) is seen somewhat heterogeneous but mostly hypointense signal in midline sagittal T1-weighted image in Figure 1.2(c). The top pituitary gland (dashed arrow) is being compressed a bit by mass.

1.3.2 Types of Sequence and its Reading

An MRI sequence is the specific setting of RF pulses and gradients which result in a set of images having notable peculiar appearance. Albeit, multitude pulse sequences are there (like T1, T2, proton density, T2*, FLAIR, DWI, ADC, FAT saturation etc.) each of them keeping their unique characteristic to discern tissue composition; the most frequently used MRI sequences are T1, T2 sequence. T1 or T2 images are obtained by manipulating two basic parameters: TR (repetition time) and TE (echo time). Contrast agents like Gadolinium, comes handy to highlight some of the different structures or pathology. The following images in Figure 1.3 and Table 1.1 accentuate the qualities and differences between the most commonly used sequences.

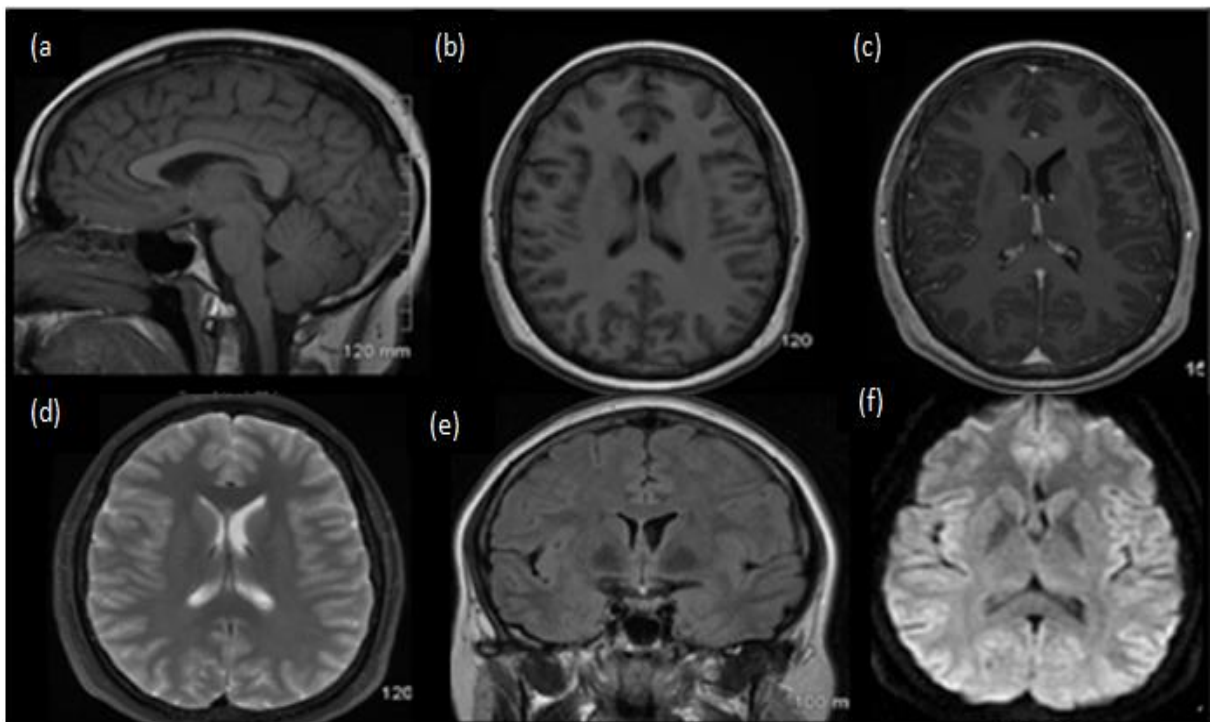


Figure 1.3: Comparative visual demarcation between most frequently used sequences i.e. T1, T2, FLAIR and DWI in MR Brain images of a patient. (a) Sagittal T1 for evaluating midline structures (b) Axial T1 for evaluating anatomic detail (c) axial T1 with contrast for evaluating BBB breakdown (d) Axial T2 for looking at areas of edema and pathology (e) Coronal FLAIR for evaluating edema with CSF (f) Axial DWI for stroke imaging, abscess, cellular tumors.

Table 1.1: Comparison between various MR sequences

MRI Sequence	Grey Matter	White Matter	Ventricles, CSF	Orbit	Orbital Fat	Property
T1 Weighted	Dark	Bright	Black	Dark	Bright	Fat High, Water low Looks for anatomy
T2 Weighted	Bright	Dark	White	White	Bright	Water high, Fat low Looks for pathology
T2 FLAIR	Bright	Dark	Black	Black	Bright	T2 W image with suppression of CSF signal
T2* (GRE)	Bright	Dark	Bright	Bright	Dark	Detects blood products. Hemosiderin blooms dark black
PD (Proton Density)	Depends on the T1 or T2 Weighting that is favored (mix of above characteristics). Number of protons per volume. Contrast increases between CSF (intermediate signal) and pathology (bright) than in T2 (both bright)					For menisci and gray/white matter evaluation
T1 Post Contrast (Gadolinium)	Distributes in vessels and tissues without blood brain barrier, if BBB Breaks gadolinium leaks and causes enhancement, makes enhanced areas in T1 image brighter. Detect and characterize lesion, MR angiography					Shortens T1 relaxation time
Diffusion weighted (DWI)	Bright when water cannot diffuse. True restricted diffusion should be bright on DWI and dark on ADC (Apparent Diffusion Coefficient). Restriction in acute ischemia/infection, cell rich tissue.					Motion of protons

1.3.3 Safety and Precautionary Aspects

Since MRI suite interacts with high magnitude radio waves and high magnetic field, some precautionary measure should be taken for the protection of human subject in order to address the concerns raised due to the occurrence of careless mishap, leading to emergencies. First and foremost important point after the installation of MRI machine is to give proper training to the technician, nurses as well as to the radiologist for operating as well as for addressing emergency measures to be taken in case of any potential danger. The following points should be duly noted before entering the MRI suite. Careful and comprehensive screening of every individual (patient, maintenance worker, security, cleaning and emergency personal) should be done. High strength hand held magnet as well as Ferro magnetic detectors should be used for screening purpose, to ensure that the entering patient does not have any potential contraindicated devices embedded within (resulting from prior surgery). Even though MRI poses no risk for machines up to 4T or less, still pregnant women should be excluded, as there is yet the need of research to find possibility of risk to the growing foetus and only in case of emergency when the risk to the benefits are properly judged, must they be allowed to undergo tests. Also, claustrophobic and other anxiety issues should be duly considered. Thus, in general, to ensure the adequate scanning as well as for patient safety and risk measurement, these issues should be administered carefully which are as follows : acknowledgement of mechanical and biological effect of static magnetic

field, safety measures in dealing gradient and RF magnetic field, cryogen usage and its safety aspect, SAR (specific absorption rate), peak sound levels (not more than 140 dB), medical issues (cardiac issues, dental appliances or any implant inside the body , psychiatric issues, sedation, contrast agent like gadolinium or iodine induced allergy, acoustic noise level depending on pulse sequence impacting hearing etc).

1.4 Medical Conditions in Brain: Study of Three Common Diseases under MR Imaging

With the rising incidence in mortality among adults and children due to strokes and trauma, primary and metastatic brain tumor, vascular abnormalities, brain infection and multiple sclerosis; MRI has come up as the best option of neuroimaging. In the present work, our focus of study is on the three most common abnormalities namely Brain Hemorrhage, Brain Infarct and Brain Tumor.

1.4.1 Brain Hemorrhage on Magnetic Resonance (MR) Images

A brain hemorrhage is a bleeding, occurring in or around the brain. In other words, it means, “bursting forth”. Symptoms arising because of cerebrovascular problems can be clinically grouped together as “Stroke”. However, this term is used more often when suddenly noticeable symptoms occur. Approximately 13% of the strokes occur because of the burst of an artery in the brain resulting in localized bleeding within the brain tissues killing the cells of the brain [9].

Bleeding can occur within the brain, amidst the skull and the covering of the brain, between the layers of the brain's covering or between the brain and the membranes that cover it. Depending on the locus of the blood loss (bleed), brain hemorrhage is often labelled as extra-axial hemorrhage (inside of the skull) and intra-axial (within the brain itself). Intra-axial hemorrhages are of two types in accordance to the exact anatomical location of the bleeding such as: Intracerebral Hemorrhage (ICH) and Intraventricular Hemorrhage (IVH). Extra-axial hemorrhages are classified in accordance with the anatomical layer of meninges where bleeding occurs, namely: Epidural Hematoma, Subdural Hematoma and Subarachnoid Hemorrhage [10,11,12,13]. Epidural and Subdural Hematomas are more likely to result from trauma or after a fall [14, 15,16,17].

1.4.2 Types of Hemorrhage

- **Extra-Axial hemorrhage**

These kinds of hemorrhages arise from the extra vascular accumulation of blood within the intracranial vault. There are several factors inducing brain hemorrhages. The most common cause are head trauma i.e. penetrating and non-penetrating cranial trauma (blunt head injury). Non traumatic causes include hypertension, aneurysm, auto regulatory dysfunction, blood vessel abnormalities like arteriovenous malformation (AVM), hemorrhagic necrosis, venous outflow obstruction, bleeding disorder like haemophilia and sickle cell anaemia. Other factors which also influence the evaluation are: the site of the hemorrhage, the integrity of the blood-brain barrier and haemoglobin concentration [18, 19, 20, 21].

- **Intra-Axial hemorrhage**

It is a kind of intracranial hemorrhage where bleeding occurs due to the obliteration of blood vessels inside brain leading to the acute building up of blood in the brain parenchyma. Its treatment, aetiology, and prognosis alter extensively relying on the type of hemorrhage. It is a life-threatening condition in which oxygen and blood supply to the brain is curtailed. The major reasons attributed to this kind of hemorrhage are high blood pressure, increased age, heavy drug and alcohol use. Other minor causes are trauma, malformed blood vessels, blood thinner usage, internal tumour bleed and bleeding disorders. Furthermore, thrombotic or embolic stroke can also convert to intracerebral hemorrhage. Birth defects of weak blood vessels can lead to leaking arteriovenous malformation (AVM) which leads to intracerebral hemorrhage in rare cases.

1.4.3 Classification of Hemorrhage

Position, volume, density (homo or hetero), shape (regular or irregular), should be considered with any intracerebral hemorrhage as they have prognostic implications. Types of hemorrhage depending on the location include basal ganglia hemorrhage, thalamic hemorrhage, pontine hemorrhage, cerebella hemorrhage, lobar hemorrhage. On the basis of aetiology, it is divided into hemorrhagic venous infarct, hypertensive hemorrhage, hemorrhagic transformation of ischaemic infarct etc. A simple categorization of hemorrhage is based on location and based on aetiology, is depicted in Figure 1.4.

In terms of timing hemorrhages are characterized as hyper acute hemorrhage, acute hemorrhage, early sub-acute hemorrhage, late sub-acute hemorrhage and chronic hemorrhage [22,23, 24]. Table 1.2 summarizes the evolution of intraparenchymal hematoma. Hemorrhage

appears totally different in all the five phases on MRI. The very appearance of hemorrhage on MR can be changed based on pulse sequence and time after the hemorrhage is been occurred. The change in signal intensity on MRI depends on the change (transition) of oxidative state of Iron (Fe) in hemoglobin, susceptibility and paramagnetic effects. Here, cellular and fluid components visualize differently on image.

Thus, if hemorrhage is present then, signal loss is in proportion to the magnetic susceptibility of the blood products. On MR, the impact of the presence of iron (Fe) in hematoma, on the magnetic field which in turn affects the signal detected from water proton is measured. Thus, the secondary effect of blood on tissue is measured on MR rather than the blood itself as is the case with CT. Also, the iron (Fe) in the hemoglobin will only have an effect on tissue to the extent the amount of para-magnetism is present in the tissue.

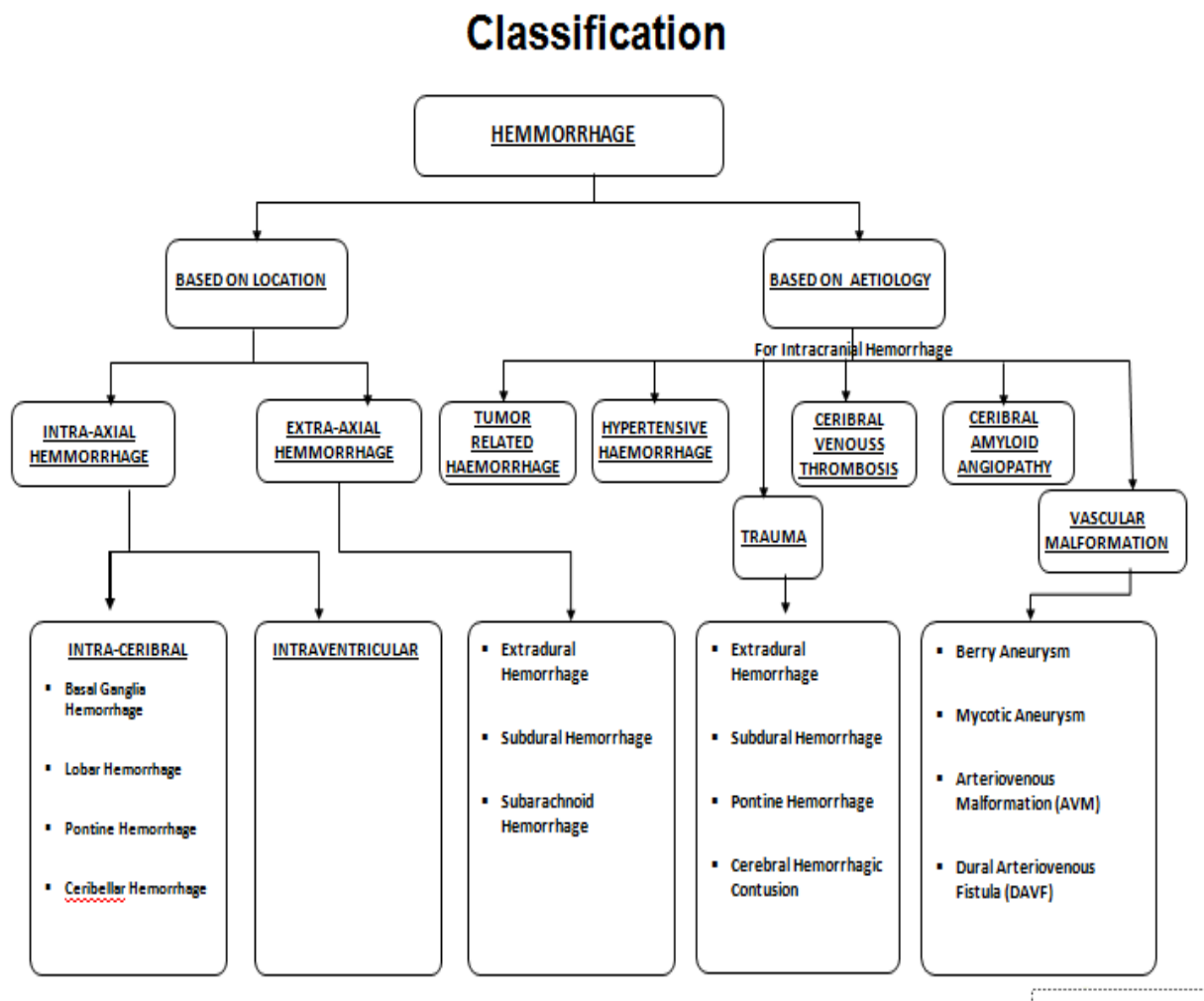












Figure 1.4: Hemorrhage (ICH) classification on the basis on site of occurrence and basis of underlying causes leading to its development.

Table 1.2: Evolution of Intraparenchymal hematoma

Stages of Hematoma					
		Haemoglobin	Location	T1	T2
• <i>Hyperacute</i>	< 24 hrs.	Oxyhemoglobin	Intracellular		
• <i>Acute</i>	< 1-3 days	Deoxyhemoglobin	Intracellular		
• <i>Early Subacute</i>	> 3 days	Methemoglobin	Intracellular		
• <i>Late Subacute</i>	> 7 days	Methemoglobin	Extracellular		
• <i>Chronic</i>	> 14 days	Ferritin & hemosiderin	Extracellular		

Initially some ratio of oxygenated to deoxygenated hemoglobin is present at the time of hemorrhage and over time there is a progressive change in the state of hemoglobin as the clot in this hematoma is going to evolve, be degraded and reabsorbed. Thus, predominantly deoxygenated hemoglobin is present, then hemoglobin molecule becomes oxidized to form methemoglobin and eventually is the formation of hemosiderin which gets scavenged up by inflammatory cells (like microglia or macrophages) and then stays around in the tissue in that form forever.

This change in state of the bleed, that is, hematoma conversion due oxidation and/or its molecule structure change after the onset at different stages (oxygenated hemoglobin, deoxygenated hemoglobin, methemoglobin or hemosiderin), is picked up in MR image. Iron is paramagnetic in nature; however, the magnetic susceptibility affect is not always seen. Oxygenated hemoglobin also contains iron (Fe) but its magnetic susceptibility effects get shielded by the presence of oxygen molecule resulting to its dia-magnetic nature. So, no signal loss is there in case of oxygenated hemoglobin.

Oxygenated hemoglobin (which is at negative side on the magnetic susceptibility scale) is mostly never seen as it ultimately takes some time by the patient to get into the scanner and in that time, it converts into deoxygenated hemoglobin.

The change from oxy hemoglobin to deoxy hemoglobin results in the change in the conformation of the molecule such that now the dramatic susceptibility affect (large amount of signal loss) can be seen T2* image, GRE will be sensitive to this effect. The other forms of hemoglobin i.e. meth hemoglobin and hemosiderin have progressively increasing degree of magnetic susceptibility, however, out of all (deoxygenated hemoglobin, methemoglobin, hemosiderin)

only meth hemoglobin shows the increase in signal on T1-weighted image due to the fact that its molecule conformation is such that paramagnetic effect is not shielded and its iron is exposed to have enough proximity ($<3 \text{ \AA}$) to those of water proton leading to proton electron dipole interaction. Since hematoma evolution is a process, there is never an absolute magnetic susceptibility. In-between the meth hemoglobin and hemosiderin, comes the state when meth hemoglobin diffuses throughout the area of the clot in the intervening serum and such state is known as extracellular state; giving the signal loss due to 3\AA distance between proton and electron, whose impact can be seen in the image unlike in the case of deoxy hemoglobin where blood is located in the pockets of the cells (intracellular). It is important to note that blood appears hypointense and blooms black on MRI T2*image. Intracranial blood products age differently than extracranial blood products. The extracranial hematomas generally have heterogeneous appearance.

1.4.4 Role of MR in Case of Hemorrhage

It has been concluded by one of the studies (2015) that MR shows far more superior results of IVH in comparison with the CT by yielding (returning) better estimates of intraventricular blood volume. Even for the small volumes IVH gets detected on MRI showing its exceptional efficiency. Albeit, awareness of technical characteristics between the two modalities is required for analyzing the results correctly. It was found that 3% of the IVH cases were missed out by CT while MR was 100% sensitive. The Gareb Score of MRI was higher by 24% [14].

The following are the promising areas where MRI has found its crucial usage regarding intracranial hemorrhage and ischemic stroke [25].

- a) In case of acute subarachnoid hemorrhage with patient having multiple aneurysms, it is used to decide which aneurysm is ruptured in particular.
- b) MRI is used to anticipate the fate of unruptured intracranial saccular aneurysms.
- c) It is needed to evaluate vasculitis activity and atherosclerotic plaque activity.
- d) It specifically locates atherosclerotic plaque relative to branch artery ostia and to investigate stroke etiology as well as to evaluate possible hazard of angioplasty.
- e) Used for discrimination in-between intracranial atherosclerotic plaque, arterial dissection, reversible cerebral vasoconstriction syndrome, vasculitis, and other causes of intracranial arterial narrowing.

1.4.5 Mimics in Hemorrhage

On MRI, lesions containing protein, calcification, fat (e.g. lipomas or dermoids) and melanin cause hyperintensity on T1-weighted images, occasionally get mistaken for hemorrhage, due to their similar appearance. Intracellular and extracellular methemoglobin hyperintensities have similar appearance with other conditions or pathologies like melanotic metastases on T1-weighted images. On turbo fast spin-echo T2-weighted MR image, the fat turns out bright while on traditional spin-echo T2-weighted MR image it appears hypointense. Hemorrhages can be distinguished from fat by usage of fat-suppression methods comprising of chemical shift imaging or inversion recovery sequences (e.g. STIR (short-tau inversion recovery)). The existence of chemical shift artifact may also lead to faulty indication of a fatty lesion. Gradient-echo images show profound hypo intensity in both calcification and hemorrhage, thereby mimicking each other. Also, the existence of residual gadolinium-based contrast material can mimic hemorrhage. However, location as well as morphological differences of the aberrant signal intensity along with clinical presentation of lesion will be enough to differentiate between these two. CT also offers help to distinguish these entities.

1.4.6 Brain Infarction on Magnetic Resonance (MR) Images

Brain infarct are the leading cause of emergency conditions worldwide and they lead up to 80% of ischemic strokes and about 15% hemorrhagic stroke related death. It is the major area of concern for clinical practitioners due to the ever-increasing number of cases. A series of pathophysiological events occurs because of the occlusion of artery depriving brain of oxygen and nutrients. The damaged brain tissue enclosing core ischemic lesion whose recovery is (potentially reversible) is possible if identified effectively. This condition is referred as ischemic penumbra. After the start of ischemia, this penumbral tissue is salvageable only within the first few hours. Therefore, the main challenge of the therapeutic decision based on imaging methods (CT, MRI, PET), is to speedily identify the source blocked artery for prompt recanalization. Different tissues have tissue specific imaging signature which change with time as the infarction evolve. Various methods have been developed to locate the extent of tissue which is at the risk of infarction. Over the last 20 years many image processing and analysis approaches have been tried for infarction related numerous things such as: to scrutinize different tissue states, to quantify tissue diffusion, to spatially delineate difference between salvageable and dead tissue, predicting final outcome of ischemic tissue fate etc. It is also required to comprehend the aspects that have impact on dynamic evolution of infarct and penumbra such as collateral flow pathways,

lesion swelling, and spontaneous reperfusion.

“Stroke” is a medical term for signs that appear from cerebrovascular problems [26]. It is the abrupt stopping of the blood supply to the brain. The term stroke is often used for sudden noticeable symptoms for example single-side paralysis, single side vision loss, speech slurring, and one side face drooping etc. Maximum number of strokes are evoked by the sudden occlusion of an artery (ischemic stroke) while the minor portion of other strokes are brought in by bleeding into brain tissue when a blood vessel out bursts (hemorrhagic stroke). Depending on the part of brain which is injured and severity of stroke, the after effects are seen. As different areas and functions are managed by different parts of the brain, generally the immediate area encompassing the stroke gets affected. The mortality rate in case of hemorrhagic strokes is much higher in comparison with ischemic strokes.

Cerebrovascular problems are of three types namely thrombosis, embolism, and hemorrhage. Rapid neurological deficit occur because of embolism and thrombosis is due to infarction, which is either hemorrhagic or ischemic in nature. Hemorrhage tends to accumulate in the brain as a mass. Infarcts are classified in two groups as hemorrhagic (red) and ischemic (pale) infarcts on the basis of either there is hemorrhage present in or is enclosing the infarct. If the blood supply is being cut to the part of the brain by thrombus, a large embolus or by even severe vasculitis, then those infarcts are labelled as Ischemic. These kinds of infarct look pale or lighter than the surrounding brain tissue. Thrombosis is the most frequent cause of ischemic infarcts. The most common places to have thrombosis are the origin of the middle cerebral artery, the carotid bifurcation, or either end of the basilar artery.

The extent of ischemia (degree of patency of the primary occlusive lesion) varies in regard with total volume of blood flow received by the part of brain from the thrombosed arteries or by the artery occluded by the big embolus. Hemorrhagic infarcts also known as red infarcts (due to the presence of extravasated blood) are usually connected with embolic events. It results from either the small emboli showering the area or by collateral flow reperfusing the brain area containing the fragile vessel. Hemorrhagic infarct is seen following breakdown of the lamina of the micro vessels. Just like hemorrhage, ischaemic strokes also age in a similar fashion. In terms of timing infarcts are characterized as early hyper acute, late hyperacute, acute, sub-acute and chronic. It appears totally different in all the five phases on MRI. The very appearance of infarct on MR can be changed based on pulse sequence and time after it has been occurred. Although this terminology has substantial heterogeneity rising from the time of its onset, the following definition summarizes the evolution of infarction [27].

- Early Hyperacute: Time frame - 0 to 6 hours

-
- Late Hyperacute: Time frame - 6 to 24 hours
 - Acute: Time frame - 24 hours to 1 week
 - Subacute Time frame - 1 to 3 weeks
 - Chronic Time frame - more than 3 weeks

1.4.7 Mimics in Infarct

The difficulties and factors associated with identification of infarction is already been discussed. However, differentiating HI (hemorrhagic infarct) from ICH (Intra cerebral hemorrhage) is another issue of concern. It is important to distinguish these two entities which mimic each other. Intracerebral hemorrhage (ICH) sometimes overlaps with a hemorrhagic infarct and hence needs to be differentiated as the line of treatment will then vary. Cautious examination of the profile of the stroke on the primary CT in different sections would be helpful in distinguishing between the two conditions. Characterizing parenchymal intracerebral hemorrhage from hemorrhagic infarct can be challenging. The treatment and management of these two complaints is not the same and so the importance of accurate diagnosis [28, 29].

The following points to be noted to distinguish between HI and ICH.

In case of Hemorrhagic Infarct:

- Areas of infarct are distant from the site of hemorrhagic infarct.
- On perfusion imaging, the center of the hematoma corresponds to highest risk of infarction.
- Evidence of occlusive disease on TOF imaging.

In case of Intracerebral Hemorrhage:

- On perfusion imaging, the region of the deficit does not extend beyond the region of infarct.

1.4.8 Brain Tumors on Magnetic Resonance (MR) Images

Brain is an organ composed of soft nervous tissue in the form of soft spongy mass. The brain is constituted of three major parts. The cortex- which is the outermost layer of brain cells controls thinking and voluntary movements. The brain stem controls basic activities like breathing and sleep, lies in-between the rest of the brain and spinal cord. The basal ganglia situated in center of brain is a mass of structures which monitors and controls coordination between other brain areas. The cerebellum situated at backside of brain aids in balance and coordination. This highly specialized organ is protected by skull bones, tissue layers and

cerebrospinal fluid. The most common disease manifested in the brain is brain tumor which arises due to uncontrolled cell division [4, 7, 8]. These can be divided into primary and secondary brain tumors. Primary brain tumors originate in the brain. Tumors can start in any part of the brain or related structures. The prominent examples are Meningioma (MEN), Childhood Tumor Medulloblastoma (MED), Glioblastoma Multiforome (GBM), Astrocytoma (AS) etc. [30,31]. The secondary brain tumors may originate in other parts of the body and finally affect the brain via cerebrospinal fluid or blood stream. Hence, the tumors of the lung, breast, kidney, stomach, bowel (colon), and melanoma skin cancer can all spread to the brain. These tumors are highly diverse in terms of appearance which includes shape and size, texture, location and intensity. To analyses such a diverse area of study (Brain Tumors) high level of visual contrast between the tumor and its background is required which is possible in MRI along with the visibility of tumor in multiple levels of projection.

The Figure 1.5 (a) shows MR image of patient in which the brain tumor is shown in the axial plane, Figure 1.5 (b) shows the same in the sagittal plane whereas Figure 1.5 (c) shows the brain image of tumor patient in the coronal plane. The basic intensity and texture information of the brain tumors is provided by MR sequences namely T1 and T2-weighted and post contrast weighted scans. Image analysis shows that either the images are isointense i.e. the tumor having the same intensity as surrounding tissue or hypointense i.e. tumor darker than the surrounding tissue or hyperintense i.e. the tumor brighter than the surrounding tissue. Tumors can be visualized as solid hypo to isointense in T1-weighted image, hypo to isointense in T2 weighed image and necrotic Hypo in T1 or hyperintense in T2-weighted image. Pressure zones where brain tissue is compressed by invasive process appear hyperintense on T2-weighted MR images [32]. If characterized on the basis of tumor texture, it can be homogenous relatively similar intensity of the entire tumor or Heterogeneous with different signal intensity within the tumor.

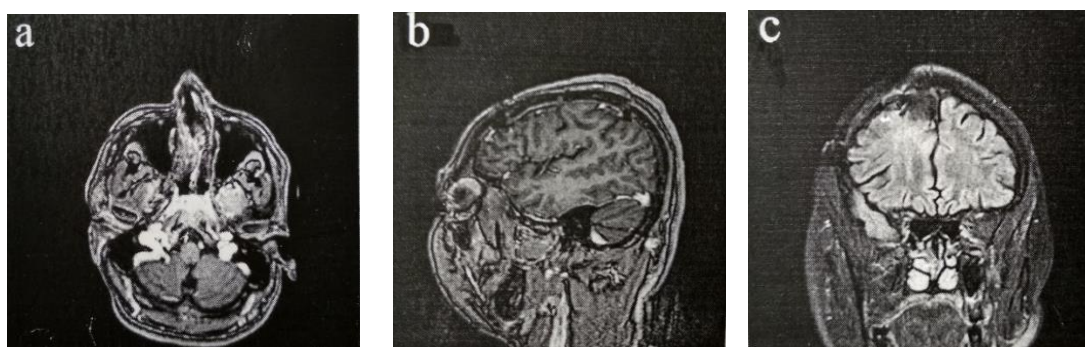


Figure 1.5: MR brain images of tumor patients in axial, sagittal and coronal planes

1.5 Need for Abnormal MR Brain Detection

The human brain in itself is a very intricate organ. It consists of two hemispheres which are further subdivided into 4 lobes namely: the frontal lobe, the parietal lobe, the temporal lobe and the occipital lobe. The division of frontal and parietal lobes is done by a deep groove, the central sulcus (Rolando's fissure). The lateral fissure (Sylvain fissure) separates the temporal lobe from the frontal lobe. Any minor change resulting from any kind of disease or insult can cause serious further implications. For example, the brain surface consists of gyri and sulci. The sulci will be compressed if there is brain edema, while it will expand in case of atrophy (as in Alzheimer's disease) as a result of tissue loss. Any kind to change i.e. compression or dilation from the normal anatomy due to accumulation of blood or due to necrosis by the disruption of atrioventricular blood flow leads to cerebrovascular problems.

So, in case of medical problems in brain the obvious course of action, for detection of a hemorrhage are: obliteration of the gyri-sulci pattern, asymmetry, abnormal distinction gray-white matter, hyper/hypo dense abnormalities etc, in brain parenchyma; hydrocephalus or intraventricular blood in ventricular system; extra cranial soft tissue swelling, fracture, normal air content of the sinuses and the mastoid in bone. Along with the patient's symptoms towards disease and pathophysiological (pathogenetic) information, all of these above investigations as well as others in case of different brain problem, can be easily reflected in medical imaging modalities, thereby aiding physician with additional information, for a quick differential diagnosis. Thus, the utmost importance of synergistic effects of medical imaging field and clinical field cannot be ignored. Also, even though MRI prominent features has drafted the anomaly in image form, its visualization is still critical, dependent on intra observer variability. Various ongoing research in development of CAD tools still needs to be robust and then has to be adopted on a common platform in order to reduce the fatality [33, 34, 35,36].

1.6 Need for Segmentation

The main purpose of segmentation is to convert the given image clinical information into more meaningful consequential image relevant for analysis by contouring the specific ROI's. The crucial morphological information is derived later on serving as a significant qualitative/quantitative descriptor for image analysis [37]. The eventual success or failure of any CAD system is largely proportional to the segmentation technique adapted in the model. Segmentation of brain lesion has always been the most challenging task on account of the brain complex structure and inter observer readability which require significant degree of accuracy and

precision. Segmentation ambiguity increases if the lesion is not perfectly clear, i.e. it has fuzzy visibility due to varied reasons like machine or subject developed artifacts, presence of homogeneous lesion isointense near the similar intensity brain parenchyma, presence of perilesional/cytotoxic/vasogenic edema surrounding lesion near similar background. Sometimes lesion infiltration into the normal tissue additionally creates dilemma. Furthermore, segmentation is used as a measure of lesion size (recession/growth) pertaining to particular treatment, in therapeutics before radiation therapy, in radiation dose calculation etc. Partial volume artifact, geometric distortion, inter slice gaps, misalignment within image series are the challenges which complicate the segmentation process. For achieving accurate segmentation from MR images, these challenges are compensated by preprocessing steps involved in the automatic/ semi-automatic segmentation models. Also, contouring lesions manually in hundreds of MRI slices is a laborious task prone to subjective variations. Hence, there is always the requirement of generalized system generated segmented results which is least affected by human interpretations and gives the conclusions totally based on the mathematical operations performed with the pixel in an image.

1.7 Need of Classification

Diagnostic MRI is a useful tool in clinical medicine. Because of its qualitative, subjective and experience-based nature, MRI can be impacted by image conditions, for instance scanning equipment, machine generated artifacts as well as machine setting. Visual fatigue can be induced in the radiologist analyzing multiple MR images, and this in turn make lesion even harder to differentiate and locate leading in possibilities of faulty interpretations. Brain lesion on MR images often have overlapping characteristics. The visual judgment for distinguishing brain lesions is rather confusing and accuracy of diagnosis largely dependent on the radiologist's knowledge as well as expertise. This often conduce bias effects in diagnostic procedure and restrict its objectivity and reproducibility. In difficult cases of strokes and tumor, the radiologist often prefers to go in for additional corroborating imaging modalities (CT) that are costly and time consuming or a biopsy (in case of tumors) which is an invasive procedure with risk of bleeding and infection. It has been long recognized that errors in image interpretation are inevitable even for the best human observer. Such errors may be exacerbated as a result of fatigue, inexperience or environmental factors. Hence, there is a necessity to develop a *computer assisted classification system (CAC)* which can be utilized by the radiologist as a non-invasive diagnostic tool to back up their observations based on visual appearance of brain lesions on MRI scans. [38]. The goal of the CAC system is to improve the quality and the productivity of clinician task

by improving the accuracy and consistency in radiological diagnosis and thus reducing the image interpretation time. MR diagnosis with the assistance of an efficient and reliable CAC system may reduce the frequency of further examinations with expensive imaging or invasive methods that may be required.

1.8 Organization of Thesis

The research work carried out here in this thesis is presented under two different aspects. The first aspect deals with the *segmentation of brain MR medical images* while the second one deals with the *detection and discrimination of pathology* between stroke, hemorrhage and tumor.

This thesis comprises of six chapters. The first chapter introduces the topic and states the objectives of the subsequent research. The remainder of the thesis is organized as follows:

Chapter 2 provides a detailed literature review on various segmentation techniques. It also provided a detailed study on feature extraction and feature selection of brain lesion. Later in this chapter, classification methods using artificial neural network (ANN) and support vector machine (SVM) are discussed along with the research gaps related to this study.

Chapter 3 provides data set sources and dataset used for proposed methods as well as the protocol followed for data acquisition.

Chapter 4 presents the proposed as well as detailed description of active contour-based segmentation algorithm for segmenting brain lesion. The segmentation results of the proposed approach along with the testing of method on different datasets is discussed in the later part of the chapter. To provide in-depth insight, a comparison is also made between the segmentation results obtained by the proposed and the other approaches.

Chapter 5 presents spatial domain texture analysis of brain MRI. The effect of the feature reduction techniques is investigated. Also, it discusses the development of a classification method based on artificial neural network (ANN) along with the quantitative result analysis.

Chapter 6 summarizes the conclusions drawn from the intensive experimentation carried out in the thesis highlighting important points which support the advantages of the proposed methodology. The scope for future work in this field is also suggested.

1.9 Research Contribution

This work has focused on segmentation and classification of brain MR medical images for identification of the three major fatalities, namely Tumor, Infarct and Hemorrhage.

Since visual perception of MR images during prognosis of disease contouring and classification is subjective to inter-observer variability, so most of the effort has been directed towards designing and development of effective methods to extract particular region precisely and accurately as well as to differentiate between lesions which sometimes mimic one another.

The contributions that present work aims to highlight are as follows:

1. For the designing and development of segmentation model, a novel technique named as MRBAC (modified region based active contour) method is formulated. This technique is variant of region based (ACM) active contour methods. Generally, region-based ACM evolution is relied on global information due to which in the presence of intensity inhomogeneity these model fails. *Although few variations are presented in literature to incorporate local information empirically in the image, but their demerit is the involvement of complicated procedures resulting to highly time intensive procedures.* The proposed modified region based active contour method (MRBAC) is a variant of LGDF model [243]. Classical LGDF model findings are disputable in certain cases of MRI lesions and may not fit well when presented with the image, where the background and foreground have only a difference in texture or when the object boundaries are very weak. Also, defining the initial contour location was done empirically which is time consuming process. *The proposed method conserves the merits of traditional technique along with adopting the new feature for contour initialization.* The radiologist present in the MRI center can manually trace the contour which seeks high amount of attention, patience and time. The proposed method speeds up the whole process as it requires the involvement of technicians who can quickly rough mark the boundary. So instead of empirically feeding data (ρ value) for defining the initial contour location, the proposed method directly feeds the rough marking as initial level set and updates the local intensity information (mean and standard deviation) until convergence. If the change in evolving contour of the level set function between successive iteration is less than the termination criterion, in our case 0.3, then contour evolution is stopped automatically. The proposed method is then ten tested on three pathologies by conducting three separate experiments to assess the working of the formulated algorithm. The experiments are executed on homogeneous, heterogeneous and diffused lesions on MR images and are compared with the ground truth demarcated by radiologists. In order to

analyze and evaluate the performance of the segmentation scheme quantitatively several validation parameters are used namely, TP, FP, ACC, JSI, DC and HD, results of which are mentioned in chapter 4.

2. For the designing and development of classification model of homogeneous, heterogeneous and diffused pathology for detection of lesions (hemorrhage, brain infarct and brain tumor) on routinely acquired T1 and T2-weighted MR images, an ANN classification system is developed. In order to remove the redundancy and speed up the whole process, feature extraction and feature selection is done in the present study. For extracting image parameters useful in representation and description, statistical texture features are calculated from the attribute extraction techniques namely IBF, GLCM, SGLDM, GLDS, NGTDM, SFM, Laws TEM, FDTA, FPS. For selecting only useful attributes, mRMR feature selection technique is employed in this work. The developed classification module is conducive to radiologist and neurologist by assisting in in decision making and treatment planning.

Thus, in brief the overall contribution of present work was the development of interactive and efficient model formulation for early and accurate recognition of three most commonly occurring abnormalities, accentuating death incidences.

CHAPTER 2

LITERATURE REVIEW

2.1 Introduction

The present chapter gives a broad overview of different literatures published globally on segmentation, extraction and selection of features, and finally classification of images of lesions on the MR images. Processing of images is being done all-round the globe in the different fields like detection of facial expression, medical support system and forensics. The above technique is widely used for diagnostic purposes because of its advantage of being a non-invasive computer assistance-based method. Image processing is widely used in medicine tissue discrimination in-between normal and abnormal tissue holds important diagnostic value.

The process of partitioning an image into separate regions with similar attribute bearing pixels is called as Image segmentation. With image being just an object replica, its described as 2-dimensional function $I(x, y)$ where both x and y are spatial coordinates and ' I ' is the amplitude of coordinate pairs which is known as grey level or intensity value of image at that particular point. The basic goal of segmentation is to simplify or /and change the image in a form which is more easily analysable. On the basis of significant features of image like, pixel intensity, texture, color etc various segmentation techniques of images have been developed. For the detection of brain anomaly, quantitative analysis (feature extraction followed by classification) plays a pivotal role, giving computer assisted diagnostic help to the neurosurgeons. In the process of quantification, various image processing steps are applied which include enhancement of image, segmentation of lesions, feature extraction and selection and then finally classification of the lesion based on the results of above steps. Noteworthy works done in area of image segmentation, feature extraction, feature selection and classification methodologies, are illustrated in following section. A systematic assessment of the above provides overviews of all the evidence currently accessible on particular topic of interest and allows the researcher to explore the potential of computer assisted system designing for the detection and classification of brain lesions.

2.2 Image Segmentation Methods

Image segmentation of brain lesions can be done manually or through computerized algorithms automatically or semi-automatically using different contouring techniques. Manually partitioning in itself is a tedious error prone task. Also, there are numerous constraints which are

faced during automatic segmentation of brain lesions using real time clinical dataset, for instance: problems related to defining metric, the unavailability of standard regulated protocols, time-consuming process of data collection, lack of definitive gold standard etc. Moreover, the task of automatic segmentation in MRI data consisting artefacts further leads to missing of boundary because of dependence on orientation of the acquisition. These artifacts in the MR images predominantly lead to the failing of many robust automatic algorithm. Additionally, the radiologist who were directing the present work were inclined in developing a segmentation and classification system which will segment and classify the pathology if the rough marking is done by them.

Brain lesion segmentation means delineation of the abnormal tissue from normal brain tissue. In the tumor cases, it implies segregation of the tumorous tissue and healthy parenchyma. It is amongst the most important steps in the medical imaging and also assists to the planning of the surgical or non-invasive treatment. Malignant tumors have a lot of variation in physical appearance like size, shape or texture as well as on the basis of location and intensity. In a similar way infarcts and hemorrhages exhibit different characteristics and are classified based on the time of evolution, location and aetiology of hematoma. Several textural analyses of brain lesions have been done. MR images of brain abnormality provides the information about texture in form of gray tones distributed spatially [39]. The texture change can also be the result of some underlying disease which is progressing with time. This makes texture attributes to be an important criterion for obtaining clinical information of the abnormalities e.g. hemorrhage, tumor, infarct etc. and also further helps in segmenting the anomalies of brain [40]. Lots of research have been conducted on the textural analysis of brain. Most of these studies cater with segmentation of the tissues of brain as gray matter (GM), white matter (WM) and cerebrospinal fluid (CSF) on the MR images. Several authors have also provided good results for delineation of normal tissues of brain [41-44]. Zadeh et al. [44] segmented normal parenchymal tissues as WM, GM, CSF, muscle by the use of Euclidean distance. It noticeably segregates the abnormal tissues from the healthy ones by making similar tissue groups. Algorri and Flores-Mangas [41] coupled classifier knowledge base of semi-automatic method with the Fuzzy Indexing for the segmenting the brain structures using spatial specifications of brain. A similar study was done by Leemput et al [42] for the segmentation and classification of the brain tissues. Markov random fields were also used for the segmentation of single and multispectral images. By this technique, the inhomogeneities present in the Brain MR signal is also gets rectified. Although, all the above

discussed methods are used to segregate the normal and abnormal tissues on the basis of similar textural pattern, but, odema and lesion segmentation still is a demanding task.

Segmentation of brain lesion can be done via two modes: automatically and semi automatically. For the automatic segmentation of pathology and odema, very limited techniques remain available. Automatic techniques used for detecting, segmenting and classifying the brain tumors are region growing based approaches [45-48], fuzzy c-means clustering [49-51], ANN techniques [52,53], watershed-based approaches [54,55], atlas-based techniques [56-58]. Fletcher-Heath et al. [51] used Fuzzy C- Means (FCM) clustering along with previously acquired knowledge base for the brain MR images tumor segmentation. Many authors have applied segmentation algorithms to the MRI of brain tumors in 35 to 36 slices. Although this technique works well for large sized tumors, small sized ones are not properly segmented or sometimes missed as it requires the tumorous regions appearance in minimum three successive slices. Liu et al. [59] used Fuzzy connectedness theory for segmenting and further measurement of the volume of the lesions. The only shortcoming with this method is that it needs input data in the form of information for the location of the lesion. For the breast cancer cases, neuro fuzzy algorithm which is based on convex set was advocated by Grohman et al. [60]. The usage of supervised k-Nearest Neighbour (k-NN) method and automatic Knowledge Guided (KG) method was proposed by Mazzara et al. [61] for segregating brain lesions on MR images. The segmentation accuracy of k-NN method was 56% while that of KG method is of 52%. Prastawa et al. [57] used Atlas as geometric before brain tumor and odema segmentation. Lerski et al. [62] used texture analysis for analyzing MRI of brain tumor. Mahmoud-Ghoneim et al. [63] conducted another tumor textural analysis by the use of 3D co-occurrence matrix. Both authors discussed above have reported very high specificity and sensitivity. However, it's worth noting that volume of tumor was manually marked in all these methods. Pachai et al. [64] used multi resolution pyramid algorithm for the segmentation of multiple sclerosis lesions on brain MR images. On comparing the same with manual methods of segmentation, this method has proven far better reproducibility and morphological accuracy. Textural analysis was suggested by Pitipot et al. [65] for segmenting the caudate nucleus, hippocampus and corpus callosum by the use of hybrid neural classifier. FD or fractal dimensional analysis is done for the acquiring the information related to texture and roughness of surface from medical images. This technique was also used for studying the shape of lesion or the change in size of the lesion in the brain's cortical region [66]. Brain tumor images were generally segmented by the usage of fractal models [67-69]. The segmentation of the width of Glomerular Basement Membrane (GBMs) was done by

the use of edge detection, morphological image processing, skeletonization, modelling by statistical approaches and active contour models as proposed by Rangayyan et al. [70]. He also further analyzed the pixel resolution effect on the calculated texture features by the use of Grey Level Co-occurrence Matrices (GCLM) during the process of differentiation of monographic breast lesions in groups of malignant or benign tumors. Intuitionistic fuzzy set (IFS) proposed by Chaira and Anand [71] was used to highlight the hemorrhage/tumor area boundary for enhancement and detection. Joshi et al. [72] proposed maximum likelihood criterion of the Bayesian network. Because of the availability of priori information about the parameters Bayesian model convergence is faster in comparison with others. Kumar and Gupta [73] proposed the approach of probabilistic networks for segmentation where image sequencing was studied through moving objects.

For MRI segmentation especially involving abnormalities of brain various researchers had used semi-automatic techniques too. A majority of these researches had used Parametric Active contour methods [74-77]. Fluid Vector Flow (FVF) was applied by Wang and Cheng [76] for segmentation purposes. In this process the flow of the fluid is energised towards the object boundary, thereby, producing the external force field for carrying out the contour evolution. Although this model gave promising results on post contrast T1-weighted images of tumor, it was not successfully tested on different intensities of T1, T2-weighted images. Further, it required interactive threshold selection which has fair chances to fail in complex images of lesions. As this method is not very object specific it may locate wrong object on encountering binary objects, hence missing the real target. Modified contour model was proposed by Dakua and Sahambi [78,79], in which automatic selection of seed was done and the Laplacian of difference of Gaussian weighting function was used for segmenting left ventricular myocardial wall on the heart MRI. Level set active contour models usage has been envisaged by various researchers [80, 81]. It has been found that the semiautomatic methods give more accuracy in comparison with the automatic methods because of the initial manual marking of area of abnormality (initial region of interest). The search area reduction caused by manual intervention helps in further locating and segmenting the brain lesions with greater accuracy. Some of researches which were of similar nature were done by the use of parametric and geometric active contour modelling for detection of homogenous anomaly (tumor) are discussed in the trailing paragraphs.

Previous segmentation approaches done globally were mostly directed on similarity and discontinuity criteria. Watershed transform, thresholding, region splitting and merging, region growing are few approaches which segment via looking into the similarity of the pixels while

methods based on detection of edges came under the approaches which follow the discontinuity criteria. [82, 83]. Image thresholding is one of the traditional methods where the image is divided into foreground and background. This technique is fully based on the choices of the gray values [84]. Though it is easy to apply, its performance is sightless i.e. it blindly dives image on the basis of chosen threshold and is indifferent towards another critical attributes of the image and hence it is very susceptible to image artefacts and noise causing improper segmentation. Clustering methods [93, 86] such as fuzzy c-means (FCM) focus on partitioning given set of objects within the given set of clusters. Although, it retains much more information, but information related to spatial domain is not considered which gives it sensitivity towards noise and artefacts. Many improved versions of FCM were later developed like Bias corrected FCM (BCFCM) which includes the spatial information too, thereby giving better segmentation results [87]. However, it is a very computationally ineffective approach and so to for mitigating this issue, kernel FCM was introduced which uses kernel for distance by the modification of the cost function of BCFCM [88]. Several other different parameters were used in the other improvised techniques like FLIFCM, GKFCM, NMFCM [89-96].

In other state of art approaches, the spatial relationship amongst the pixels is used for the purpose of segmentation and are known as spatially guided approaches. These are basically region based (region splitting and merging [97, 98], region growing, hybrid approaches) or the energy-based approaches (active contours, graph-based, watershed techniques, marker-based watersheds etc.). The region growth process starts at the pixel level, and at each step the same type of pixels merges one by one and continues until no more identical pixel elements are left to be added. It works on growing the seed via homogeneity principle, but it can sometimes face the problem of over-segmentation [99-104]. However, watershed approaches use image morphological attributes i.e. exploiting both region and the contour information for segmentation [83, 84]. It has rather simple and easy style of partitioning achieving complete segregation, but in this case also over-segmentation issue is still a challenging task to deal [105,106]. Also, it is highly noise sensitive. Its hybrid variants were introduced by the authors which involves the synergistic effect of both region merging and morphological attributes, in order to deal with the noise related problems [107-112]. The unique qualities of wavelet and watershed transform were used for segmentation of 2DE gel images by Sengar et al. [109]. They also removed the shortcomings of watershed transform by utilizing the spot characterization in wavelet domain. Each watershed county has its own connected set of maxima which was introduced and then computed in the wavelet domain. Dynamic curves like active contours uses criterion of energy minimization. These can be basically categorized in two types: geometric or parametric based on

their implementation [84]. These are adept framework envisaged by Kass et al. [113] for marking objects in 2D images containing considerable amount of noise. However, the main issue associated with this model is problem encountered during initialization and poor convergence in noisy images. Also, it is very sluggish process. In order to resolve this problem, the modelling of propagating curves was done at particular levels of high dimensional surface. Osher and Sethian [114], did the modelling of the evolving curves at specific levels of the higher dimensional surfaces for overcoming the limitations faced by the snake model. The surfaces are dynamic in nature which can evolve with time taking the requisite shapes. These surfaces called as the level set function (LSF) which has a middle front being known as the zero-level set. Malladi et al. [80] in 1995, employed the same levels set techniques for shape recovery which were proposed by Osher and Sethian. Gong et. al. [115], introduced the hybrid level set technique for increasing the robustness of the system by including the shape constraints during the region-based contour progression. Active contour model with the level set formulation, is further classified as edge-based approach and region-based approach. Level set models based on edge detection utilize image gradient of a given image to stop and evolve the curve.

Geodesic active contour (GAC) models are the most accepted type of edge-based segmentation methods utilizing a balloon force term along with the edge based stopping term where the regulating the motion of the curve [74, 117-118]. However, the task of drafting the balloon force is very difficult. Also, it has shortcomings like sensitivity to noise and problem in curve initialization. The traditional level set approaches give birth to the irregularities in the course of evolution of level set function. However, these conventional approaches governing factor is to keep the moving curve close to the signed distance function [119,120]. For better segmentation and a stable curve movement, lots of researchers have re-initialized LSF regularity parameter though this process is also not error free. Occasionally, it moves the zero LSF away from the accounted place [118,120-122]. Li et al. [119] presented a variational formulation for Geodesic active contour with a penalty term for mitigating this problem, which works by pushing the LSF close enough to signed distance function. This method adequately removes the periodic re-initialization procedure of LSF during the process of evolution taking into consideration that the variational energy function is a unification of two terms which are the internal and the external energy term. Here the internal energy term penalizes the LSF deflection to a pre-assigned distance function whereas the external energy is used for the motion of zero LSF to the desired position. However, some side effects which were produced on the level set function due to the penalty term which can reduce the accuracy of segmentation. Additionally, Li et al. [123] improvised their prior method by introducing a different distance regularization parameter along

with an external energy term, which drives the contour movement towards the expected position. The need of re-initialization was completely removed due to the involvement of this new distance regularizing term, and also helps to avoid the undesirable effects brought by the penalty term.

Besides edge-based active contour models, region-based models try to detect each region of interest in the given image by combining the region-based information into their energy functional. These models have been found to be superior to the edge-based active contour models and their advantages are unrestricted position of the initial contour, automatic detection of estimated boundaries as well as effective segmentation because of global energy minimization based on statistical properties inside and outside the evolving contour on which it evolves the deformable shapes and keeps the regularity of the active contour. Chan and Vese [124] introduced region based active contour model and named it as CV model used for segmentation purpose based on the Mumford and Shah Model [125], to extract the object of interest where gradient is unable to detect object boundaries. The CV model provides better performance than the GAC model because of its nature to acquire a large convergence rate. Though, image segmentation using the CV model depends on the placement of initial contour. If the contour is improperly initialized, various outcome could be obtained using different contours selection in an image. To overcome this limitation of the CV model, many researchers [126-130] have tried to introduce some efficient techniques. Solem et al. [127] proposed the initialization methods for contour which is estimated using a search method which is also a time engaging process and often fails during the small difference between the object and its background. In [126], initializing curve is generated by iteratively joining edge points estimated by the canny detector and morphological filter, while in [129, 130] these schemes are introduced without solving the PDE's. However, these are still sensitive to initialization of contour and noise. Further, Li et al. [131] presented a variational level set formulation for segmentation of image that is based on the regularization function and region scalable fitting (RSF) energy function. The RSF function obtains information relating to intensity of the local regions at established scale in order to estimate the two fitting functions and forces the contour towards the estimated boundaries of the object. The regularity term available in this model is used to control the length of the object boundaries and prevents the over-segmentation. Currently, several researchers [132-134] tried to utilize these methods for the US image segmentation purpose. Generally, external interference and technical limitations lead to intensity non uniformity. The images having intensity non uniformity and requiring correction of the bias field were interleaved segmented in [135]. Moreover, Zhang et al. [136] presented another region-based active contour model that utilizes both the features of the GAC and the CV model. In this approach, signed pressure function has

been used instead of edge stopping function to control the direction of the curve evolution. Several quantitative evaluations have been performed on this approach and it has been reported that it performs better than the conventional level set methods.

In another graph-based model [137] used for image segmentation, firstly graph is constructed by considering each vertex corresponding to a pixel in the image and the edge connects the pixel to its neighbour. After constructing the graph, the different sub-graphs of similar intensity levels are now merged and produce larger graph. Finally, by repeating the merging process, an image is segmented into the larger homogenous region. It produces better segmented images with higher accuracy; however, it is sensitive to the parameter selection. [138]. Nguyen and Wu proposed different mixture model by incorporating neighboring pixel spatial information into Gaussian mixture model. Their model based on Markov random field (MRF) proved to be fast and computationally inexpensive [139]. Similarly, Ajaz et al. proposed use of morphological filters in combination with image enhancement techniques for automatic segmentation of IR-SLO fundus images. Firstly, they applied morphological filters for contrast and then successively applied Contrast Limited Adaptive Histogram Equalization (CLAHE) along with Bilateral filtering for background exclusion and finally used Isodata technique. The model's average accuracy compounded to be of 0.90 [140]. Mishra et al. [141] proposed the scheme for detection and multi-person tracking based on their color appearance on real time videos using active contours and Gaussian Mixture model (GMM). Segmentation and blob analysis of each frame was done using GMM and active contours. The color moments and structure tensor features of every individual in FOV were extracted to compare similarity features among tracked person. Their algorithm showed potential in case of harsh environment as poor illumination, partial occlusion or when the moving target becomes static thereby tracking and identifying it. Gerig et al. [142] proposed the use of ITK-Snap software tool for 3D and 4D imaging datasets for semiautomatic segmentation of anatomical structures of interests by specifying the pathology as foreground and healthy tissue as background and using these locations in image as a training data in supervised random forest machine learning algorithm.

After the foreground/background probability map is created, deformable contour is initialized within the structure of interest manually which evolves until the full segmentation is complete.

In the current research work only, region based active contour models are considered to implement the proposed approaches.

2.3 Feature Extraction Methods

Feature extraction is a significant step in texture classification. Features aid in discriminating the brain lesions regarding their specific textural pattern and intensity, during the classification of brain anomalies. In the previous chapter, brain lesions (hemorrhage, infarct and tumor) along with their identification criteria on MR images have been discussed.

Due to the intricacy of the structure of brain and further complexity arising as a result of mimicking nature of the brain abnormalities on MR images, there is a requirement of useful feature extraction which are not redundant among themselves i.e. they are not correlated. For using feature as a discriminant, all the features must have large variance. Radiologists use textural homogeneity/heterogeneity or iso, hypo and hyper intense criteria for visualization of any brain anomaly as well as a measure for differentiation between different brain abnormalities. These visually extractable features prove as a guiding principle for finding the best suitable mathematical feature descriptors for developing the computer aided diagnostic system (CAD) to differentiate between various brain lesions. In brain MR Imaging, intensity is the key feature for discrimination of different types of tissues. Nevertheless, for the classification of brain lesion using the intensity alone, is not sufficient [143-146]. If the features are not discriminative enough, even the best classifier cannot provide good classification accuracy. The feature extraction techniques should be able to capture inter-class variations and at the same time, minimize the effect of the intra-class variations. Several studies have been reported in literature and feature extraction is an active area of research. Numerous mathematical descriptors used are textural features, intensity-based features, shape based and morphology-based features etc. There are various feature extraction methodologies which are discussed in the present literature review, and the same have been applied in the current research as well. As we are aware that not all the features are significant, we retain only those features having significant discrimination capability for the differentiation of tissues with brain anomalies (e.g. hemorrhage, tumor etc.) from the normal tissues.

The structural alterations present in the tissues can be easily detected by histological examinations but sometimes cannot be visually inspected from the image of tissues. In these cases, texture analysis plays a critical role in discrimination and classification problems [147-154]. Different categories of statistical approaches based on the texture properties of an image are described by Castellano et al [40]. Tourassi [148] referred texture as an affluent source of visual information which can be effectively described by statistical and spectral properties of radiologic images. Accordingly, texture analysis has prospects to enhance the visual expertise of

radiologist by generating features which are not visually implicit and thereby increasing the information content of the routine diagnostic practice. This added information may be apt to the diagnostic problem in hand. For the texture analysis various feature extraction techniques have been devised and used in [149]. Generally, an ensemble of mathematical operations is performed on the data of the image in an attempt to extract a unique set of useful features. Further, a lot of studies have been done to quantify the microscopic texture pattern possessing important clinical information in order to classify between healthy and pathologic brain or to differentiate the type of lesion in the brain [150,151]. In the marked ROI (region of interest) of the medical image, areas of same texture have uniform features [152]. Chatterjee et al. presented various feature extraction techniques like shape and contour-based techniques like contour signatures, localized contour sequence features, moment features etc. for static hand gesture recognition system. To overcome the same shape gesture misclassification problem, they presented zoning based feature extraction methods [153].

The feature extraction techniques which are most widely used in practice are spatial grey dependence matrices (SGLDM) also known as gray level co-occurrence matrix (GLCM), edge frequency, autocorrelation function, local binary pattern, texture unit and spectrum, fuzzy texture unit and spectrum. GLCM approach proposed by Haralick et al. [39,155] has been generally used by numerous researchers. Different grades of Astrocytoma tumors were classified by Glotsos et al. [156] made use of GLCM matrix along with run length matrix for classification of lesions. Selveraj et al. [157] separated normal and abnormal slices by extracting GCLM image features. Wavelet and GCLM features were extracted by Kharrat et al. [158] to differentiate between normal tissues from malignant tissue. Deepa et al. [159] successfully performed similar work to discriminate normal and abnormal MR image using GCLM with accuracy close to 95%. Further, Zarchari et al. [160] classified different types of brain tumors by applying GLCM, intensity-based features, Gabor texture features and statistical and shape-based features. In the research done by Georgiadis et al. [161,162] total of 36 features were calculated from histogram, GLCM and run length matrix. Ultrasound visual features of focal liver lesions were extracted by Kim et al. [163] and then correlated these images features with radiologists grading. They concluded that there is a good agreement between their algorithm results based on textural features and radiologists visual grading.

Over the past few decades, increasing number of textural features have been introduced and incorporated in various ongoing works. Sheet et al. [164] proposed a method named Brightness Preserving Dynamic Fuzzy Histogram Equalization (BPDFHE) for adjustment of

brightness preserving dynamic histogram equalization technique for its improving brightness preserving and increasing contrast while reducing the computation complexity. This method uses fuzzy statistics of digital images for the processing and representation of digital images. Local texture of micro calcified area of interest was represented by wavelet decomposition-based features and the global texture of the area was represented using statistics-based feature by Dhawan et al. [165]. The other relevant features used are size, number, distance of segmented micro calcification clusters and the first order grey level histogram-based statistics of segmented micro calcification regions. Wavelet Packet transform (WPT) was used by Khare et al. for feature extraction of relevant frequency bands from raw EEG (Electroencephalograph) signals for classification of five mental task [166,167].

Ojala et al. [168] introduced local texture descriptor named as Local binary pattern (LBP) which is effective for textural classification with low computational complexity. Its other attractive properties are rotation invariant, robustness against monotonic gray level transform and low computational burden. The uniform local binary pattern (LBP^{u2}), rotation invariant local binary pattern (LBP^{ri}), and rotation invariant uniform local binary pattern (LBP^{riu2}) are the extension of original LBP with its reduced dimension of feature vector. LBP has proven itself superior in several comparative studies and has been extensively used in large number of fields like in medicine, face recognition, biometrics etc. [169-172]. In the medical field LBP is used to identify malignancy in the breast [170] and finding brain MR volumes relevant slices [173]. Superior local binary patterns have been checked out to capture descriptive textural information [174].

Transform domain feature extraction technique like gabor transform, discrete wavelet transform is utilized in the classification framework. Since gabor filters are orientation and scale tunable detectors, these filters are largely being used as a feature extraction technique in medical image analysis [175]. Basically, gabor filters are wavelet collections with each wavelet collecting energy at a particular orientation or direction and at a particular frequency. Gabor function has found a widespread usage due to its optimal localization characteristics in both spatial and frequency domain and is therefore recognized as a useful textural analysis tool. Various supervised as well as unsupervised segmentation and classification approaches has been devised by several authors using DTCWT, banks of Gabor filters with different orientation and scale tuning [176-181]. Kyperountas et al. [176] analyzed Gabor features for facial expressions. In a comparative study Manjunath and Ma [182] demonstrated that image retrieval via Gabor features gives better results than multi-resolution simultaneous autoregressive model features, pyramid-structured wavelet transform features and tree structured wavelet transforms features. For image

retrieval, Zhang et al. [181] extracted Gabor features from textured and natural images and then calculated mean and variation of Gabor filtered image. Another study was undertaken by Rama Krishnan et al. [183] for extraction of various textural features using of Gabor Wavelet, wavelet families, local binary pattern, Brownian motion curve and fractal dimension from epithelial regions of tissue section. They concluded that bior 3.1 wavelet coefficient gives higher accuracy of 88.38% in combination with Gabor wavelets and LBP and it was suggested that the combination of more than one texture measure can improve the overall efficiency. Herlidou et al. [184] conducted textural analysis using the statistical domain feature extraction techniques such as histogram, co-occurrence matrix, run length matrix, gradient matrix for the study of skeletal muscle dystrophy on MR images. Murala et al. [185] proposed local ternary co-occurrence patterns (LTCoP) as a feature extraction method for biomedical image retrieval. The co-occurrence of similar ternary edges present in an image were encrypted by LTCoP. The ternary value was calculated for different thresholds to analyze the performance. To prove the effectiveness of proposed rotation invariant algorithm, it was compared with the LBP, the LTP and the LDP on three benchmark biomedical image databases. The outcome showed its potential over existing methods in terms of precision, recall, average retrieval rate (ARR) and average retrieval precision (ARP).

The complexity of the present work lies in the fact that it involves the study of the major brain anomalies - Tumor, Stroke and Hemorrhage which have overlapping visual characteristics on the MR images. Hence, there is the need to exploit of entire range of discriminating power of available datasets to develop much more efficient structures. The literature given above discusses several techniques of intensity and textural analysis. The method of feature extraction is selected based on the literature study and by consideration of all diagnostically important features for brain anomaly classification on MR imaging to obtain high classification accuracy.

2.4 Feature Selection Methods

Feature selection methods play a very crucial role in any classification module. Feature selection techniques helps in identification and selection of discriminative (informative) features for data interpretation, thereby improving the overall classification performance in order to buildup of a better system. These techniques reduce the computational cost of the system by reducing dimensionality of data. A feature set is normally composed of several groups of features. Different combination of these features may receive different classification accuracy and garbage (noise) feature may appear in each group. Feature selection eliminates the unimportant features to obtain the optimal finest subset of features that discern well among

classes. Hence, after application of the best suited feature selection techniques, the overall prediction performance increases significantly, further increasing the comprehensibility of the proposed models as the irrelevant and redundant features as probable noise are removed. It can be differentiated from feature generation as in the latter case, new features are created by the combining the original features, however, in feature selection process the true meaning of selected features is maintained as in some they are desirable in their original form. Adaptive optimization search methodologies for machines learning techniques such as Genetic Algorithms (GA), Principal Component Analysis (PCA), minimal Redundancy Maximum Relevance (mRMR) are generally used for selecting optimal features from the given input feature set. Genetic Algorithms (GA) works with a batch of candidate solutions called as population. GA is based on survival of the fittest principle, generating alternative solutions to the successive populations until acceptable results are obtained. The result quality is dependent on fitness function which in turn rely on appropriate selection of crossover rate and mutation rate. The chromosomes having greater fitness value are more probable to get selected for reproduction through roulette wheel method. In this way GA reduces feature set which helps in increasing the SVM classification accuracy, as only the healthier and fitter chromosomes are selected. Li et al. [186] combined bands optimally by GA-SVM and irrelevant bands from the output were pruned by bound search algorithm (BB) in order to get a minimal set of relevant band for classification task. Genetic programming (GP) was used for cancer diagnosis by extracting features through modified Fisher linear discriminant analysis (MFLDA) and thereby classifying with minimum distance classifier [187]. Similarly, Raymer et al. [188] proposed GA to use it as feature subset selection framework and as vector optimization for feature weights. In [189] Jack and Nandi used ANNs overall generalisation performance was improved through the use of genetic algorithm based feature selection process.

PCA is another dimension reduction statistical technique, in which the correlated eigen vectors are orthogonally transformed and then projected onto the subspace covered by those eigen vectors concurring to the largest eigen values. In this conversion the signal components are de-correlated in such a way that the projection to the high variance direction maximize the variance and minimize the mean squared residual in-between the original signal and the dimension reduced approximation [38]. Application of PCA technique benefits in consumption of less memory for creating training set and low noise sensitivity as it retains high variance components and discards small variation, while its specific disadvantage is the dependency on linear data [191]. To overcome this, Buchala el al. [192] proposed nonlinear projection method

known as curvilinear component analysis (CCA) which outperforms PCA with much lesser components. Zhang et al. [193] utilized DWT technique to extract features and thereby dimension of the features were reduced by applying PCA. Dimensionality of the search space of prototype images was reduced by the proposed use of PCA by Sinha and Kangarloo [194], which best describes the subject image. They compared projection of vector images on a given dataset with that of database images of T1-weighted MR images. Different approaches have been introduced by several authors for relevant selection of features from the feature domain by using PCA in medical image database [195,196]. Kumar et al. [197] presented class specific feature selection method in which the features having smaller variance get selected. This method showed significant improvement over the classification accuracy, sensitivity and specificity.

Several authors have used the minimal redundancy maximum relevance (mRMR) for feature selection as per their discriminative properties [198,199]. Niaz et al. [200] proposed a CAD model using support vector machine (SVM), k-nearest neighbours, linear discriminant analysis along with naïve Bayes classifier for prostate cancer on magnetic resonance imaging (MRI). Furthermore, feature selection methods constructed on mutual information, t-test, and mRMR criterion; were compared. Ding et al. [201] proposed a CAD system for thyroid histograms using the statistical and textural features and then the most effective and reliable features among them were selected using an mRMR algorithm. Gomez et al. [202] investigated the co-occurrence statistics in addition with six gray scale quantization levels to classify breast lesions on ultrasound images. To reduce feature space dimensionality, the feature space was graded by the use of mutual information technique with mRMR criterion.

2.5 Classification Methods

The final stage of every CAD system is the design of a classifier which aims to acquire knowledge of the extracted features in order to assign the group or severity label to the given test samples in accordance to the problem stated. The focus of classifier is towards assigning new data object represented as input features to one of the possible classes with a minimum rate of misclassification. A classifier constructs a partition/boundary on learning by examples. Basically, the methods adopted by the classifiers are categorized into two groups: Supervised classification and un-supervised classification. Supervised classifiers procure guidance at the learning stage than compared to the unsupervised classifiers. The accuracy of the supervised image classification is a function of training data used in its generation. Jain et al. [38] outlined that selection of classifier is a difficult task and it depends on either availability or the knowledge of end users. Therefore, researchers have availed various classifiers such as support vector

machines (SVM), Artificial Neural Networks (ANN), ada boost, K-nearest neighbor (k-NN) and random forest (RF), linear discriminant analysis (LDA) etc. [204-209]. These systems have demonstrated the capacity of performing the task with reasonable performance parameters such as classification accuracy, sensitivity, specificity, and computation time using texture features. The diverse strategies proposed for various ailments have considered the MRI, CT scan, US, and other modalities to acquire the dataset.

Brain lesion classification has been considered as one of the toughest tasks because of the huge variance in the subject of study. Heterogeneous texture of the brain lesions and the issue that some lesions don't enhance at all, causing their misclassification as normal region are some of the major issues faced. The complications are further enhanced, increasing the difficulty of classification when infiltration of lesions occurs in the normal brain parenchyma. Few lesions show mixed characteristics mimicking other pathologies.

Christodoulou et. al. [210] proposed an approach for characterization carotid plaque into two categories namely symptomatic and asymptomatic, utilizing ten different texture features sets named FOS, SGLDM, GLDS, NGTDM, SFM, Laws TEM, FDTA, FPS and shape based parameters. On the basis of these features they proposed two classifiers: modular neural network composed of self-organizing map (SOM) and k-Nearest Neighbour (k-NN). Cortes et al. [211] introduced support vector network to the inseparable training dataset. Support vector machines non-linearly maps input vectors to a very high dimension feature space and constructs a linear decision surface. These networks have high generalization ability to be utilised in any domain. For the brain tumor classification different computer aided techniques are used availing MR image sequencing or MR spectroscopy. Substantial results have been obtained by many researchers by classifying brain tumors on the basis of MR spectroscopy data [36, 212-216]. Wang et al. [215] used conventional MR imaging for discriminating between benign and malignant tumorous growths by using decision tree algorithms. Cho et al. [216] and Weber et al. [36] classified the heterogeneous and non-heterogeneous brain lesion using spectroscopic and perfusion MRI. Diffusion coefficients maps were computed from diffusion tensor imaging data and are combined with rCBV for discriminating between demyelinating lesion, primary brain tumor from other brain abnormalities such as abscess and lymphomas [218]. A probabilistic neural network is applied with nonlinear least squares features transformation method and texture features of T1 post contrast images were employed to discriminate in between primary and secondary brain tumors in [162]. The clinical grade classification of the tumor using linear SVMs by taking 15 best descriptive features was done by Li et al. [219]. In order to improve

classification performance Devos et al. combined spectroscopy imaging with standard MR intensities. However, such features are defined based on the expert knowledge and therefore are not completely automated and reproducible [85].

Methods available in literature either distinguish normal from abnormal slice [157,217] or focus on differentiating multiple classes of brain anomaly [160-162]. Selvaraj et al. [157] studied 1100 slices (267 normal slices, 833 abnormal slices) of 150 subjects. Every slice of each subject was taken up for the calculation of statistical features so as to classify them as normal or abnormal slices of brain. The normal and abnormal slice classification accuracy came out to be 98.6% and 96.1 % respectively. In a similar kind of study, El-Dashan et al. [217] segregated 10 normal and 60 pathological images from the dataset of 70 images. The abnormal images comprised of the subjects having gliomas, Alzheimer's disease, Metastatic bronchogenic carcinoma. They introduced two classifiers. The first classifier based on of feed-forward back-propagation artificial neural network (FP-ANN), provided the accuracy of 97% while the second classifier was based on k-Nearest Neighbour (k-NN) gave the accuracy of 98%. Georgiardi et al. [161, 162] proposed model of multiclass classification of different kinds of brain tumor like Gliomas, Meningioma's and Metastases using LSFT-PNN classifier in two studies. 75 images were used in the first study and achieved an accuracy of 87.5% for Metastases, 96.67% for Gliomas and 95.24% for Meningiomas. A data set of 67 images was considered in the second study where in two stage classifiers were used in order to increase the individual class accuracy. Primary and secondary (metastases) tumor were classified giving an accuracy of 95.24% and 93.48% respectively in the first stage. 100% accuracy in classification of primary tumors (Meningioma's) and 88.89% for gliomas was acquired in the second stage. Zacharaki et al. [160] performed an analogous study on 98 images of brain tumor. Balodi et al. [203] investigates the possibility to recognize the severity of MR in a classification system, utilizing statistical texture features of the regurgitant region. Two methods of classification were proposed by Jain and Sahambi [190] for normal sinus rhythm and different arrhythmias through combination of wavelets and ANN. Nandi et al. [116] proposed intelligent hybrid model FMM-RF, utilizing power spectrum and sample entropy features to classify ball bearing faults by applying vibration signals. Their hybrid model availed the attributes of Fuzzy Min-Max (FMM) neural network and the Random Forest (RF) models to evaluate the practicality on real world datasets. The outcome of the FMM-RF model indicates good accuracy.

2.6 Conclusion

On the basis of an extensive literature survey, the following conclusions have been drawn. Various automatic and semiautomatic methods are explored by many researchers for segmenting normal brain tissues and lesion on MR brain images. The presence of heterogeneity, iso-intense to hypointense manifestation of the lesion and the existence of edema around the lesion increases segmentation complexity. Also, due to intensity inhomogeneities, low tissue contrast and weak boundaries, detection of these lesions become a difficult task. Normally subjective variations exist in radiologist marking due to human experience and error. In the present study, a modified segmentation method is proposed using both texture as well as intensity information which can segment heterogeneous, homogeneous or diffused lesions on T1 and T2-weighted MR sequences.

There is a comprehensive literature for feature extraction methods where the texture-based methods are revealed to be most suited for the present classification studies. Intensity and texture provide relevant features in this study involving brain lesion imaging. Six widely used feature extraction methods from these approaches are used for the present work. Feature selection procedures are extensively performed using mRMR and PCA. An exhaustive literature is available on feature selection techniques. Feature selection methods are implemented separately using these approaches for optimal feature selection. The literature surveys reveal that there are very limited studies which separate normal and abnormal slices of brain MR images. Also, there is limited reported literature for the classification of different kinds of brain lesions such as hemorrhage, infarct and tumor using MR images. These pathologies often mimic each other with other lesions as their signature attributes to differentiate with each other are not dominant enough. They can be iso-intense to hypo-intense in nature. Normal regions (NR) represents extremely varying anatomical regions. Due to human ambiguous perception, every now and then normal regions are sometimes misclassified as lesions. Accurate lesion prediction depends on the experience and expertise of radiologist and has subjective variability. Therefore, to remove ambiguity and reach the firm decision classification methods are proposed to assist radiologist in decision making process for multiclass brain lesion classification. It was observed that both ANN and SVM classifier have been used in medical studies prove good classification accuracy. An attempt has been made in the present work to use the ANN based classifier in order to design a CAD system for the least treatable brain pathologies if diagnosis is not done speedily like hemorrhage infarct and tumor.

2.7 Objectives of the Present Study

The main objective of present study is to develop separate methods in order to assist the creation of better CAD system for identification of three most commonly occurring abnormalities, accentuating death incidences. It has been recognized and emphasized time and again that early and correct segmentation as well as classification of ROI can reduce casualty caused by these emergency conditions. This research work is conducted on brain fatalities which includes brain stroke, infarct and tumor. The main objectives can be stated as:

- 1) Development of MR stroke, brain infarct and brain tumor image database.
- 2) Design, development and implementation of semi-automatic system (with minimum intervention) to help radiologist by supporting them with an interactive, efficient and robust segmentation tool for heterogeneous, homogeneous, or diffused pathology (stroke, brain infarct and tumor) on basic MRI sequences (T1-weighted, T2-weighted).
- 3) Implementation of feature extraction methods for acquiring intensity and texture-based features on routinely taken T1 and T2-weighted images. Application of feature selection method for removal of redundant features.
- 4) Designing, implementing and evaluating the classification module for hemorrhage, brain infarct and brain tumors by analysing routinely taken T1 and T2-weighted MR images so that it would assist radiologist and neurologist in decision making and treatment planning.

CHAPTER 3

METHODOLOGY

3.1 Introduction

The modus operandi of research is to specify and frame a problem statement in order to get its solution. Thus, research methodology is the blue print that represent the intended path to be followed to meet the objectives that have been set. It comprises of the crucial steps such as the collection of data and implementation of existing and newly proposed techniques for the accomplishment of various set objectives. In research area that involves human subjects, proper ethical principles need to be attended while collecting the data for human samples. For this the prior consent of patient must be taken.

Although MR images of brain furnishes evident visualization of the brain anatomy, yet the insight picture details of small lesion are not very clear or definite. Computer Aided Diagnosis (CAD) system is an alternative solution to assist the diagnosis process. Consequent problems related to identification of lesion on MR images are being dealt in this work which are: changes in lesion orientation relative to patient posture, inadequate segmentation of homogeneous, heterogeneous and diffused lesion bearing weak and false edges; and classification of lesion. For that purpose, this research work is basically directed to develop a CAD system constituting segmentation and classification algorithms for identification of abnormality on brain MR images thereby aiding the radiologists in decision making process. The present chapter gives the details of the protocols and the dataset used in the present study. To meet the research objectives discussed in Section 2.7 of Chapter 2, research methodology is designed as presented in Figure 3.1. The stepwise procedure of the methodology is explained in the following sections.

3.2 Acquisition of Data

The primary step involving any research work is the acquisition of the image dataset. This research is oriented towards aiding in identification of three most common types of leading abnormalities causing the rising incidence in mortality among adults and children. After much survey the choice of diseases shortens to brain tumors, brain hemorrhage and brain infarct.

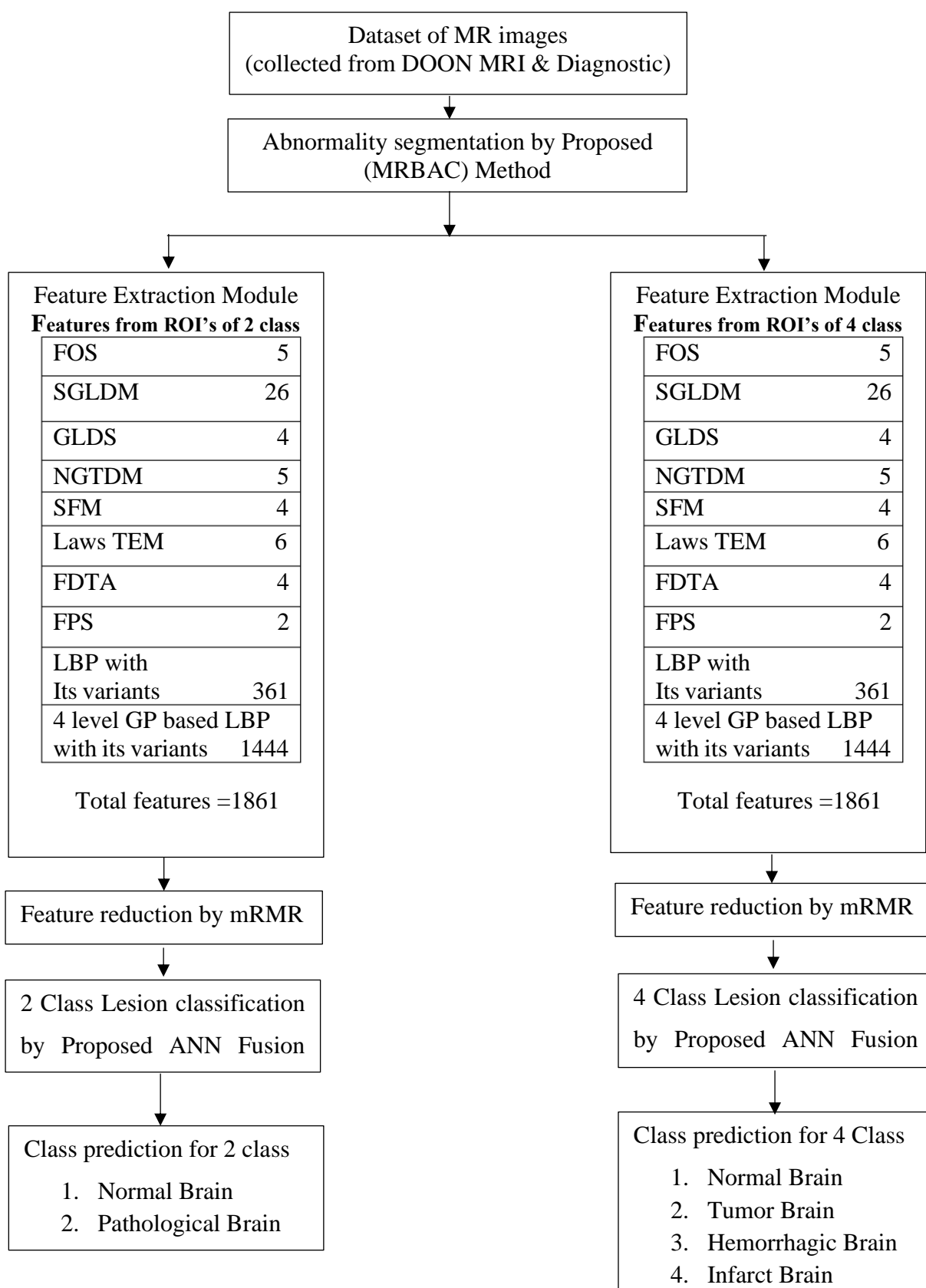


Figure 3.1: Research methodology

The clinical dataset was obtained from DOON MRI & Diagnostics, a private hospital located in Dehradun (India), abiding with its ethical council agreement, assistance, time involvement and subsequent discussions with two expert radiologists for assisting in the problem conceptualization, data accumulation and finally validation of results.

Stringent measures have been taken in maintaining the confidentiality of the patient's specific medical details. Before the acquisition of MR images, patient's approval has been taken. The preparation of database is one of the main difficulties as it depends upon the frequency of the chances of the patients of specific brain diseases visiting DOON diagnostics for examination. Because of this, database creation takes considerable amount of time. In the current case it was more than a year.

3.2.1 Brain Image Acquisition and Assessment Criteria for DOON MRI & Diagnostic Dataset

The subjects are patients (men, women and children) who have undergone brain medical examination at the Department of Radio diagnosis, DOON MRI & Diagnostic. This study used the MR data set of 12 normal brain and 48 pathological brain in total with the segregation of patients of tumor, hemorrhage, infarct and normal. In each case, the patient's consent was taken for the use of the image for research purpose. This research work is legitimized by the medical ethics committee of the DOON MRI & Diagnostics. For each subject MR Image is acquired in three planes i.e. Axial, Sagittal and Coronal. Comprehensive screening for the collection of data in order to differentiate between normal and abnormal brain parenchyma was done on frequently used MRI pulse sequences such as T1-weighted image, T2-weighted image, DWI (diffusion weighted image) etc. All these pathologic as well as normal images are acquired from the same MRI equipment (G E Healthcare 1.5 Tesla MR Scanner) These acquired images are free from noise or any artefact and are evaluated by the radiologist for their diagnostic quality.

The brain lesions (brain tumor, brain hemorrhage and infarction) on MR images were examined by two expert radiologists to get a common opinion which may vary with individual expert due to inter observability. Brain lesion assessment criteria is described as follows:

- (a) Brain lesions are assessed on MR images by visual interpretation based on the experience of the radiologists.
- (b) Brain lesion are assessed by follow-up, clinical history of the patient and other associated findings.

3.2.2 Dataset Source and Details

As stated, the data for this study is acquired from the DOON MRI & Diagnostic for testing the developed algorithms.

Clinical dataset:

Out of 48 patients, 19 tumor, 15 hemorrhage and 14 infarct patients are collected in database. For each subject, MR Image is acquired in all the three planes which are axial, sagittal and coronal. From each patient 9-12 MRI slices are considered for study. This dataset also includes MR- T1, T2-weighted scans of a normal subject which are 12 in number. The acquisition protocol of each of them are given in Table 3.1.

3.3 Proposed Methodology

The research methodology is designed out by appropriate scheming of the experiments. The proposed work is divided into mainly into two parts, one is segmentation and other is classification. These are discussed as follows:

3.3.1 Modified Region Based Active Contour (MRBAC) for Morbid Brain Segmentation

Modified region based active contour (MRBAC) is proposed in which gaussian distributions with different means and variances are deployed to describe the local image intensities. This method address issues of intensity in-homogeneities and noise (like multiplicative noise) of varying strength. MRBAC segments:

- i. Homogeneous lesions of uniform intensity where state of art methods Region Growing method, Distance Regularized Level Set Evolution (DRLSE) methods fail to segregate lesions against analogous background.
- ii. Difficult content-heterogeneous as well as infused lesions on MR images (T1-weighted, T2-weighted)
- iii. Lesions and edema (Perilesional, Cytotoxic, Vasogenic) on T1-weighted, T2-weighted, Diffusion weighted MR images.

Table 3.1: Acquisition protocol of 2D brain tumor, brain hemorrhage, brain infarct acquired from DOON MRI & Diagnostic

Attribute Name	Brain Tumor		Brain Hemorrhage		Brain Infarct	
	2D T1	2D T2	2D T1	2D T2	2D T1	2DT2
Acquisition plane	Axial	Axial	Axial Flair	Axial	Axial T1 flair	Axial
TR/TE (ms)	$\frac{2240}{10.368}$	$\frac{5400}{110.292}$	$\frac{2004.24}{9.888}$	$\frac{5420}{110.796}$	$\frac{1899.04}{9.888}$	$\frac{3980}{87.4}$
Pixel spacing (mm)	0.4297, 0.4297	0.4297, 0.4297	0.4297, 0.4297	0.4297, 0.4297	0.4297, 0.4297	0.4297, 0.4297
Slice thickness (mm)	5	5	5	5	5	5
Flip angle	90	90	90	90	90	90
Echo train length	7	24	7	24	7	20
Bandwidth (Hz)	122.07	122.07	97.65	122.07	97.65	122.07
Acquisition Matrix	0,416, 224,0	0,416, 256,0	0,320, 192,0	0,416, 256,0	0,320, 192,0	0,352, 224,0
SAR	1.4962	1.2641	1.64.12	1.2359	1.6456	1.4471

- **Dataset Details**

For performing validation, 118 lesion boundaries were manually marked by the experienced radiologist that are considered as the ground truth segments. True positive (TP), False Positive (FP), Accuracy (ACC), Jaccard Similarity Index (JSI) and Dice Coefficient (DC) and Hausdorff Distance (HD) are calculated among the segmented regions related to the ground truth boundary and the generated segment boundary. Three sets of extensive experiments are done and compared with the state of art methods. For experiment one, 57 tumor slices have been selected out of which 26 are T1-weighted and 31 are T2-weighted images. For second experiment, 27 infarct slices have been selected out of which 12 are T1-weighted and 15 are T2-weighted images. In the third experiment total 34 hemorrhagic slices has been selected out of which 16 are T1-weighted and 18 are T2-weighted images. These images are homogeneous as well as heterogeneous in nature containing edema.

3.3.2 Development of a Classification System for Multiclass Brain Lesion Classification

A classification model is developed using Artificial Neural Network for brain lesion categorization of MR images. This framework is named as Fusion Network as it is made by assembly of 10 neural network classifiers.

Two set of experiments are conducted for classification to assist radiologists. These experiments are:

- Supervised ANN based classification CAD system in Matlab Toolbox for lesion verses normal parenchyma
- Supervised ANN based four class classification CAD system in Matlab Toolbox for T, H, I and NI.

Here T stands for Tumor, H stands for hemorrhage, I stand for Infarct and NI stands for Normal Image

For these experiments on proposed ANN based Fusion Network, dataset prepared is discussed below:

- **Dataset Details**

For first experiment, 488 MR images from database are considered for classification. The classes along with the number of ROIs are mentioned in Table 3.2. Out of 488 MR images, 230 Normal and 258 Pathological images have been taken for training and testing of neural network classifiers and proposed Fusion Network for classification.

Table 3.2: Acquisition of 2D MRI database of normal and abnormal brain images acquired from DOON MRI & Diagnostic

Name of Class	Lesion Type	Number of ROIs-488
Class 1	Normal Brain	230
Class 2	Pathological Brain	258

For second experiment, 510 MR images from database are considered for classification. The classes along with the number of ROIs are mentioned in Table 3.3. Out of 510 MR images, 176 Normal Brain, 123 Brain Tumor, 107 Brain Hemorrhage and 104 Brain Infarct images have been taken for training and testing of multiclass neural network classifiers and proposed Fusion Network for classification.

Table 3.3: Acquisition of 2D MRI database of brain tumor, brain hemorrhage, brain infarct acquired from DOON MRI & Diagnostic

Name of Class	Lesion Type	Number of ROIs-510
Class 1	Normal Image (NI)	176
Class 2	Brain Tumor (T)	123
Class 3	Brain Hemorrhage (H)	107
Class 4	Brain Infarct (I)	104

- **Feature Extraction and Reduction**

Ten existing feature extraction methods are selected to extract relevant features from ROIs. These methods are divided into 10 groups: FOS features (First order statistics), SGLDM features (Spatial gray level dependence matrices), GLDS Feature (Gray level difference statistics), NGTDM Feature (Neighborhood gray tone difference matrix), SFM Features (Statistical feature matrix), Laws TEM Features (Laws texture energy measure), FDTA

Features (Fractal dimension texture analysis), FPS Features (Fourier power spectrum), LBP (Local binary pattern) features along with features from its variants (LBP^{u2} , LBP^{ri} and LBP^{riu2}) and 4 level Gaussian Pyramid Based LBP features along with features from 4 level Gaussian Pyramid of its variants (LBP^{u2} , LBP^{ri} and LBP^{riu2}). mRMR feature selection technique is used for selecting optimal set of features and for reduction of dimensionality of data by eliminating features which have negligible role in classification.

- **Proposed Classifier**

Two types of CAD system, one is two class classifier and second is multiclass classifier, based on multiple texture features has been proposed in this present study for the classification of images. The developed CAD systems are supervised classification of pathology by ANN.

Model named as Fusion Network is developed by using the combination of ten trained artificial neural networks. First approach of classification distinguishes images into normal and pathological brain images while another approach of classification, based on supervised learning, differentiates MR images into normal, tumors, hemorrhages and infarcts images by using above calculated and reduced features.

Normal regions of brain represent highly varying anatomical regions. Non-enhancing lesions are sometimes misclassified as NIs. Therefore, radiologists suggested including NI as a separate class during development of method for classification. This is the reason for including NIs as separate classes.

3.4 Conclusion

The overview of methodology to accomplish research objectives has been presented in this chapter. Its essential constituents are design of experiment, data collection usage of different datasets to validate and test the proposed methods. The overview of the experimental design has been represented which explains the basic methodology with datasets used for the different studies. All the designing steps of proposed segmentation and classification methods for brain MR images are discussed in detail in the subsequent chapters.

CHAPTER 4

MODIFIED REGION BASED ACTIVE CONTOUR

This chapter introduces a new segmentation method for MR images with active contours. It begins with a brief review of the various segmentation approaches, followed by the methodology of the proposed approach. Both subjectively and objectively, the segmentation performance of the applied approach on morbid cerebral magnetic resonance images is verified. In addition, the last section of chapter presents a comparative analysis of the proposed methodology to verify the plausibility of our approach to brain tissue analysis.

4.1 Introduction

Digital Imaging is widely used in all scientific fields, such as biology, forensics, criminology, astronomy, etc. Image processing is used to improve graphic information to get clear, precise and detailed interpretation. It has attained valuable place in the field of medicine. Digital imaging in the medical field is used in diagnosis and therapeutics. The computerized images can be obtained from different sources and are processed in order to display a better quality image and to perceive different sections of the body, such as bones, tissues, organs, etc. in a much better way. Small deviation during the reading if misinterpreted can have fatal consequences. These image deviations can be caused by artifacts, illness or noise. Hence, the distinction between normal tissue and pathological tissue has a decisive diagnostic value. Segmentation plays an important role in solving this major problem.

The aim for the segmentation is to emphasize the properties of the image and use these prime attributes of the image in order to segregate it into sub parts in accordance to some principle. In other words, image segmentation is a process of delineation of an acquired image from different modalities (MRI, CT, USA, etc.) in well-defined areas which has certain clinical value, thereby facilitating image governed interventions, surgery, visualization and quantitative analysis. The peculiarity of any segmentation method depends on how well it uses the features derived from the original image to obtain the accurate and measurable result. The segmentation technique is evaluated and modified depending on its effectiveness, relevance and usefulness. The main difficulties of the segmentation process are: artifacts created by the machine during the generation of the image by the machine itself, noise and different tissues with analogous intensity [99]. An expert or a radiologist is

usually needed in most approaches for revising different control parameters in order to divide the image of the brain into two or more sub-sections, to identify the boundaries between normal growth and abnormal growth; or to differentiate between different parts of the brain, etc. Therefore, accurate automatic retrieval of object boundaries is of paramount importance in the clinical area.

Over the years, various algorithms are included in the literature (as presented in chapter 2), from which it can be inferred that recent developments in brain MR image segmentation are primarily focused on the Active contour methods (ACM) and its modified versions [119,123,124,127,131,132,133,135,136]. The performance of traditional approaches of ACMs is based on the proper initiation of the contours and the selection of the appropriate parameters to control curve dynamics, each time when the method is applied on every image. It is a laborious process, requiring a lot of time and knowledge. With this consideration, chapter 4 presents the modified region based active contour method (MRBAC) for segmentation of brain MR images which is a time efficient user adaptive process during curve initiation.

The organization of the remaining section of this chapter is as follows. The next part gives the brief description of various segmentation approaches along with the various schemes of ACMs which are employed in the proposed segmentation formulation. The proposed method is named as the MRBAC method which is discussed in detail and the process to implement it is also explained in this section. The MRBAC approach performance is also analyzed and explained using real MR images. Considerable effort has been made to evaluate and compare the effectiveness of segmentation with other existing methods in terms of the various performance indicators discussed in the following sections.

4.2 Categorization of Various Segmentation Schemes

Image segmentation is one of the crucial steps for qualitative and quantitative analysis of brain images, and proper segmentation provides useful information in the diagnostic process. The segmentation procedure splits the image into appropriate sub-regions and groups the neighborhood pixels according to a predefined criterion. The segmentation result corresponds to a group of disjoint regions, similar to regions within the input image. The segmentation methods are based on similarity or discontinuity criteria. Segmentation approaches which are constructed specifically to detect discontinuities are edge-based methods while those relying on similarity are: thresholding, region growing, region splitting and merging, and watershed [84, 111]. Some methods of image segmentation are briefly

described below.

4.2.1 Segmentation Based on Thresholding

These techniques are based on the principle of separating an object from an image background by selecting the suitable gray level range [220]. In this concept, the threshold value plays an important part. This value is usually chosen from the histogram of an image. A region consists of all pixels whose value (color, intensity, or any other property) is between two thresholds. A particular image area is divided by isolating, peaks, valleys or shapes in the corresponding intensity histogram [84]. The threshold methods do not need any prior information about the image. This method is practical and convenient for segmentation. However, precise segmentation cannot be accomplished due to the presence of different texture content in images or because of the presence of noise. In addition, the boundaries obtained by this method can give an unfair reading of the shape of the object.

Otsu method is one of the general thresholding approaches. In this algorithm, the pixel distribution pattern is analyzed in accordance with the concept that the pixels in each class/ group must be as similar as possible. This means that the intra-class variance of each class should be minimized, which ultimately maximizes the variance between the different classes. The intra-class variance defined by the Otsu method is a weighted sum of the variances of every cluster. In the literature, it is the most commonly used method that provides satisfactory and reliable results. However, the situation becomes problematic in multimodal histograms without clear or well defined boundaries [221, 223]. Moreover, it is usually difficult to determine functional and statistical attributes based solely on the value of the gray level.

4.2.2 Edge-Based Segmentation

Points, lines and edges contribute a huge amount of information for different areas of the image. [221]. However, edges and lines get generated when the intensity of the pixels changes dramatically. Basically, many edge detection methods are based on the gradient (local derivative) operation. The gradient vector of the image $I(x, y)$ is defined by computing the partial derivatives $\partial I/\partial x$, $\partial I/\partial y$ at every pixel point. There are varied range of edge detection methods each having different properties which can be applied for detection of the edges [224]. Numerous edge detector operators are present in the literature, which are usually pronounced after their inventors in which the most commonly used ones are: Prewitt operator [83,225], Sobel operator [83,226], Laplace operator [83,227] and Canny edge detector [83,228]. One of the major disadvantages of gradient operators is that they involve with derivative calculation which

consequently enhances the noise. Laplacian method on the other hand, gives the derivative of second-order and so it has even more sensitivity towards noise. So, the alternative to this issue is to make use of two operator's i.e. Laplacian of Gaussian operator which convolutes the image with Gaussian smoothing function. However, Sobel edge detector gives the benefit of both derivative effect along with the smoothing effect in the image while the Canny detector depends on the first derivatives extreme of Gaussian operator used on an image. Canny operator smoothens the image at first and then to eliminate noise from the image, it hunts for high gradient regions. Generally, detection of edges by evaluating gradients provides superior results in only those images which have sudden transition in intensity and are moderately lower in noise content. Due to its noise sensitivity, some smoothing operation is required as pre-processing step which consequently blurs the edge information in the image. As the process involves convoluting the image with the local filtering operation (kernel), thus it has low computational cost relatively when compared with the other segmentation procedures. The basic limitation of edge based segmentation methods is its dependency on the information confined on the local neighbourhood of image. Usually, the techniques which are centred on detecting the edges does not depend on model-based information rooted in the images [221]. In many instances, the edge based approaches totally neglect the organization in advance level which may be meaningfully existed in image [221].

The chief aim of edge detecting approaches is to connect appropriate edge so as to get borders of the object. As every edge located in an image may not perfectly linked or sometimes they may not be aptly visualized, henceforth this approach does not offer proper segmentation results. Likewise, it is typically difficult in identifying and classifying spurious edges [111]. Thus, detection of edges is regarded as pre-processing stage in these types of cases.

4.2.3 Region-Based Segmentation

Region based segmentation models are the counterpart approach to the edge-based segmentation approaches [103]. In this mode, segmentation is done by performing a pixel similarity search in sub-regions relying on certain properties like color, texture, or intensity. Segmentation according to this method is based on the principle that adjacent pixels of a given image area have similar characteristics. The objective is to search for regions that meet predefined homogeneity criteria. The segmentation approaches reliant on region properties are generally of two kinds, i. e. region growing approaches or the split and merge approaches [83].

The process of region growing [100-102] creates a group of pixels or subsets of

regions into larger regions that meet predefined criteria. In this type of technique, image attributes are used to map each pixel of the input image with groups of pixels called region. The region growth process starts at the pixel level, and at each step the same type of pixels merges one by one and continues until no more identical pixel elements are left to be added. Its results are better even when edges of the object are difficult to detect, as well as in the instances images corrupted with noise [111].

Region growing technique rely on a uniformity/homogeneity criteria. In other words, this method is manifested by selecting and grouping homogeneous sections of the image pertaining to some properties. Approaches based on region attributes use relatively larger neighbourhoods for decision-making purposes and all the time they deliver closed bound regions. The end user chooses a seed point, and then the region spreads out becoming larger and larger from the seed point until any growth stopping criteria is not encountered. These processes demand manual involvement for the selection of seed point and to formulate the stopping condition. Besides this major restraint of the region growing methods, there is another important problem resulting from the selection of initial seed point as on the basis of its properties the regions will grow. Oftentimes the choice of primary seed depends on the image type or peculiarity of the applications. Unlike the Laplacian or Gradient edge detection approaches, the borders of the regions by region growing are thin and completely connected. However, this method is also vulnerable to noise which is the reason of holes in the segmented area or amid two separate regions. Split and merge approaches [229] commence with entire image that is divided into small regions. At every step dissimilar regions comprising heterogeneity in them are sub-divided into smaller rectangular regions iteratively until every region becomes similar (homogeneous). Afterwards, the merging course starts where each similar neighbouring homogeneous region gets unified. Due to the successive partitioning of regions into quarters; the borders shaped by split process tend to look artificial and squarish in shape [111].

4.2.4 Watershed Transform-Based Segmentation

Watershed transforms [107], are one of the many techniques which are classified in region-based approaches for segmenting the region applying mathematical morphological tools. It is a one of the powerful methods in the field of image segmentation. It enjoys numerous advantages and hence watershed transform is extensively practiced in wide range of image processing fields for instance processing of synthetic images, medical Image segmentation, welding images, astronomy etc. Even with poor contrast in an image this [53]

transform entirely segregate into separate parts and thus avoids the need for any kind of contour joining. This transform embodies countless notions of the approaches like discontinuity detection and region processing. The segmentation outcomes are stable compared to other techniques, and the boundaries are perfectly linked continuous boundaries. This transform is built by the implementation of the flooding process on a grayscale image.

The watershed algorithm exploits region along with contour info for segmentation purposes, by considering it as 3D-topographic surface where the two are the spatial dimension while the third is a particular attribute like intensity, gradient. On the basis of this concept, the image is sub-divided into two distinct sets namely, the catchment basins and the watershed lines either by flooding the topographical surface from minima or by restricting the merging of waters coming from the different sources. For image segmentation, two procedures can be adopted for simulating this technique. First method is to uncover basins at first and afterwards watershed by taking a set complement. Second approach is to divide the entire image into basins and then locate watersheds by the use of boundary detection. Hence explicitly, the expression watershed transform stands for tagging the image in such a way that each point on a specific catchment basin has identical unique label. However, practically this transform is not directly employed in the original image instead, it is applied on the morphological gradient of the image [84,105].

The principal benefits of the watershed algorithm are that it can be straightaway implemented as well as it is less computationally complex. Moreover, it is adept of generating connected boundaries, even in the presence of low contrast regions or the weak edges in an image [84]. Though, the chief shortcoming of the watershed transform is the over-segmentation arising from the existence of noise irregularities in an image.

4.2.5 Hybrid Segmentation

Hybrid segmentation approaches, also at times referred as multivariate segmentation involve the fusion of two or more techniques. The properties of both region-based and edge-based segmentation techniques has the synergistic effect on the formulated hybrid model. They can be comparatively more accurate than the previously discussed segmentation approaches. The properties mined from both the techniques has combining strength of both of these two distinct methods, for example region joining decision is established on not only

on similarity of pixels but is also built upon previously extracted edges and the completion of these edges [97,230].

A large variety of hybrid segmentation methods are present in the literature delivering superior segmentation results [100,108,112, 231-234]. One such kind of hybrid method are the morphological watersheds segmentation schemes where the watershed is applied to the image gradient. This image gradient is observed as the topography having boundaries lying between the regions known as ridges.

4.3 Active Contour Based Segmentation

Active contours are denoted as the dynamic curves in two-dimension or the active surfaces in three-dimension which travel inside the image realm in order to capture the desired object's border lines. The contour movement is initiated by the user and is propelled by the combination of two forces viz. the internal force and the external force. These two forces achieve the minimal energy state whenever the curve reaches the desired boundaries of the objects. Snakes or active contours are widely popular in the management of several image comprehending problems for instance in medicine it is used for image segmentation and shape retrieval of abnormal tissues, object tracking, and edge detection. These methods are superior to the classical segmentation models as these models can attain sub-pixel accuracy in conjunction with giving the closed smooth curves or shapes. These prevailing deformable delineation model can be classified in two groups, namely, Parametric and Geometric (ACMs) active contour models. Parametric ACMs or parameterized curves [75,113] may take various explicit forms in a Lagrangian framework whereas the Geometric ACMs [74, 80] are implicitly represented in Eulerian framework in form of the level sets of a 2D-function.

4.3.1 Parametric Active Contour Models

The parametric ACMs were formerly proposed by Kass et al. [113] particularly to trace the objects boundaries. These dynamic shape models are extensively used in numerous viable image processing applications related to computer vision. Usually referred as snake models, the parametric contours evolve from initial position to the direction of the desired boundaries of the ROI and it stops when the model reaches its lowest energy state. These parameterized active curves can be written as $C(i)=[x(i), y(i)]$ where $0 \leq i \leq 1$ denotes contour arc-length. The parameters in this model help in regulating the dynamics of evolution of the curve, thereby focusing on minimizing the energy linked to the current contour. The energy of the contour

is the summation of the internal energy and the external energy in the spatial domain and it can be mathematically written as:

$$E = \int_0^1 \frac{1}{2} (\alpha |C'(i)|^2 + \beta |C''(i)|^2) ds + \int_0^1 E_{ext}(C(i)) di \quad (4.1)$$

Here, α , β denote weighting parameters accountable for controlling the tension, rigidity of the deformable curve, respectively. The 1st integral term represents the internal-energy function (smooth factor) determining the regularity of curve. The second integral term is the external-energy term E_{ext} , is represented in image domain (Ω), helps in lowering the value of desired features. The external energy acquired from features of image, is accountable for producing the contour with desired boundaries. The external energy is given as $E_{ext}(x, y) = -|\nabla(s(x, y))|^2$ or $E_{ext} = -|\nabla(G_\sigma(x, y) * s(x, y))|^2$, where ∇ indicates the gradient operator while $G_\sigma(x, y)$ is a 2D-Gaussian function with the standard deviation (σ). The evolving curve will become stable at minima, satisfying the mentioned Euler-Langrange equation:

$$\underbrace{\alpha C''(i) - \beta C''''(i)}_{F_{Int}} - \underbrace{\nabla E_{ext}}_{F_{ext}} = 0 \quad (4.2)$$

Here, F_{int} is the internal force while F_{ext} denote the external force, the contour C is the function of time. Equation (4.2) is solved as:

$$\frac{\partial C(i, t)}{\partial t} = \alpha C''(i, t) - \beta C''''(i, t) - \nabla E_{ext} \quad (4.3)$$

In which the initial contour is given by $C(i, 0) = C_0(i)$. A mathematical solution of equation (4.3) on can also be realized by applying the finite difference approach on the discrete grid. In spite of its popularity the traditional parameterized snake models consist of two main weaknesses which are trivial capture range and difficulties rising from topological deviations like splitting and merging of constantly evolving curve. Numerous approaches have been introduced to resolve the capture-range issue, namely: distance potential forces [236], pressure-forces [237], multiresolution approaches [238], gradient-vector-flow (GVF) [75,239] etc.

4.3.2 Geometric Active Contour Models

Caselles et al., Malladi et al. [74,80] introduced Geometric ACMs in an attempt to end the tyranny of parametric models. These models are also referred to as Geodesic Active Contours (GAC) [74] or conformal active contours [235] from time to time. These approaches are based on the level set framework and the curve evolution theory [121,122]. The main objective lies in representing the propagating contours in form of zero level-set function (LSF), and then evolving the LSF according to the partial-differential equation. Osher and Sethian [114] presented the numerical framework of level-set principle for the implementation of the active contours. In the mathematical level-set formulation of ACMs, the contour is defined by $C = \{(x, y) | \phi(x, y) = 0\}$, and contour propagation is represented by the zero level set function $\phi(t, x, y)$ at time 't'.

The evolution of LSF $\phi(x, y)$ is presented in Figure 4.1 (a) and the propagating corresponding curve is given in Figure 4.1 (b). When the LSF $\phi(x, y)$ starts developing from its initial state, the corresponding contour C begins to swell towards outside. Concurring to this definition, the contour propagation is equivalent to evolution of LSF i.e. $\partial C / \partial t = (\partial \phi(x, y)) / \partial t$. The reason for using level zero is that the contour C can be defined as a divider in-between the positive and negative area, so by just checking the sign of $\phi(x, y)$, contours location can be figured out.

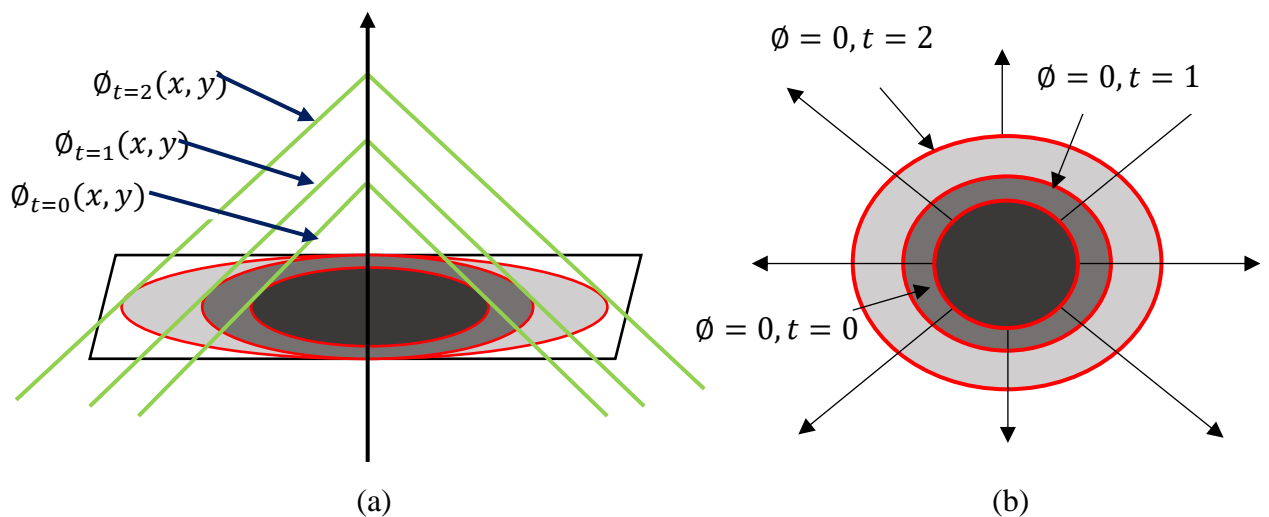


Figure 4.1: Level set evolution and the corresponding contour propagation: (a) Topological view of level set $\phi(x, y)$ evolution, (b) The changes on the zero-level set $C: \phi(x, y) = 0$ [114]

The following partial differential equation symbolizes the contour C evolution in the normal direction with speed F , governing the movement of the active curves.

$$\frac{\partial \phi}{\partial t} = F|\nabla \phi|, \phi_0(x, y) = \phi(0, x, y) \quad (4.4)$$

where $|\nabla \phi|$ and ϕ_0 denotes the normal direction and the initial contour respectively. Geometric ACMs have several advantages than compared with the conventional parameterized ACMs. For example, the level-set method behaves in a variable fashion in accordance to the motion of the contour by evolving LSF rather than straightaway affecting the curve [240]. Additionally, geometric ACMs can efficiently cope up with the topological variations.

The geometric models can be categorized into two groups namely: (a) Edge Based Active Contour Model (EBACM), (b) Region-Based Active Contour Model (RBACM). The EBACM approach follows the edge-based segmentation methodology by utilizing various edge detectors. They generally rely on gradient of the image to drive the curve towards the suitable boundaries. The RBACM approach on the other hand is capable of detecting the ROI by using region descriptors to manage the evolution of curve. Both of these approaches i.e. EBACM, RBACM are illustrated in the following sections and they are used for the comparison with the proposed segmentation approach.

4.4 Edge Based Active Contour Models using DRLSE Approach

EBACM comes under the category of edge-based segmentation methods. They are generally comprised of two terms viz., the regularity term and the edge detection term, that are utilized for estimating the contour shape and to drive the curve towards the edges, respectively. Formerly, Osher and Sethian [114] addressed the movement of active contours which was governed by the speed function F denoted as,

$$F = \text{div} \left(\frac{\nabla \phi}{|\nabla \phi|} \right) \quad (4.5)$$

Thus, the equation (4.4) is represented as,

$$\frac{\partial \phi}{\partial t} = |\nabla \phi| \left(\text{div} \frac{\nabla \phi}{|\nabla \phi|} \right) \quad (4.6)$$

Caselles et al. [241] introduced another prevalent EBACM based on mean curvature motion as:

$$\frac{\partial \phi}{\partial t} = g|\nabla \phi| \left(\operatorname{div} \left(\frac{\nabla \phi}{|\nabla \phi|} \right) + \alpha \right) \quad (4.7)$$

In equation (4.7), α refers to the inflation force which push the contour towards the object once the curvature became negative or null. $g = 1/[1 + |G_\sigma(x, y) * I(x, y)|^2]$ is the edge-function stops the level-set evolution near to the desired object boundaries, whenever the g vanishes. The G_σ is the Gaussian smoothening function having standard deviation (σ) while $G_\sigma * I$ is the smoothened image form. Later on, Caselles et al. [74] proposed a new EBACM method which begins by minimizing the energy functional defined by parameterized curves, where the contour evolution equation is derived on the Lagrangian framework. By embedding the contour into the LSF, the Lagrangian formulation can be reformulated in terms of the LSF(ϕ) in the given Eulerian formulation.

$$\frac{\partial \phi}{\partial t} = |\nabla \phi| \left(\operatorname{div} \left(g \frac{\nabla \phi}{|\nabla \phi|} \right) + \alpha g \right) \quad (4.8)$$

The formulation is known as the GAC model with the extra stopping term αg . This term is responsible to converge the contour to the object boundary more accurately and perform better even in the presence of weak edges.

The conventional active contour approaches with the LSF (ϕ) are shocky at times or may have very flat/sharp shapes at the moment of curve evolution resulting in additional inaccuracy during the computation. To resolve this issue, the general numerical scheme is utilized in which LSF is initialized as a signed distance function ahead of the evolution process and then the function ϕ is re-initialize as a signed distance function consistently during the evolution [120].

$$\frac{\partial \phi}{\partial t} = \operatorname{sign}(\phi_0)(1 - |\nabla \phi|) \quad (4.9)$$

In equation (4.9), ϕ_0 is the function to be reinitialized. If ϕ_0 is not smooth or is steeper on one side of the interface than the others, then the zero level-set of the resulting function ϕ moves inappropriately from that of the original function. Practically, the LSF evolution can be greatly deviated from the estimated location in just few iteration steps, mainly whenever the time-step utilized in discrete evolution equation is not small enough or whenever ϕ_0 is steeper, i.e. it is not very smooth. Thus, the process of re-initialization became crucial key to control the stability of curve evolution procedure and promise the improved segmentation results. Various researchers had re-initialized the regularity of LSF

for making LSF stable in several ways [118, 120, 121, 122,]. As the process of reinitialization of initial level set may be quite difficult at times so, Li et al. [119] introduced different variational formulation of the GAC model having the penalty-term that drives the LSF close to signed distance function. In a way, this process completely eliminates the periodic reinitialization procedure during the contour propagation. Though, there are some undesirable effects on level-set functional owing to the penalty term. Moreover, Li et al. [123] further improvised their previous approaches by including new distance-regularizing term and called it a distance-regularized level-set evolution (DRLSE). It consists of two well potential function as well as the external energy term which drives the movement of the contour towards the expected position. The variational-formulation can be written as:

$$E_{total}(\phi) = \mu R(\phi) + E_{ext}(\phi) \quad (4.10)$$

In equation (4.10), $E_{total}(\phi)$ is the overall energy including the regularization-term $R(\phi)$ while $E_{ext}(\phi)$ is the external energy term. The $R(\phi)$ term inherently forces ϕ to approach the signed-distance function at the time of evolution of the LSF and the parameter μ is weighting-coefficient ($\mu > 0$). $E_{ext}(\phi)$ refers to the external energy that forces the zero-LSF to the expected position. The external energy for the function $\phi(x, y)$ is given:

$$E_{ext}(\phi) = \lambda L(\phi) + \alpha A(\phi) \quad (4.11)$$

In equation (4.11), the first term and the second term are called the curves length-term and the artificial balloon-force- term respectively corresponding to the gradient flows of the energy function. The first term drives zero level-set contour toward the defined boundary of an object while second term is accountable to improve the contours moving speed. As the curve propagate, the parameter $\lambda > 0$ regulates the smoothness of the contour and is known as the weighting coefficient of the contour length. The parameter α is another weighing coefficient which may take any sign (plus or minus) depending on its position relative to the initial contour. The length term and balloon force energy functional terms are described as:

$$\left. \begin{aligned} L(\phi) &\triangleq \int_{\Omega} g \delta_{\varepsilon}(\phi) |\nabla \phi| dx \\ A(\phi) &\triangleq \int_{\Omega} g H_{\varepsilon}(-\phi) dx \end{aligned} \right\} \quad (4.12)$$

In the above equation g , $H_{\varepsilon}(x)$, $\delta_{\varepsilon}(x)$ are the edge-indicator functions, Heaviside-function and Dirac-delta function respectively, all of which are defined as:

$$g \triangleq \frac{1}{1+|\nabla G_{\sigma} * I|^2} \quad (4.13)$$

$$\delta_{\varepsilon}(x) = \begin{cases} 0, & |x| > \varepsilon \\ \frac{1}{2\varepsilon} \left[1 + \cos\left(\frac{\pi x}{\varepsilon}\right) \right], & |x| \leq \varepsilon \end{cases} \quad (4.14)$$

$$H_{\varepsilon}(x) = \begin{cases} 0, & x < -\varepsilon \\ 1, & x > \varepsilon \\ \frac{1}{2} \left[1 + \frac{x}{\varepsilon} + \frac{1}{\pi} \sin\left(\frac{\pi x}{\varepsilon}\right) \right], & |x| \leq \varepsilon \end{cases} \quad (4.15)$$

In equation (4.13), " I " represents the original image while " g " is its smoothed form obtained by convoluting image with Gaussian kernel G_{σ} having (σ) standard-deviation. To regularize the Dirac-delta function, the parameter " ε " is used which is constant [123]. The regularization-term $R(\phi)$ for levelset model is defined as:

$$R(\phi) \triangleq \int_{\Omega} p(|\nabla \phi|) dx \quad (4.16)$$

Here $p(|\nabla \phi|)$ refers to the potential-function of $R(\phi)$. A double well-potential function can be written as:

$$p(s) = \begin{cases} \frac{1}{2}(s-1)^2, & s \geq 1 \\ \frac{1}{4\pi^2} [1 - \cos(2\pi s)], & s \leq 1 \end{cases} \quad (4.17)$$

Taking first derivative of equation (4.17)

$$p'(s) = \begin{cases} s-1, & s \geq 1 \\ \frac{\sin(2\pi s)}{2\pi}, & s \leq 1 \end{cases} \quad (4.18)$$

Therefore, the total energy functional is approximated as:

$$E_{total}(\phi) = \mu \int_{\Omega} p(|\nabla \phi|) dx + \lambda \int_{\Omega} g \delta_{\varepsilon}(\phi) |\nabla \phi| dx + \alpha \int_{\Omega} g H_{\varepsilon}(-\phi) dx \quad (4.19)$$

Above equation is minimized by solving the gradient flow and it is given as:

$$\frac{\partial \phi}{\partial t} = \mu \operatorname{div} \left[\left(\frac{p'(|\nabla \phi|)}{|\nabla \phi|} \right) \nabla \phi \right] + \lambda \delta_{\varepsilon}(\phi) \operatorname{div} \left[g \frac{\nabla \phi}{|\nabla \phi|} \right] + \alpha g \delta_{\varepsilon}(\phi) \quad (4.20)$$

Equation (4.20) denotes the EBACM in a DRLSE formulation where the first term is known as distance-regularized energy term while the second and the third term represents the gradient flow of different energy function as described in equation (4.12). The $\phi_0(x, y)$ is initialized as:

$$\phi_0(x, y) = \begin{cases} -c_0, & (x, y) \in \Omega_0 \\ c_0, & \text{Otherwise} \end{cases} \quad (4.21)$$

Where, $c_0 > 0$ is a constant and Ω_0 is the ROI in the given image domain Ω . The equation (4.20) is discretized which can be stated in the given iterative arrangement.

$$\phi_{t+1}(x, y) = \phi_t(x, y) + \tau \frac{\partial \phi_t(x, y)}{\partial t} \quad (4.22)$$

Where, τ is known as the time step of the level-set evolution. For maintaining the stability during level-set evaluation, the time step factor τ and the penalty term μ must satisfy the condition ($\tau\mu < 1/4$).

4.5 Region Based Active Contour Models

Region based ACMs identify every region using some region descriptor like intensity, color, texture, motion to guide during the curve evolution than compared to its counterpart edge-based ACMs which use image gradients for curve propagation. Region based ACMs are less responsive to noise and weak edges as well as to the initial contour locations.

Mumford and Shah [125] addressed segregation of image as a variational problem to find out the optimum piecewise smooth (PS) approximation $F(x, y)$ of the original image $I(x, y)$ and a set of contours C in such a way that the approximation $F(x, y)$ moves smoothly within the connected components of the subsets excluding boundaries. The variational segmentation problem was solved by minimizing the global energy function as given below.

$$E_{MS}(F, C) = \int_{\Omega} |I(x, y) - F(x, y)|^2 dx dy + \int_{\Omega/C} |\nabla F(x, y)|^2 dx dy + v|C| \quad (4.23)$$

Where, $|C|$ is the contour length. Usually, it is rather hard to minimize the equation (4.23) due to unknown dimensions of C and F . This type of segmentation approach depends on the homogeneity of the image to be segmented. This presumption is often breached in medical images because of the presence of intensity inhomogeneities, motion or acquisition related artifacts and noise. Built on the foundation of Mumford and Shah model, Chan and Vese [124, 128] introduced another ACM and named it as CV model where the function $F(x, y)$ mentioned in equation (4.23) is a piecewise constant function. They effectively untangled the minimization problem by availing LSF that utilizes global image statistics in the interior and exterior of the evolving curve instead of gradients on the boundaries. They proposed the following energy function as given below.

$$E_{CV} = \lambda_1 \int_{outside(C)} |I(x, y) - C_1|^2 dx dy + \lambda_2 \int_{inside(C)} |I(x, y) - C_2|^2 dx dy + v \cdot \text{Area}(\text{inside}(C)) + \mu \cdot \text{Length}(C) \quad (4.24)$$

Here $\mu \geq 0, v \geq 0, \lambda_1 \lambda_2 > 0$ are the fixed parameters.

The 1st two terms of equation (4.24) are known as global fitting energy terms.

$$F_1(C) + F_2(C) = \int_{outside(C)} |I(x, y) - C_1|^2 dx dy + \int_{inside(C)} |I(x, y) - C_2|^2 dx dy \quad (4.25)$$

The terms $outside(C)$ and $inside(C)$ denotes respectively the region lying exterior and interior to the changing curve boundary C . The optimal constants C_1 and C_2 are the averages of intensities of the whole region outside (C) and $inside(C)$ respectively and these constants are helpful in minimizing the above global fitting energy. From Figure 4.2, it can be easily deduced that if the contour C is outside the boundary of the object then $F_1(C) > 0$ and $F_2(C) \approx 0$. And if the contour is within the object then $F_1(C) \approx 0$ and $F_2(C) > 0$ while if the condition is that the contour is C is inside as well as outside the object, then $F_1(C) > 0$ and $F_2(C) > 0$. Thus, the fitting energy term can only be minimized if the contour C is on the periphery of the object, that is $C = C_0$.

$F_1(C) > 0$ and $F_2(C) \approx 0$ $F_1(C) \approx 0$ and $F_2(C) > 0$ $F_1(C) > 0$ and $F_2(C) > 0$ $F_1(C) \approx 0$ and $F_2(C) \approx 0$

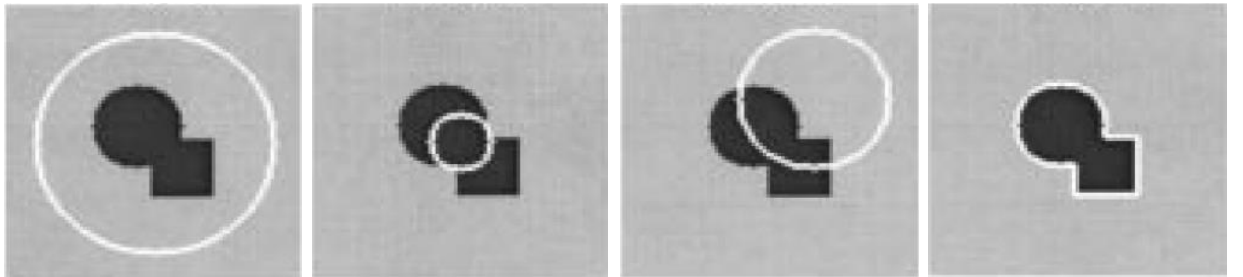


Figure 4.2: Different possible cases of contour position [124]

The energy function in equation (4.24) can be expressed in the level set formulation and then by solving the level set equation, the energy minimization problem can be dealt. So, following is the framework in the level set formulation.

$$\frac{\partial \phi}{\partial t} = \delta_\epsilon(\phi) \left[\mu \text{div} \left(\frac{\nabla \phi}{|\nabla \phi|} \right) - v - \lambda_1 (I(x, y) - C_1)^2 - \lambda_2 (I(x, y) - C_2)^2 \right] \quad (4.26)$$

where constants C_1 and C_2 are the averages of the intensities in the complete region outside (C) and inside(C), respectively. These are represented as a function of ϕ as defined below.

$$C_1(\phi) = \frac{\int_{\Omega} I(x,y)H(\phi(x,y))dxdy}{\int_{\Omega} H(\phi(x,y))dxdy} \quad (4.27)$$

$$C_2(\phi) = \frac{\int_{\Omega} I(x,y)(1-H(\phi(x,y)))dxdy}{\int_{\Omega} (1-H(\phi(x,y)))dxdy} \quad (4.28)$$

The CV model mostly works better for those images where the intensities in each disjoint region either inside(C) or outside (C) are consistently constant. However, it leads to poor segmentation in the image having intensity inhomogeneities. The performance of segmentation of CV model is affected by the placement of initial contour. Various results may be acquired on the same image by selecting distinct initial contour. Hence, proper initialization of the contour in CV model remains challenging problem to provide accurate segmentation results.

A concurrent parallel effort to the work of Chan-Vese, Tsai et al. [242] suggested the reformulation of Mumford Shah model from the curve propagation aspect by the use of gradient flow formulation and the implementation of level set framework. In order to overcome the limitations of the CV model, Li et al. [131] proposed a RBACM model adopting different variational LSF, which operate on RSF energy and level set regularization term. The RSF energy function can be interpreted in the terms of the two-fitting function which are basically the averages of the local image intensities on both side of the contour. Final curve evolution leads to the minimization of associated energy function and for this the intensity information in local regions at a certain scale is used to compute two fitting function, thereby guiding the contour movement towards the estimated object boundaries. Because of the presence of the level set regularization term in this formulation, the regularity of the LSF is maintained to guarantee accurate curve evolution as well as it also avoids re-initialization procedure [131]. The overall energy function can be written as

$$E_{Total}(\phi) = E_{RSF}(\phi) + E_R(\phi) \quad (4.29)$$

Where E_{Total} represent the total energy, E_{RSF} is the RSF energy given as:

$$E_{RSF}(C, F_1, F_2) = \sum_{i=1}^2 \lambda_i \int_{\Omega_i} K(x - y) |I(y) - F_i(x)|^2 dy \quad (4.30)$$

In the above equation (4.30) λ_1, λ_2 are two positive constants ; $F_1(x), F_2(x)$ are two separate fitting functions which approximate the average image intensities in $x \in \Omega$ and $(K(a) = (1/\sqrt{2\pi\sigma}). \exp(-|a|^2/(2\sigma^2)))$ is the Gaussian kernel function with standard deviation σ . Also, $E_R(\phi)$ in equation (4.29) is the composition of both level set regularization term $P(\phi)$ and contour length $L(\phi)$. The term $E_R(\phi)$ is given as:

$$E_R(\phi) = \mu P(\phi) + v L(\phi) \quad (4.31)$$

Where $P(\phi) = \frac{1}{2} \int (|\nabla\phi - 1|)^2 dx$ and $L(\phi) = \int \delta_\epsilon(\phi) |\nabla\phi| dx$, where δ_ϵ represents the Dirac delta function with a constant parameter ϵ which is accountable to regularize the Dirac delta function. Delta function is estimated as:

$$\delta_\epsilon(\phi) = \frac{1}{\pi} \left(\frac{\epsilon}{\epsilon^2 + \phi^2} \right) \quad (4.32)$$

Now the equation (4.29) can be written as:

$$E_{Total}(\phi, F_1, F_2) = \int_{\Omega} E_{RSF}(\phi, F_1, F_2) + \mu \frac{1}{2} \int_{\Omega} (|\nabla\phi - 1|)^2 dx + v \int_{\Omega} \delta_\epsilon(\phi) |\nabla\phi| dx \quad (4.33)$$

The equation (4.33) minimized by solving the gradient flow is given as [131]:

$$\frac{\partial\phi}{\partial t} = -\delta_\epsilon(\phi)(\lambda_1 e_1 - \lambda_2 e_2) + \mu \left[\nabla^2\phi - \text{div} \left(\frac{\nabla\phi}{|\nabla\phi|} \right) \right] + v \delta_\epsilon(\phi) \text{div} \left(\frac{\nabla\phi}{|\nabla\phi|} \right) \quad (4.34)$$

where

$$\begin{cases} e_1(x) = \int_{\Omega_1} K(x-y) |I(y) - F_1|^2 dy \\ e_2(x) = \int_{\Omega_2} K(x-y) |I(y) - F_2|^2 dy \end{cases} \quad (4.35)$$

In the above expression of equation (4.34) comprise of three separate terms in which the 1st term $-\delta_\epsilon(\phi)(\lambda_1 e_1 - \lambda_2 e_2)$ represents the data fitting term which is used to develop the contour towards the desired object boundaries. The 2nd term $\mu \left[\nabla^2\phi - \text{div} \left(\frac{\nabla\phi}{|\nabla\phi|} \right) \right]$ refers to the contour regularity term accountable to keep up the regularity of the LSF with its weighting coefficient (μ) and it is also known as regularization coefficient. The 3rd term $v \delta_\epsilon(\phi) \text{div} \left(\frac{\nabla\phi}{|\nabla\phi|} \right)$ coined as the contour length term, is responsible of providing the smoothness on the zero LSF. This term is controlled by its controlling parameter (v). In equation (4.35) F_1 and F_2 refer to the weighted averages of the intensities within the

neighboring region of (x) , whose size is proportional to the scale parameter (σ) and are given as:

$$F_1 = \frac{K_\sigma(x) \cdot [M_1^\epsilon(\phi(x))I(x)]}{K_\sigma(x) \cdot [M_1^\epsilon(\phi(x))]} \quad (4.36)$$

$$F_2 = \frac{K_\sigma(x) \cdot [(M_2^\epsilon(\phi(x)))I(x)]}{K_\sigma(x) \cdot [M_2^\epsilon(\phi(x))]} \quad (4.37)$$

Where, K_σ refer to the Gaussian kernel function and is defined similarly as used in equation (4.30). The Heaviside function “H” in the above formulation is approximated by the smooth function H_ϵ is given by

$$H_\epsilon(x) = \frac{1}{2} \left[1 + \frac{2}{\pi} \arctan \left(\frac{x}{\epsilon} \right) \right] \quad (4.38)$$

And $M_1^\epsilon(\phi) = H_\epsilon(\phi)$, $M_2^\epsilon(\phi) = 1 - H_\epsilon(\phi)$. In this formulation, the level set function $\phi_0(x, y)$ is initialized as given below:

$$\phi_0(x, y) = \begin{cases} -c_0, & (x, y) \in \Omega_0 - \partial\Omega_0 \\ 0, & (x, y) \in \partial\Omega_0 \\ c_0, & (x, y) \in \Omega - \Omega_0 \end{cases} \quad (4.39)$$

where $c_0 > 2\epsilon$ is a constant, Ω_0 is a region of interest (ROI) in the given image domain Ω and $\partial\Omega_0$ is the boundary of Ω_0 . The discretization of equation (4.34) is written as:

$$\phi_{t+1}(x, y) = \phi_t(x, y) + \tau \frac{\partial \phi_t(x, y)}{\partial t} \quad (4.40)$$

where τ refers to the time step of level set evolution.

4.6 Proposed Modified Region Based Active Contour (MRBAC) Method

Generally, region-based ACM evolution relies on global information due to which in presence of intensity inhomogeneity these model fails. In medical image processing, presence of intensity inhomogeneity is often the case either due to motion or acquisition artifacts or due to type of tissue itself. Although few methods are available in literature to incorporate local information empirically in the image, but their demerit is the involvement of complicated procedures resulting to highly time intensive procedures. Appropriate contour initialization of ACMs directly affects its segmentation performance. The proposed modified region based active contour method (MRBAC) is a variant of LGDF model [243]. Classical LGDF model findings were evaluated on few images and are disputable in certain

cases of MRI lesions. It does not fit well when presented with the image where the background and foreground have only a difference in texture or when the object boundaries are very weak. Also, defining the initial contour location was done empirically which is time consuming process.

The proposed method conserves the merits of traditional technique along with adopting the new feature for contour initialization. The radiologists at the MRI center manually trace the contour which seeks high amount of attention, patience and time.

The proposed method speeds up the whole process as it requires the involvement of technicians who can quickly rough mark the boundary. So instead of empirically feeding the ρ value defined in circular neighbourhood region θ_x , we propose the initial level set function in form of quickly drawn outline around the lesion.

The LGDF energy formulation of region θ_x along all the disjoint regions Ω_i is given as [243]:

$$E_x^{LGDF} = \sum_{i=1}^N \int_{\Omega_i \cap \theta_x} - \log p_{i,x}(I(y)) dy \quad (4.41)$$

Where $p_{i,x}(I(y))$ is the probability density in region $\Omega_i \cap \theta_x$ depicting the gray value distribution in that region which is given as:

$$p_{i,x}(I(y)) = \frac{1}{\sqrt{2\pi}\sigma_i(x)} \exp\left(-\frac{(u_i(x)-I(y))^2}{2\sigma(x)^2}\right) \quad (4.42)$$

Adding weighting function in equation (4.41) results in

$$E_x^{LGDF} = \sum_{i=1}^N \int_{\Omega_i \cap \theta_x} - \omega(x-y) \log p_{i,x}(I(y)) dy \quad (4.43)$$

Where, $\omega(x-y) = 0$ for all $|x-y| > \rho$, $\int_{\theta_x} \omega(x-y) dy = 1$ is a non-negative weight function. Here, the weight function ω is a truncated Gaussian kernel with a localization property that with the increase of $|r|$ value, $\omega(r)$ decreases and approaches to zero. It is defined as:

$$\omega(r) = \begin{cases} \frac{1}{a} \exp\left(-\frac{|d|^2}{2\sigma^2}\right) & \text{if } |r| \leq \rho \\ 0 & \text{if } |r| \geq \rho \end{cases}$$

Here a is constant such that $\int \omega(r) = 1$. The above E_x^{LGDF} is given as

$$E_x^{LGDF} = \sum_{i=1}^N \int_{\Omega_i} - \omega(x-y) \log p_{i,x}(I(y)) dy \quad (4.44)$$

To minimize above energy functional for all centre point x in image domain Ω double integral of equation (4.44) is taken as

$$E^{LFDF} = \int_{\Omega} E_x^{LGDF} dx = \int_{\Omega} \left(\sum_{i=1}^N \int_{\Omega_i} -\omega(x-y) \log p_{i,x}(I(y)) dy \right) dx \quad (4.45)$$

In the level set framework, the image is divided into two regions Ω_1 and Ω_2 as foreground and background suggesting the regions lying outside and inside the zero-level set, such that $\Omega_1 = \{\varphi > 0\}$ and $\Omega_2 = \{\varphi < 0\}$. Using Heaviside function H , the energy E_x^{LGDF} is given as:

$$E_x^{LGDF}(\varphi, u_1(x), u_2(x), \sigma_1(x)^2, \sigma_2(x)^2) = - \int \omega(x-y) \log p_{1,x}(I(y)) M_1(\varphi(y)) dy - \int \omega(x-y) \log p_{2,x}(I(y)) M_2(\varphi(y)) dy \quad (4.46)$$

Where, $M_1(\varphi(y)) = H(\varphi(y))$ and $M_2(\varphi(y)) = H(\varphi(y))$

$$E^{LGDF}(\varphi, u_1, u_2, \sigma_1^2, \sigma_2^2) = \int_{\Omega} E_x^{LGDF}(\varphi, u_1(x), u_2(x), \sigma_1(x)^2, \sigma_2(x)^2) \quad (4.47)$$

In order to regularize the level set by penalizing contour deviation by signed distance function

$$P(\varphi) = \int \frac{1}{2} (|\nabla \varphi(x)| - 1)^2 dx \quad (4.48)$$

In order to penalize the length for smooth contour evolution

$$L(\varphi) = \int |\nabla H(\varphi(x))| dx \quad (4.49)$$

Incorporating length and regularization term, the entire energy functional can be written as

$$F(\varphi, u_1, u_2, \sigma_1^2, \sigma_2^2) = E^{LFDF}(\varphi, u_1, u_2, \sigma_1^2, \sigma_2^2) + vL(\varphi) + \mu P(\varphi) \quad (4.50)$$

Where, $v, \mu > 0$ are the weighting constants. The Heaviside function H is given as

$$H_{\epsilon} = \frac{1}{2} \left[1 + \frac{2}{\pi} \arctan \left(\frac{x}{\epsilon} \right) \right] \quad (4.51)$$

The derivative of H_{ϵ} is the following smoothing function

$$\delta_{\epsilon}(x) = H_{\epsilon}^1(x) = \frac{1}{\pi} \frac{\epsilon}{\epsilon^2 + x^2} \quad (4.52)$$

Thus, energy functional is approximated as

$$F_\epsilon(\varphi, u_1, u_2, \sigma_1^2, \sigma_2^2) = E_\epsilon^{LGDF}(\varphi, u_1, u_2, \sigma_1^2, \sigma_2^2) + \nu L(\varphi) + \mu P(\varphi) \quad (4.53)$$

Above energy function is minimized by parameters u_i and σ_i^2 must satisfy Euler-Lagrange equations:

$$\int \omega(y-x) (u_i(x) - I(y)) M_{i,\epsilon}(\varphi(y)) dy = 0 \quad (4.54)$$

and

$$\int \omega(y-x) (\sigma_i(x^2) - (u_i(x) - I(y))^2) M_{i,\epsilon}(\varphi(y)) dy = 0 \quad (4.55)$$

where

$$M_{1,\epsilon}(\varphi(y)) = H_\epsilon(\varphi(y)) \text{ and } M_{2,\epsilon}(\varphi(y)) = 1 - H_\epsilon(\varphi(y))$$

From 4.54 and 4.55 we get

$$u_i(x) = \frac{\int \omega(y-x) I(y) M_{i,\epsilon}(\varphi(y)) dy}{\int \omega(y-x) M_{i,\epsilon}(\varphi(y)) dy} \quad (4.56)$$

And

$$\sigma_i(x^2) = \frac{\int \omega(y-x) (u_i(x) - I(y))^2 M_{i,\epsilon}(\varphi(y)) dy}{\int \omega(y-x) M_{i,\epsilon}(\varphi(y)) dy} \quad (4.57)$$

Minimization of energy functional F_ϵ with respect to φ in equ 4.53 is achieved by solving gradient decent flow equation

$$\frac{d\varphi}{dt} = -\delta_\epsilon(\varphi)(e_1 - e_2) + \nu \delta_\epsilon(\varphi) + \text{div} \left(\frac{\nabla \varphi}{|\nabla \varphi|} \right) + \mu \left(\nabla^2 \varphi - \text{div} \left(\frac{\nabla \varphi}{|\nabla \varphi|} \right) \right) \quad (4.58)$$

Where

$$e_1(x) = \int_\Omega \omega(y-x) \left[\log(\sigma_1(y)) + \frac{(u_1(y) - I(x))^2}{2\sigma_1(y)^2} \right] dy \quad (4.59)$$

$$e_2(x) = \int_\Omega \omega(y-x) \left[\log(\sigma_2(y)) + \frac{(u_2(y) - I(x))^2}{2\sigma_2(y)^2} \right] dy \quad (4.60)$$

This method of segmentation based on variational level set for active contour model where image intensities are represented by Gaussian distribution with distinct means and standard deviations. Local means and standard deviations of images are effectively utilized to segment the brain MR images having intensity inhomogeneities. Additionally, this model is

able to differentiate the homogeneous intensity areas having different local standard deviations. This model is tested for brain MR images having different types of abnormalities like Hemorrhage, Infarction and Tumor.

Implementation steps

For medical image (Brain MRI) segmentation and implementation of the above discussed aspects, the proposed (MRBAC) algorithm is given as:

Step 1: Start with given MR image

Step 2: Define the enclosed boundary as the region of interest and evaluate the initial level set function φ_0 . Define time step parameter $\tau = 0.1$, Gaussian kernel of size 5, $\lambda_1 = \lambda_2 = 1$.

Step 3: Compute local means $u_i(x)$ by equation (4.56)

Step 4: Compute local standard deviation by equation (4.57)

Step 5: If the change in evolving contour of the level set function between successive iteration is less than the termination criterion ($\varphi_i - \varphi_{i-1} < 0.3$) then stop.

Step 6: Return to step 3 until convergence criteria is met.

In this segmentation, Gaussian distributions with different means and variances are deployed to describe the local image intensities. Here we assign level set function by local Gaussian distribution fitting energy and variables by localized means and variances. Goal is to let the level set evolve thereby achieving energy minimization. Local means and local variance of intensity are updated iteratively thereby updating the level set function. This method address issues of intensity in-homogeneities and noise (like multiplicative noise) of varying strength by assigning means and variance of local intensity as spatially varying function. We have conducted this study on the three common diseases namely, Brain tumor, Hemorrhage and Infarct accentuating death incidences. It has been recognized and emphasized time and again that early and correct segmentation of ROI which is respondent to inter-observability of radiologist can reduce causality caused by these emergency conditions.

4.7 Assessment Criteria

The experiments are executed on homogeneous, heterogeneous and diffused lesions on MR images and are compared with the ground truth demarcated by radiologists. In order to analyze and evaluate the performance of the segmentation scheme quantitatively several validation parameters are used for example True Positive (TP) [222, 245], False Positive

(FP) [222, 245], Accuracy (ACC) [245], Jaccard Similarity Index (JSI) [222, 245], Dice Coefficient (DC) [245], and Hausdorff Distance (HD) [222, 244, 245].

4.7.1 True Positive (TP) Ratio

It represents those pixels which become visible in both binary mask of the segmented region computed by manual as well as in computerized segmentation method. The TP value is given as:

$$TP = \frac{|s_M \cap s_T|}{|s_M|} \quad (4.61)$$

where s_M indicates the manually segmented ground truth binary mask and s_T denotes the binary mask of the region segmented by the computerized method. The higher value of the TP ratio implies that overlapping area between the real and segmented region is large.

4.7.2 False Positive (FP) Ratio

It is a measure of those pixels which become visible in the segmented region generated by test method, while do not appear in the ground truth binary mask. Lower values of FP imply fewer incorrect regions covered by segmented region. The FP ratio is given as:

$$FP = \frac{|s_M \cup s_T - s_M|}{|s_M|} \quad (4.62)$$

4.7.3 Accuracy (ACC)

It measures the proportion of pixels contained within the correctly extracted region obtained by test method out of all the pixels of manually delineated region. The segmentation accuracy is given as:

$$ACC = \frac{TP+TN}{TP+FP+TN+FN} \quad (4.63)$$

Where TP, FP, TN, FN denotes the true positive, false positive, true negative, false negative values, respectively.

4.7.4 Jaccard Similarity Index (JSI)

It is used as a statistical measure of similarity between the regions delineated by manual and computerized method. It is represented as:

$$JSI = \frac{|S_M \cap S_T|}{|S_M \cup S_T|} \quad (4.64)$$

Higher value of JSI metric signifies that more segmented region matches with the manual segmentation or the ground truth.

4.7.5 Dice Coefficient (DC)

This statistical measure gives the similarity of the extracted regions in-between the test segmentation algorithms and manually delineated ground truth. The DC ratio is given as:

$$DC = 2 \times \frac{|S_M \cap S_T|}{|S_M + S_T|} \quad (4.65)$$

The values of dice coefficient should be close to unity which ensures the exact overlapping of the segmented and the manually delineated region.

4.7.6 Hausdroff Distance (HD)

This metric is used as a measure of structural difference between two objects. It is given as the maximum of the Euclidean distance between the least distant point pair in the structures. For the two contours P and Q, the HD index is estimated as follows:

$$HD(P, Q) = \max \left\{ \sup_{x \in P} \inf_{y \in Q} d(x, y), \sup_{y \in Q} \inf_{x \in P} d(x, y) \right\} \quad (4.66)$$

Where sup and inf refers to the supremum and infimum operators, respectively and $d(x, y)$ denotes the Euclidean distance between two points x and y. Therefore, the HD provides the upper limit of the object misalignment between the contour of the extracted and manual delineated boundaries. In other words, the smaller HD value indicates that distance between boundaries of segmented and manually marked ROI is very small which further shows better segmentation by the technique.

4.8 Experimentation

To examine the performance of the proposed MRBAC segmentation method, three experiments have been done. Proposed MRBAC segmentation technique is compared with Region Growing and DRLSE segmentation methods. Same images are taken to segment lesion with all three-segmentation technique so that performance comparison can be done effectively. Same performance measures are used to compare the proposed segmentation

methods with other two methods. MR images with three lesions namely tumor, infarct and hemorrhage are taken and the intensive segmentation on images are done to assess the validity of the proposed MRBAC method. Lesions have different shape, location and size in each experiment. Since other segmentation methods which are taken in experiment work well with homogeneous lesions hence for fair comparison with proposed MRBAC segmentation method, homogeneous lesions having full or peripheral enhancement are considered as a part of experiment along with heterogeneous lesions.

The segmentation and analysis of lesion on brain MRI is executed in Matlab R2014a. Experiments were conducted on the Intel(R) Core (TM) i3 - M370 CPU at 2.4 GHz, 6 GB RAM, Windows 10 Home.

Details of experiments are given below:

Experiment 1: Segmentation and evaluation of different shapes and types of tumors in axial, sagittal and coronal planes. Also, the effectiveness of proposed method on Brain Tumor MR Images is analyzed by comparing MRBAC method with other methods.

Experiment 2: Segmentation and evaluation of different shapes and types of infarcts in axial, sagittal and coronal planes. It also illustrates the effectiveness of proposed method on Brain Infarct MR Images by comparing it with other methods.

Experiment 3: Segmentation and evaluation of different shapes and types of Hemorrhage in axial, sagittal and coronal planes. The potential of MRBAC method on Brain Hemorrhage MR images is judged by analyzing it with other methods.

4.9 Results and Discussions

4.9.1 Experiment No. 1:

Analysis and evaluation of segmentation results for Brain Tumor images- In order to validate the experimental objective, several test brain tumor MR images are taken. MR data used for experimentation is collected from Doon MRI & Diagnostics, Dehradun (India). All images are resized to 256×256. Fifty-seven images of tumor patients are considered for this experiment out of which are twenty-six are T1-weighted image and thirty-one are T2-weighted images. These images are in three different planes, namely axial, coronal and sagittal.

The segmentation result of five different tumor MR images are presented in a qualitative manner in Figure 4.3. It displays the comparison of the segmentation results

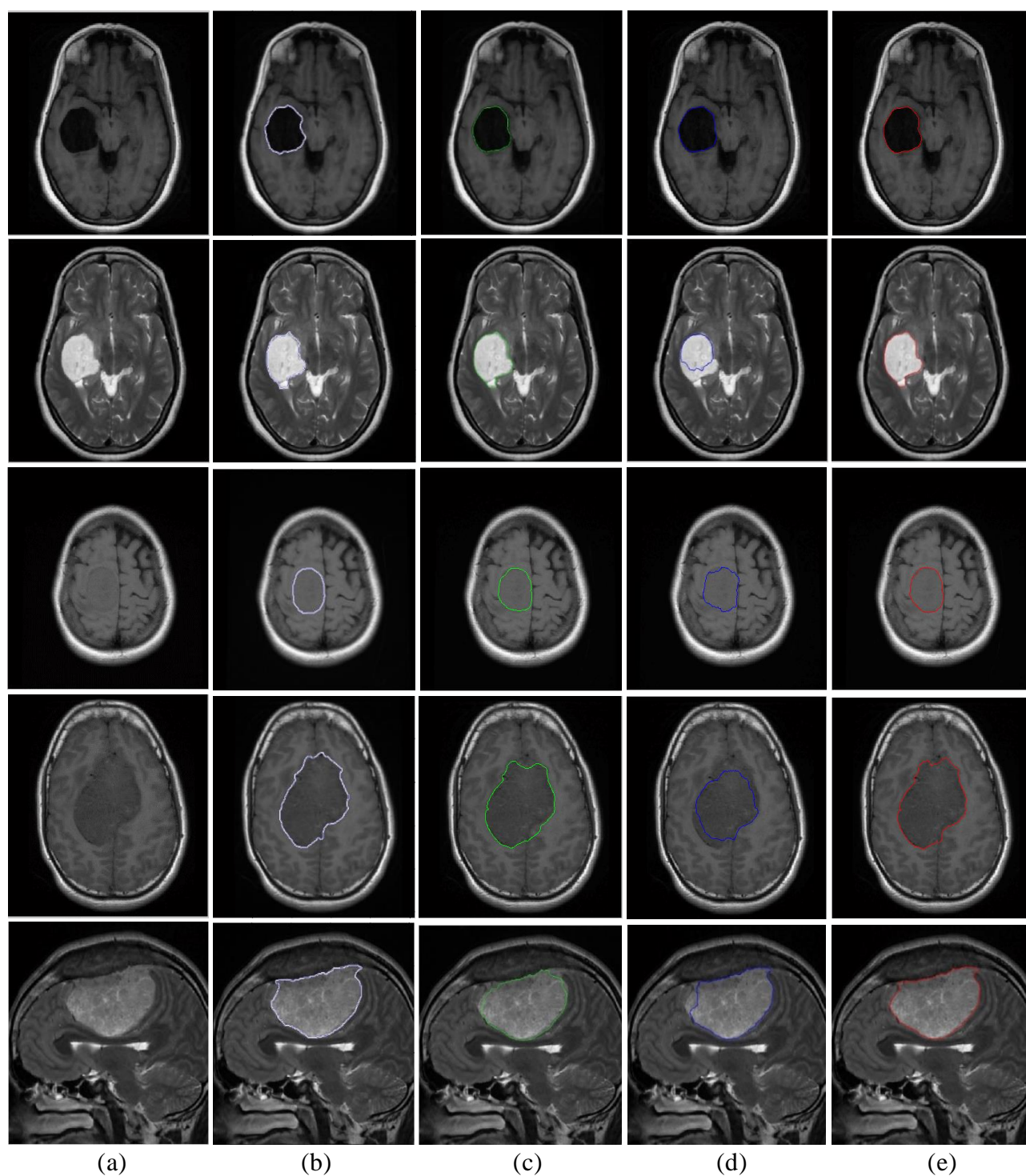


Figure 4.3: Comparative visual analysis of segmentation result of different tumor MR image obtained by (a) original image (b) ground truth marked by radiologist (c) segmented by Region Growing method (d) segmented by DRLSE method (e) segmented by proposed MRBAC method.

obtained from the aforementioned segmentation approaches with that of proposed method. Figure 4.3(a) is the original image while Figure 4.3(b) is ground truth marked by the radiologist. From Figure 4.3(e), it can be perceived that the ROI boundaries are accurately segmented by the proposed method. Figure 4.3(c), (d) presents the extracted region boundaries segmented by Region Growing method, DRLSE method, respectively. The third and fourth rows shows the tumor in presence of intensity inhomogeneities with quite weak boundaries. It can be clearly seen that proposed MRBAC method can successfully delineate hypointense, hyperintense, isointense tumors despite of the presence of very weak boundaries showing its superiority over other methods. The image shown in first row is an axial T1-weighted MR image of large epidermoid tumor. Second row image is an axial T2-weighted image MR image of the same subject. The axial T1-weighted image shown in third row refers to the right parietal parasagittal meningioma. The image shown in fourth row is an axial T1-weighted MR image of a large bilobed flax. Last row image is the T2-weighted image in sagittal view of the same patient.

Table 4.1: Performance measures obtained by different segmentation methods for MR images of tumor shown in Figure 4.3

Methods	Images	TP	FP	ACC	JSI	DC	HD
Region Growing	T 1	0.895	0.010	0.942	0.886	0.940	2.236
	T 2	0.920	0.061	0.931	0.867	0.929	3.000
	T 3	0.911	0.028	0.942	0.886	0.940	2.646
	T 4	0.910	0.054	0.926	0.864	0.927	5.000
	T 5	0.885	0.026	0.927	0.862	0.926	5.385
DRLSE	T 1	0.897	0.009	0.943	0.889	0.941	2.646
	T 2	0.605	0.005	0.797	0.602	0.751	3.606
	T 3	0.913	0.066	0.925	0.857	0.923	3.742
	T 4	0.685	0.015	0.828	0.674	0.806	4.243
	T 5	0.909	0.020	0.942	0.891	0.942	4.000
Proposed MRBAC	T 1	0.922	0.012	0.954	0.911	0.953	2.236
	T 2	0.880	0.043	0.919	0.844	0.915	3.000
	T 3	0.933	0.043	0.946	0.895	0.945	2.646
	T 4	0.941	0.037	0.950	0.908	0.952	4.359
	T 5	0.956	0.0232	0.965	0.934	0.966	4.000

Also, it is visible from the obtained result that the proposed method effectively extracts tumor boundaries in the MR image. The segmentation result obtained by MRBAC is almost similar to the manually marked regions as compared to Region Growing and DRLSE methods. In addition to the qualitative evaluations of the brain MR tumor images, different quantitative analysis has also been given in terms of the different performance metrics of assessment criteria that is mentioned in Table 4.1. The averaged quantitative results with standard deviations are listed in Table 4.2 which shows the accuracy of proposed segmentation method is 94.7% than compared to 93.3% and 88.7% for Region Growing and DRLSE methods respectively. This indicates the better performance of the proposed approach over other compared techniques. The other performance metrics such as JSI and DC found by the proposed approach, achieves higher values than other compared segmentation approaches. The higher values of both these parameters indicate that proposed approach segments more similar portions of tumor than other methods.

Table 4.2: Averaged performance measures obtained by different segmentation methods for all MR images of tumor

Methods	TP (AVG \pm STD)	FP (AVG \pm STD)	ACC (AVG \pm STD)	JSI (AVG \pm STD)	DC (AVG \pm STD)	HD (AVG \pm STD)
Region Growing	0.904 \pm 0.013	0.036 \pm 0.019	0.933 \pm 0.007	0.873 \pm 0.011	0.932 \pm 0.006	3.653 \pm 1.286
DRLSE	0.802 \pm 0.131	0.023 \pm 0.022	0.887 \pm 0.062	0.783 \pm 0.121	0.873 \pm 0.079	3.647 \pm 0.546
Proposed MRBAC	0.926 \pm 0.026	0.032 \pm 0.012	0.947 \pm 0.015	0.898 \pm 0.030	0.946 \pm 0.017	3.248 \pm 0.806

The averaged TP obtained by MRBAC approach is also high of 92.6%. This approach achieves higher TP, ACC, DC and JSI values and lower FP, HD values as clearly seen in Figure 4.4. This is demonstrated in the box plot of all the quantitative indices obtained by Region Growing method, DRLSE method and the proposed method for better representation of result. It can be observed from it that the median of TP, ACC, DC, JSI have highest value while FP, HD have lowest values in case of MRBAC method and the dispersion in the values is also not very large.

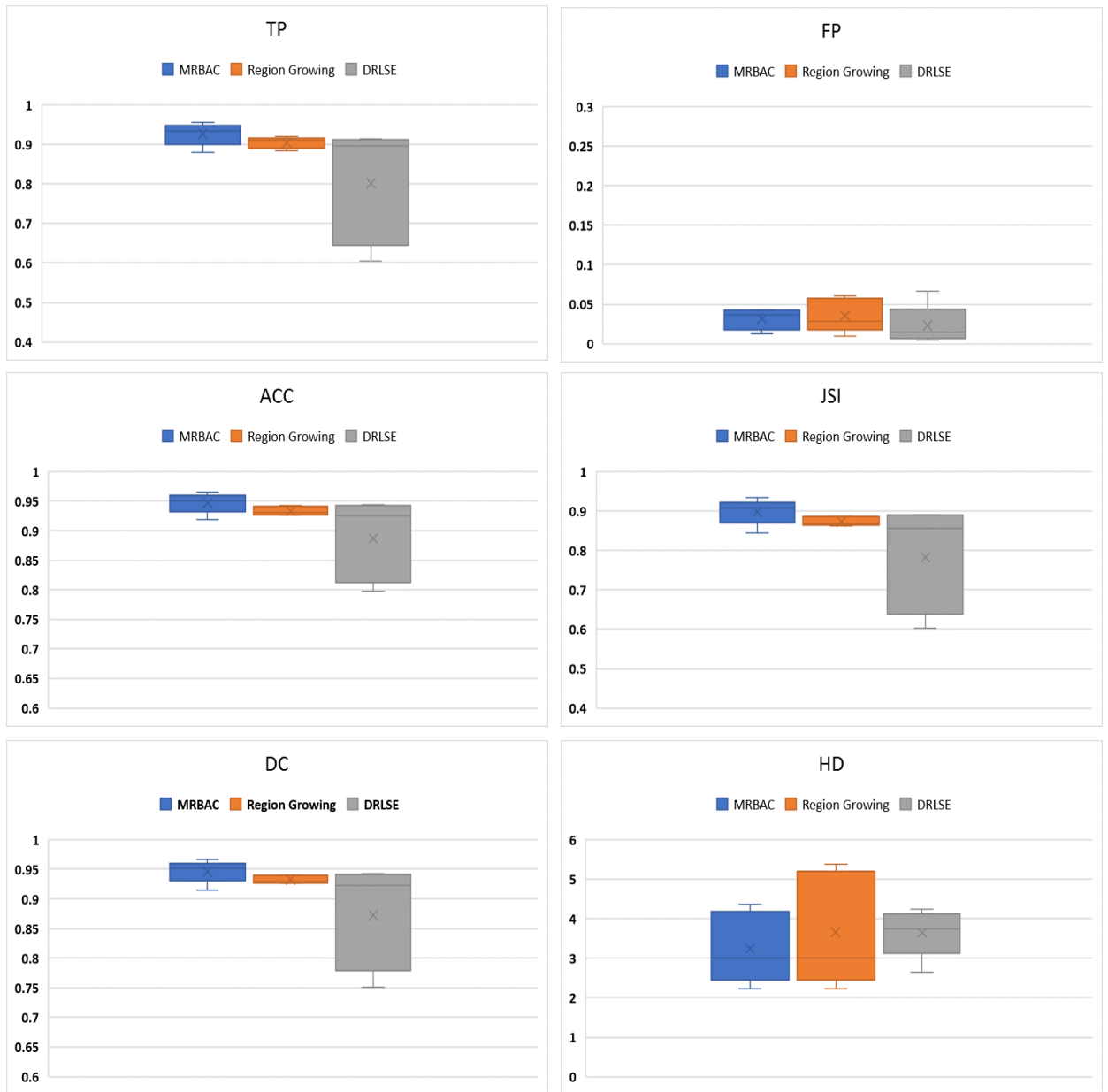


Figure 4.4: Box plot of True Positive (TP), False Positive (FP), Accuracy (ACC), Jaccard Similarity Index (JSI), Dice Coefficient (DC) and Hausdorff Distance (HD) measurements of all the Tumor MR images shown in Figure 4.3 by proposed MRBAC, Region Growing and DRLSE segmentation methods.

Furthermore, the running time for all the segmentation models is also been evaluated. The specifics of the computation time and the average number of iterations to extract the region of all the images are listed in Table 4.3. From the results, it can be seen that the

proposed MRBAC method takes less time and a smaller number of iterations in comparisons to others.

Table 4.3: Comparative performance of segmentation approach with averaged number of iteration and averaged computation time for all tumor images

Methods	Averaged resolution	Averaged Iterations	Averaged computation time (s)
Region Growing	256x256	190	16.75
DRLSE	256x256	210	18.46
Proposed MRBAC	256x256	160	14.47

4.9.2 Experiment No. 2:

Analysis and evaluation of segmentation results for Brain Infarct images - In order to validate the experimental objective, several brain infarct MR images are taken. MR data used for experimentation is collected from Doon MRI & Diagnostics, Dehradun. All images are resized to 256×256. Twenty-seven images in all the three different planes are taken for evaluating the performance of the proposed method for infarct patients. Out of twenty-seven, twelve T1-weighted image and fifteen T2-weighted images are selected.

The segmentation result of five different infarct MR images are presented in a qualitative manner in Figure 4.5. The image shown in first row is chronic infarct with residual encephalomalacia. Second row image is an axial T1-weighted image MR image of the ischemic infarct. The coronal T2-weighted image shown in third row is of the same subject. The image shown in fourth row is an axial T2-weighted MR image of acute ischemic infarct. Last row image is the T2-weighted MR image in coronal view of the large acute ischemic infarct. Figure 4.5 shows the comparison of segmentation results obtained by aforementioned segmentation methods with that of proposed method. Figure 4.5 (a) is the original image while Figure 4.5 (b) is ground truth marked by the radiologist. From Figure 4.5 (e) it can be seen that the proposed MRBAC technique precisely segments the infarct areas of the brain MRI. Figure 4.5 (c) and (d) presents the extracted region boundaries segmented by Region Growing and DRLSE method, respectively. From these results it can be observed that Region Growing and DRLSE methods fails to delineate the boundaries completely while proposed method is able to segment infarct images effectively even in the presence of heterogeneities and weak boundaries. Segmentation results obtained by MRBAC method is similar to the manually

marked regions as compared with other methods.

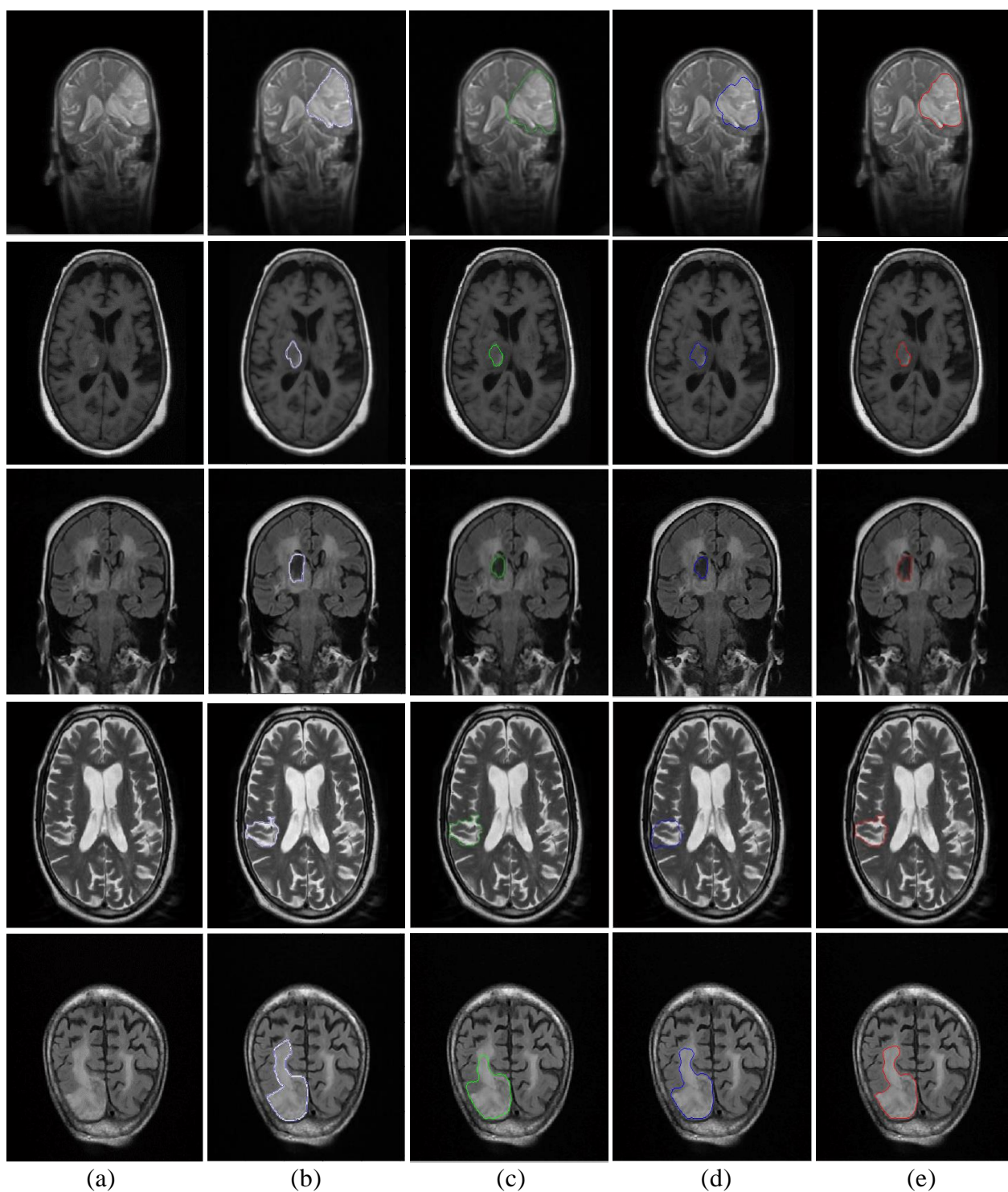


Figure 4.5: Comparative visual analysis of segmentation result of different Infarct MR Image obtained by (a) original image (b) ground truth marked by radiologist (c) segmented by Region Growing method (d) segmented by DRLSE method (e) segmented by proposed MRBAC method

Table 4.4: Performance measures obtained by different segmentation methods for MR images of infarct shown in Figure 4.5

Methods	Images	TP	FP	ACC	JSI	DC	HD
Region Growing	II1	0.982	0.255	0.876	0.783	0.878	4.000
	II2	0.658	0.016	0.822	0.648	0.786	2.000
	II3	0.650	0.038	0.809	0.626	0.770	2.828
	II4	0.970	0.301	0.856	0.746	0.855	4.123
	II5	0.842	0.167	0.847	0.722	0.838	3.742
DRLSE	II1	0.824	0.082	0.874	0.762	0.865	3.000
	II2	0.805	0.040	0.884	0.774	0.873	2.000
	II3	0.683	0.038	0.825	0.658	0.794	2.828
	II4	0.905	0.400	0.792	0.646	0.785	3.742
	II5	0.902	0.119	0.895	0.806	0.892	2.646
Proposed MRBAC	II1	0.879	0.018	0.930	0.864	0.927	3.464
	II2	0.702	0.019	0.843	0.689	0.816	2.000
	II3	0.801	0.111	0.853	0.721	0.838	2.646
	II4	0.972	0.278	0.865	0.761	0.864	2.646
	II5	0.927	0.085	0.923	0.855	0.922	2.828

Table 4.5: Averaged performance measures obtained by different segmentation methods for all MR images of infarct

Methods	TP (AVG \pm STD)	FP (AVG \pm STD)	ACC (AVG \pm STD)	JSI (AVG \pm STD)	DC (AVG \pm STD)	HD (AVG \pm STD)
Region Growing	0.821 \pm 0.145	0.155 \pm 0.113	0.842 \pm 0.024	0.705 \pm 0.059	0.825 \pm 0.041	3.339 \pm 0.808
DRLSE	0.824 \pm 0.081	0.136 \pm 0.136	0.854 \pm 0.039	0.729 \pm 0.065	0.842 \pm 0.044	2.843 \pm 0.563
Proposed MRBAC	0.856 \pm 0.096	0.102 \pm 0.095	0.883 \pm 0.037	0.778 \pm 0.070	0.873 \pm 0.044	2.717 \pm 0.468

In addition to all these subjective assessments of the MR brain infarct images, different quantitative evaluation has been also done with respect to various performance metrics as stated in Table 4.4. The corresponding averaged quantitative findings are mentioned in Table 4.5, which illustrate that the accuracy of proposed segmentation method is 88.3% than compared to 84.2% and 85.4% for Region Growing and DRLSE methods respectively. This shows the proposed method outperforms the other comparative methods. The additional

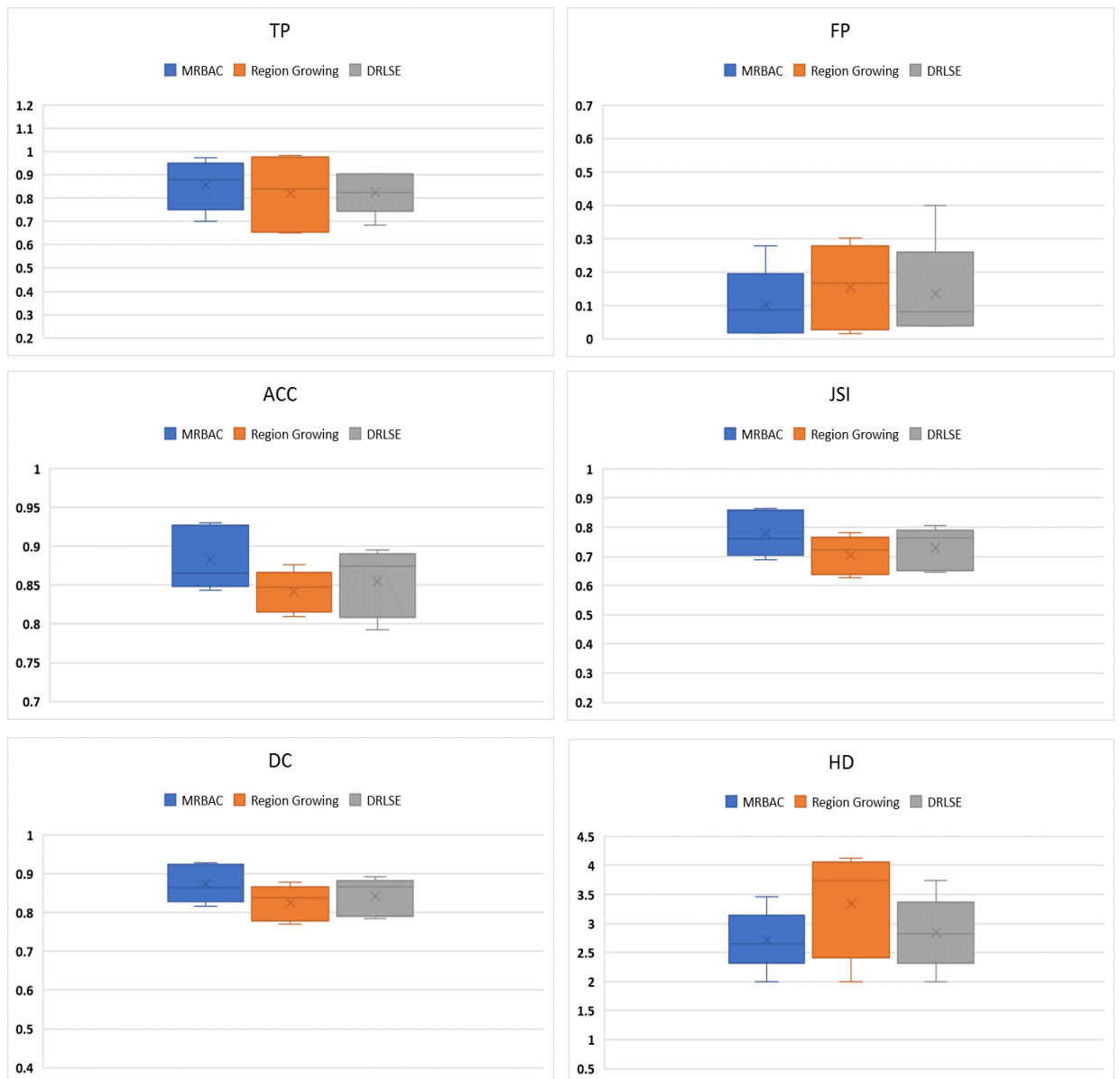


Figure 4.6: Box plot of True Positive (TP), False Positive (FP), Accuracy (ACC), Jaccard Similarity Index (JSI), Dice Coefficient (DC) and Hausdorff Distance (HD) measurements of all the Infarct MR images shown in Figure 4.5 by proposed MRBAC, Region Growing and DRLSE segmentation methods

performance measures like JSI and DC acquired by the proposed approach also achieves advanced values when compared with others which indicate that greater part of similar region is segmented by MRBAC technique than the other method. The averaged TP ratio attained by proposed method is 85.6 %, which is also high but for certain images it gives lower TP values than other. It is due to the blurred unclear regions near the boundaries which are very hard to be differentiated with real boundaries. Figure 4.6 is the box plot of each quantitative matrices obtained by Region Growing, DRLSE and the proposed method for better representation of result. It can be seen from the box plot that MRBAC approach achieves higher TP, ACC, DC and JSI values and lower FP and HD values. It can also be observed that the median of TP, ACC, JSI, DC values and FP, HD values attained by the MRBAC approach are at the higher end and lower end respectively. Furthermore, the spread in the values is also minimal which indicates that the proposed approach is superior as compared with others in term of effective delineation of the infarct areas of brain MRI.

Moreover, the computational time for all the segmentation models is also been evaluated. The specifics of processing time along with the average number of iterations used to extract the region of all the images is listed in Table 4.6. The proposed MRBAC approach takes less time and a smaller number of iterations in comparison to the others.

Table 4.6: Comparative performance of segmentation approach with averaged number of iteration and averaged computational time for all infarct images

Methods	Averaged resolution	Averaged Iterations	Averaged computation time (s)
Region Growing	256x256	123	10.97
DRLSE	256x256	166	14.33
Proposed MRBAC	256x256	98	8.78

4.9.3 Experiment No. 3:

Analysis and evaluation of segmentation results for Brain Hemorrhage images- Thirty-four images in all the three axial, coronal and sagittal planes are taken for evaluating the performance of the proposed method on hemorrhagic MR images. Out of thirty-four, sixteen T1-weighted image and eighteen T2-weighted images are selected for experimentation. All images are resized to 256×256.

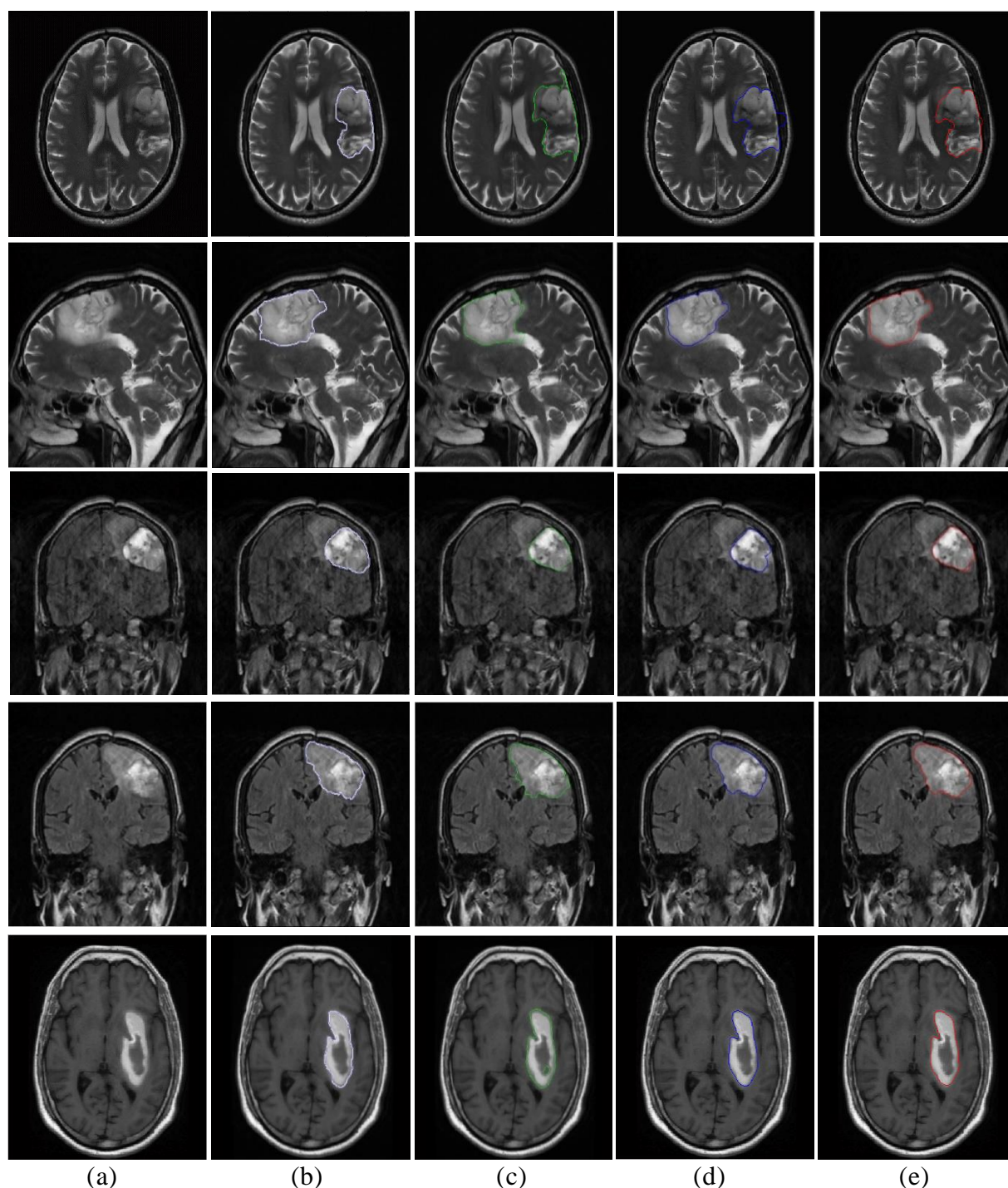


Figure 4.7: Comparative visual analysis of segmentation result of different Hemorrhage MR image obtained by (a) original image (b) ground truth marked by radiologist (c) segmented by Region Growing method (d) segmented by DRLSE method (e) segmented by proposed MRBAC method.

Segmentation results of five different hemorrhage MR images are presented in a qualitative manner in Figure 4.7. The image shown in first row is an axial T2-weighted MR image of the parenchymal hemorrhage with moderate surrounding edema. Second row image

refers to the sagittal T2-weighted image MR image while third row and fourth row image are coronal T2-weighted image of the same subject. The axial T1-weighted image shown in third row refers to the left frontal and parietal lobes with the presence of parenchymal hemorrhage. Last row image is the T1-weighted image in axial view of the subacute parenchymal hemorrhage in the left basal ganglia. Figure 4.7 shows the comparison of segmentation results obtained by Region Growing and DRLSE segmentation methods with that of proposed MRBAC method. First column of Figure 4.7 is the original image while the second column represents the ground truth marked by the radiologist. Third and fourth column of Figure 4.7, represents the extracted region boundaries provided by Region Growing method, DRLSE method, respectively. From the last column, it can be seen that the proposed technique precisely segments the whole hemorrhage areas of the brain MRI. In presence of inhomogeneities some region of the hemorrhage is left out by DRLSE and Region Growing method. From the results, it can be said that the proposed technique effectively segments iso to hypointense hemorrhage bearing poor boundaries. It shows superiority of MRBAC method over other segmentation approaches.

Table 4.7: Performance measures obtained by different segmentation methods for MR images of hemorrhage shown in Figure 4.7

Methods	Images	TP	FP	ACC	JSI	DC	HD
Region Growing	H I 1	0.986	0.247	0.881	0.791	0.883	4.000
	H I 2	0.932	0.124	0.907	0.829	0.906	3.873
	H I 3	0.830	0.021	0.904	0.813	0.897	3.873
	H I 4	0.941	0.094	0.925	0.860	0.925	4.123
	H I 5	0.958	0.185	0.894	0.808	0.894	2.828
DRLSE	H I 1	0.962	0.187	0.894	0.810	0.895	4.796
	H I 2	0.894	0.076	0.910	0.831	0.908	3.000
	H I 3	0.773	0.016	0.877	0.760	0.864	3.873
	H I 4	0.872	0.038	0.916	0.840	0.913	4.000
	H I 5	0.980	0.102	0.941	0.889	0.941	2.236
Proposed MRBAC	H I 1	0.960	0.135	0.916	0.846	0.916	3.464
	H I 2	0.933	0.093	0.921	0.853	0.921	3.000
	H I 3	0.829	0.017	0.905	0.815	0.898	3.317
	H I 4	0.895	0.038	0.928	0.862	0.926	3.742
	H I 5	0.977	0.101	0.940	0.888	0.941	2.449

Besides these qualitative assessments of all the MR brain hemorrhage images, quantitative study is done by computing different performance metrics as mentioned in the segmentation assessment criteria. Their corresponding quantitative results are listed in Table 4.7. From Table 4.8, it can be seen that averaged TP ratio acquired by MRBAC method is less than the averaged TP value obtained by Region Growing method though the averaged performance of the proposed MRBAC method in terms of accuracy gain approximately 92.2% segmentation accuracy than compared to 90.2% and 90.8% for Region Growing and DRLSE methods respectively. It is due to much lower values of FP obtained by proposed MRBAC method. JSI and DC calculated by the MRBAC approach attain higher values than compared to other methods. This implies that the proposed segmentation method is comparable with the ground truth marked by radiologist.

Table 4.8: Averaged performance measures obtained by different segmentation methods for all MRI images of hemorrhage

Methods	TP (AVG \pm STD)	FP (AVG \pm STD)	ACC (AVG \pm STD)	JSI (AVG \pm STD)	DC (AVG \pm STD)	HD (AVG \pm STD)
Region Growing	0.929 \pm 0.053	0.134 \pm 0.077	0.902 \pm 0.015	0.820 \pm 0.023	0.901 \pm 0.014	3.740 \pm 0.465
DRLSE	0.896 \pm 0.074	0.084 \pm 0.060	0.908 \pm 0.021	0.826 \pm 0.042	0.904 \pm 0.025	3.581 \pm 0.881
Proposed MRBAC	0.919 \pm 0.053	0.077 \pm 0.043	0.922 \pm 0.012	0.853 \pm 0.024	0.920 \pm 0.014	3.194 \pm 0.443

Figure 4.8 illustrate the box plot all the quantitative matrices obtained by Region Growing method, DRLSE method and the proposed method. It can be observed from box plot that, MRBAC method achieves higher ACC, DC and JSI values and lower TP, FP and HD values. The median values of TP, ACC, JSI and DC found by the proposed MRBAC segmentation method are highest and that of FP and HD are lowest and is not skewed. This indicates that proposed method is better in successful extraction of hemorrhage area of brain MRI as compared to others.

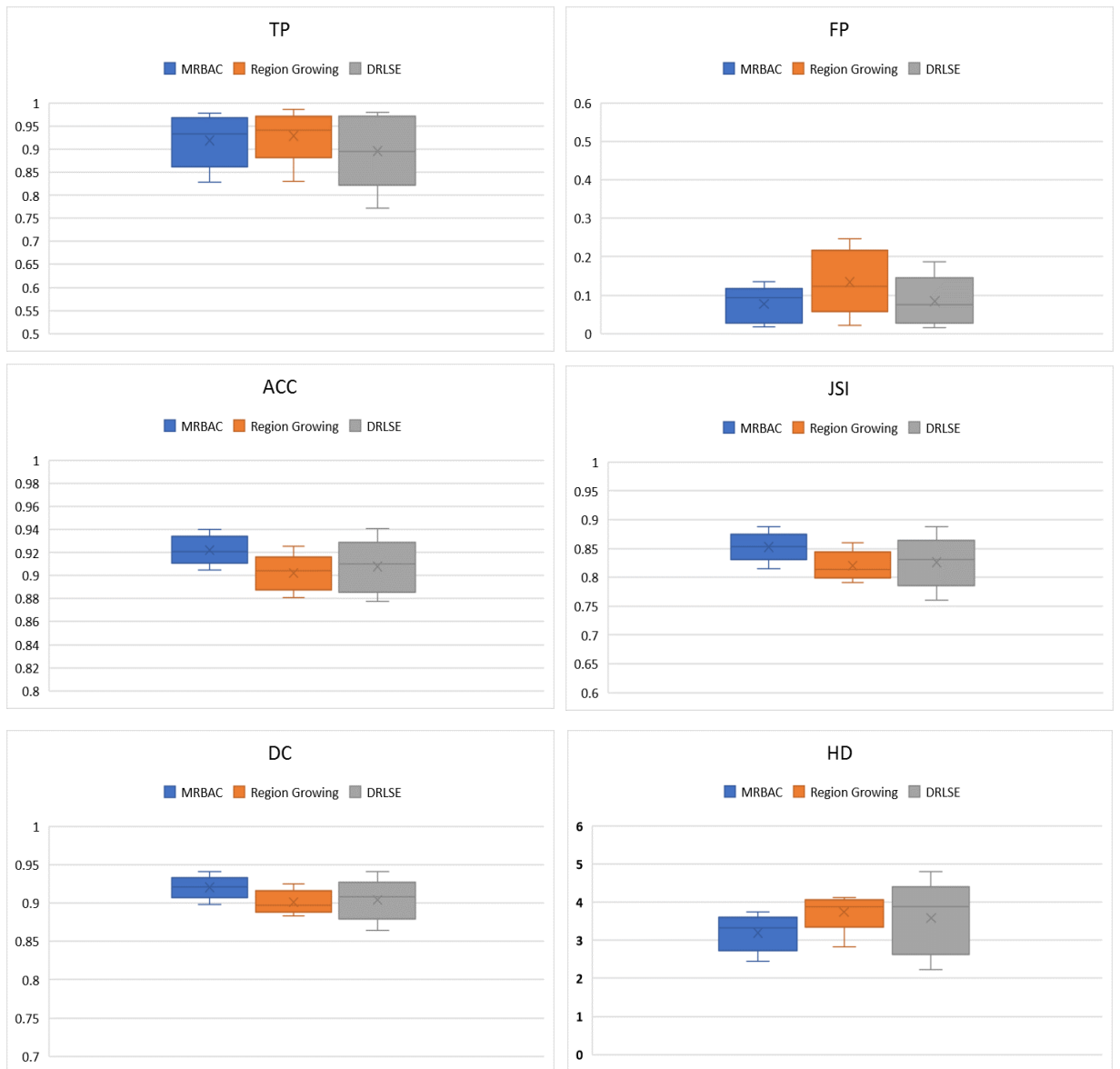


Figure 4.8: Box plot of True Positive (TP), False Positive (FP), Accuracy (ACC), Jaccard Similarity Index (JSI), Dice Coefficient (DC) and Hausdorff Distance (HD) measurements of all the Hemorrhage MR images shown in Figure 4.7 by proposed MRBAC, Region Growing and DRLSE segmentation methods

Moreover, the computational cost for each segmentation techniques is also been evaluated. Table 4.9 illustrates the processing time and the average iteration number to segment the hemorrhage areas of all the images that are shown in Figure 4.7. It can be seen

from the Table that the proposed method takes less time and a smaller iteration number as compared to other methods.

Table 4.9: Comparative performance of segmentation approach with averaged number of iteration and averaged computational time for all hemorrhage images

Methods	Averaged resolution	Averaged Iterations	Averaged computation time (s)
Region Growing	256x256	236	20.41
DRLSE	256x256	278	24.64
Proposed MRBAC	256x256	190	16.69

4.10 Conclusion

Segmentation of brain lesion has always been the most challenging task on account of the brain complex structure and inter observer readability which require significant degree of accuracy and precision. The performance of MRBAC algorithm was evaluated on sets of in-vivo medical images. Due to distinct local variance, even in presence of severe intensity inhomogeneities, MRBAC completely extracts boundaries of the lesion. Segmentation ambiguity increases if the lesion is not perfectly clear, i.e. if it has fuzzy visibility due to varied reasons like machine or subject developed artifacts, presence of homogeneous lesion isointense near the similar intensity brain parenchyma and presence of perilesional edema surrounding lesion near similar background. Sometimes lesion infiltration into the normal tissue additionally creates dilemma. For achieving better and more accurate segmentation of abnormalities from brain MR images, these challenges are compensated by the steps involved in the adopted MRBAC segmentation model.

From evaluation point of view, it is thereby inferred that the proposed MRBAC method is efficient and satisfactorily segments the required region of interest in pathological MRIs.

CHAPTER 5

FEATURE EXTRACTION AND DISEASE CLASSIFICATION

5.1 Introduction

This chapter deals with the classification issues of different types of lesions. Two approaches are presented for this purpose. First one deals with the segregation of normal parenchyma from the pathologic brain when presented with the data pool of unknown brain images. For this type of separation between normal and abnormal slices, a rationale is developed. Afterwards, if the pathology is confirmed, different subsets of type of lesion can be grouped by multiclass class classification. The first part of the classification of MR images has already been dealt with numerous researchers in the past [157,160, 161, 162, 217]. However, multiclass brain lesion study comprising to 3 major fatal types, i.e., brain hemorrhage, brain infarction and brain tumor, has yet not been attempted together. These lesions mimic each other arising subjective variations thereby leading to classification ambiguity. These pathologies constitute the highest mortality rate world-wide and require quick differential diagnosis. Presence of protein, fat (e.g. lipomas or dermoids), calcification, residual gadolinium-based contrast material and chemical shift artefact on MR images may cause ambiguity in classification between hemorrhage, infarcts and tumors mimicking each other. Also, inhomogeneities, noise, the iso to hypo intensity pattern, heterogeneity and associated edema surrounding lesion also leads to misclassification. It has been recognized and emphasized time and again that early and correct classification of pathologies can reduce casualty caused by these emergency conditions. To the best of our knowledge this study is a first of its kind dealing with three most confusing pathologies which mimic each other. The eventual success or failure of any CAD system is linearly proportional to the classification approach adapted defined by the model.

The flow diagram of the lesion classification system is given in Figure 5.1. The block wise clarification of the flow diagram is given in the following sections.

5.2 Dataset

In this study, dataset is grouped into two types of pulse sequence namely: T1-weighted images and T2-weighted images. Reaching this resolution is based on the availability of dataset as well as intra and inter-lesion specific visibility on the sequence.

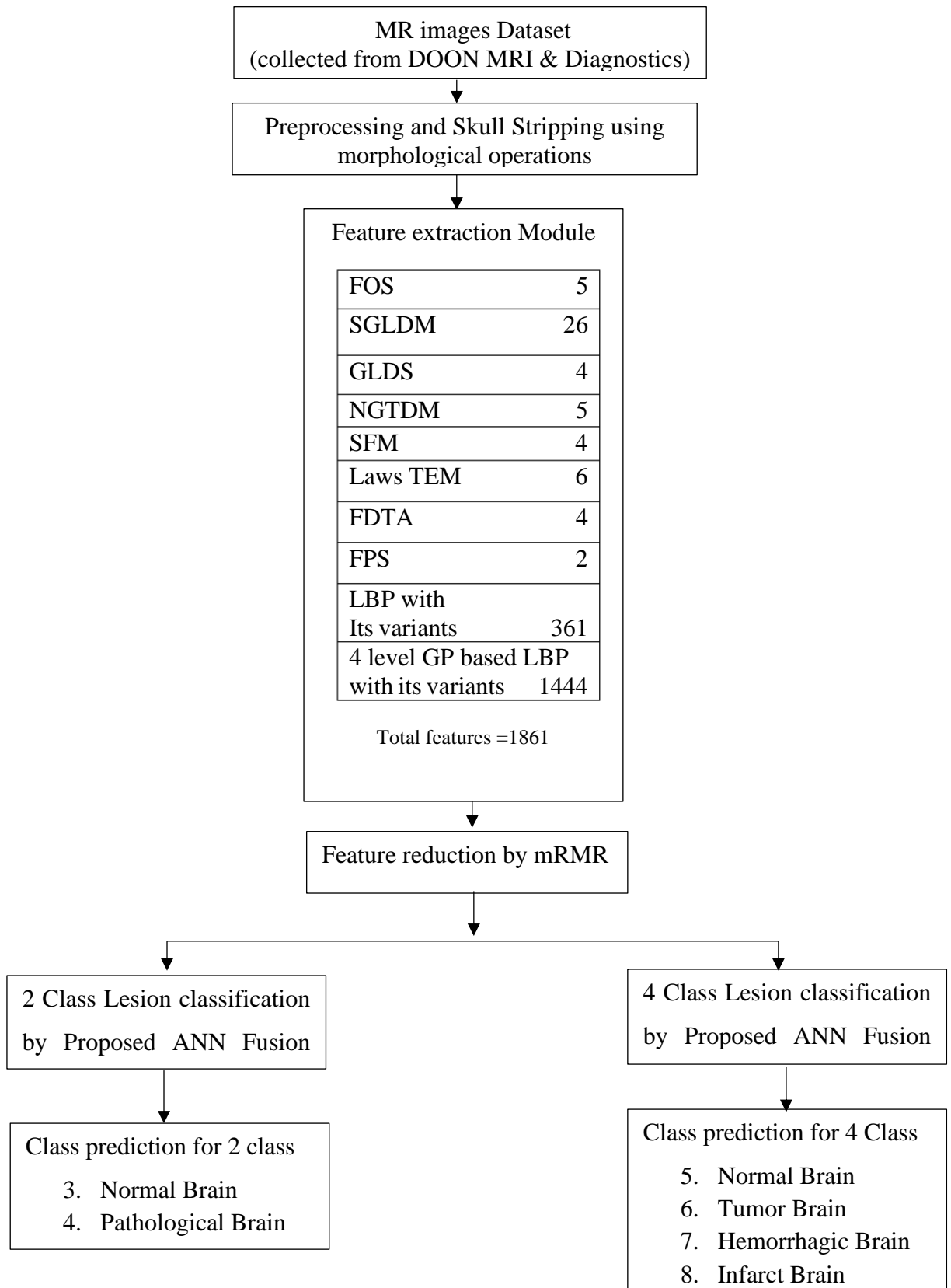


Figure 5.1: Proposed multi lesion classification scheme

5.3 Feature Extraction

This section, an illustrates the tools for extracting image parameters which are useful in representation and description. Lesion classification is based on prime features and the mechanics for calculating these parameters is laid in this section.

The internal characteristics of the pathological area comprising of pixels within that region of MR image of each pathologies are variable thereby giving each a different meaning. These characteristics or region descriptors are useful in identification, representation and description purposes. To discriminate diseases among various classes, each class is mathematically analyzed by extracting its features. These set of metrics are used to obtain information regarding the change in intensity in an image in spatial domain. Hence, the spatial arrangement of recurring patterns of texel's can be known using textural features. For image analysis, these parameters are of immense importance as they provide feasibility of numerical separations among various classes marked by different tissue types. These calculated features are used in classification purposes in whole spectrum of fields for example medical imaging, robotics, remote sensing, video analysis, face recognition, traffic monitoring, automatic weed detection and crop spraying etc. This section briefly describes the statistical texture features employed in this work.

5.3.1 Intensity Based Features (IBFs) or First Order Statistics Features (FOS Features)

These features are important as lesion intensity pattern can be hyper, hypo or iso intense as illustrated in chapter 1. This is the straightforward statistical analysis which is used for extracting the basic image related information on the ground of probability distribution of grey values of pixel [246]. The mean (μ), median, standard deviation (STD), skewness and kurtosis were calculated from the image histogram of region of lesion. The difference in between the highest and lowest intensity values in a predefined area surrounding point (x, y) is called as the image “range” feature of that point. Similarly, four other features are computed for range filter output within the regions of interest (ROI). Besides the calculation of above features, computation of mean entropy of ROI of the initial as well as the range filtered image has also been done. The image intensity of lesion is presented in the form of function $I(i, j)$ defined by 2 spatial variables i, j ; wherein, $i = 1, 2, \dots, M$ and $j = 1, 2, \dots, N$. The intensity $I(i, j)$ can have discrete values from $k = 0, 1, 2, \dots, L - 1$, where, L denotes the overall intensity levels of an image. Then the histogram is mathematically expressed as:

$$h(k) = \sum_{i=1}^M \sum_{j=1}^N \delta(f(i, j), k) \tag{5.1}$$

Here $\delta(p, q)$ is Kronecker delta function represented as

$$\delta(p, q) = \begin{cases} 0 & \text{if } p \neq q \\ 1 & \text{if } p = q \end{cases} \quad (5.2)$$

The term normalized grey level histogram $p(k)$ denotes the probability density function (pdf) of prevalence of intensity levels and is computed as the ratio of $h(k)$ to the entire pixel count in the $N \times M$ image.

$$p(k) = \frac{h(k)}{NM}, \quad k = 0, 1 \dots L - 1 \quad (5.3)$$

Mean (μ): The mean (μ) is characterized as an addition of all the intensity values of pixels in the ROI of an image over the entire pixel count of that region in the image. It constitutes to the first central moment, indicating the average level value of ROI. Mean is given by:

$$\mu = \frac{1}{N} \sum_i \sum_j I(i, j) \quad (5.4)$$

Here $I(i, j)$ represent the pixel intensity and N is the total pixel count of ROI. It is generally more appropriate for symmetrical distributions.

Standard Deviation (STD): The dispersion of grey level around the mean is known as standard deviation. It is given as:

$$STD = \sqrt{\frac{\sum_i \sum_j (I(i, j) - \mu)^2}{N}} \quad (5.5)$$

It gives information about the spread or range of gray level around the mean. Since range is calculated by using the values of two extremities, so STD can be looked up the crude measure of variability.

Skewness: Shape is important element to give information about the intensity distribution. It is defined by the third central moment of the intensity distribution and is considered as criteria for estimating the magnitude symmetry or asymmetry of gray level values around the mean. It is defined as:

$$Skewness = \frac{1}{N} \frac{\sum_i \sum_j (I(i, j) - \mu)^3}{std^3} \quad (5.6)$$

Kurtosis: It is another shape measure. It is defined by the fourth central moment of the intensity distribution. Kurtosis measures the resemblance of intensity distribution to the normal Gaussian shape and is expressed as:

$$Kurtosis = \frac{1}{N} \frac{\sum_i \sum_j (I(i,j) - \mu)^4}{std^4} \quad (5.7)$$

Entropy: It denotes the degree of randomness in grey level intensity distributions of an image and concur to the gray levels which the individual pixels can acquire. It is given by:

$$Entropy = - \sum_{k=0}^{L-1} h(k) \ln (h(k)) \quad (5.8)$$

5.3.2 Spatial Gray Level Dependence Matrices Features (SGLDM features)

This is the second order statistical tool in which co-occurrence matrices gives back the spatial distribution of joint histogram of intensity values of a pair of pixels with a given spatial relationship [39,155]. Thus, SGLDM calculates the probability of pixel pair of specific orientation θ (0° , 45° , 90° , 135°) at particular distance which have gray level value i and j occurring in an image. Over all 13 texture features were generated with $d=1$, angles $\theta = 0^\circ$, 45° , 90° and 135° , which are calculated from equation (5.15) to equation (5.27), contributing to the feature pool. The mean and range of each with 4 distinct offsets are calculated and are applied in combination.

If $p(i, j)$ is the $(i, j)^{th}$ entry in the normalized SLGDM and $P_x(i)$ and $P_y(j)$ are the i^{th} , j^{th} entry in the marginal probability matrix then the mean and standard deviation of rows and columns of the matrix is given below:

$$\mu_x = \sum_{i=1}^{N_g} \sum_{j=1}^{N_g} ip(i, j) \quad (5.9)$$

$$\mu_y = \sum_{i=1}^{N_g} \sum_{j=1}^{N_g} jp(i, j) \quad (5.10)$$

$$\sigma_x = \sum_{i=1}^{N_g} \sum_{j=1}^{N_g} (i - \mu_x)^2 p(i, j) \quad (5.11)$$

$$\sigma_y = \sum_{i=1}^{N_g} \sum_{j=1}^{N_g} (j - \mu_y)^2 p(i, j) \quad (5.12)$$

where μ_x , μ_y , σ_x , σ_y represents mean and standard deviation of P_x , P_y respectively and N_g is the number of gray levels. The probabilities P_{x+y} and P_{x-y} are related to particular intensity sums as well as differences, are given as:

$$P_{x+y}(k) = \sum_{i=1}^{N_g} \sum_{j=1, i+j=k}^{N_g} p(i, j), \quad k = 2, 3, 4 \dots \dots 2N_g \quad (5.13)$$

$$P_{x-y}(k) = \sum_{i=1}^{N_g} \sum_{j=1, |i-j|=k}^{N_g} p(i, j), \quad k = 0, 1, 2, 3, \dots (N_g - 1) \quad (5.14)$$

The following attributes are calculated in the thesis are defined as:

$$\text{Contrast}_{sgldm} = \sum_{n=0}^{N_g-1} n^2 \left\{ \sum_{n=1}^{N_g} \sum_{j=1, |i-j|=n}^{N_g} P(i, j) \right\} \quad (5.15)$$

$$\text{Angular second moment}_{sgldm} = \sum_{i=1}^{N_g} \sum_{j=0}^{N_g} \{P(i, j)\}^2 \quad (5.16)$$

$$\text{Entropy}_{sgldm} = - \sum_{i=1}^{N_g-1} \sum_{j=0}^{N_g-1} P(i, j) \log (P(i, j)) \quad (5.17)$$

$$\text{Correlation}_{sgldm} = \sum_{i=1}^{N_g-1} \sum_{j=0}^{N_g-1} \frac{(i-\mu_x)(j-\mu_y)}{\sigma_x \sigma_y} P(i, j) \quad (5.18)$$

$$\text{Variance}_{sgldm} = \sum_{i=1}^{N_g} \sum_{j=0}^{N_g-1} (i - \mu)^2 P(i, j) \quad (5.19)$$

$$\text{Inverse difference moment}_{sgldm} = \sum_{i=1}^{N_g-1} \sum_{j=0}^{N_g-1} \frac{1}{1+(i-j)^2} P(i, j) \quad (5.20)$$

$$\text{Sum Entropy}_{sgldm} = - \sum_{i=2}^{2N_g} P_{x+y}(i) \log \{P_{x+y}(i)\} \quad (5.21)$$

$$\text{Sum Variance}_{sgldm} = \sum_{i=2}^{2N_g} (i - \text{Sum Entropy}_{sgldm})^2 P_{x+y}(i) \quad (5.22)$$

$$\text{Sum Average}_{sgldm} = \sum_{i=2}^{2N_g} i P_{x+y}(i) \quad (5.23)$$

$$\text{Difference Variance}_{sgldm} = \text{Variance of } P_{x-y} \quad (5.24)$$

$$\text{Difference Entropy}_{sgldm} = - \sum_{i=0}^{N_g-1} P_{x-y}(i) \log \{P_{x-y}(i)\} \quad (5.25)$$

Information measure of Correlation (IMC_{sgldm}) are defined as:

$$IMC1_{sgldm} = \frac{HXY - HXY1}{\max\{HX, HY\}} \quad (5.26)$$

$$IMC2_{sgldm} = \sqrt{1 - \exp(-2.0(HXY2 - HXY))} \quad (5.27)$$

Where,

$$HXY = - \sum_i \sum_j P(i, j) \log(P(i, j)) \quad (5.28)$$

$$HXY1 = - \sum_i \sum_j P(i, j) \log\{P_x(i)P_y(j)\} \quad (5.29)$$

$$HXY2 == - \sum_i \sum_j P_x(i)P_y(j) \log\{P_x(i)P_y(j)\} \quad (5.30)$$

5.3.3 Gray Level Difference Statistics Features (GLDS Features)

This algorithm extracts important texture feature by the use of 1st order statistics in the image. If the image pixel pair which are at a particular distance $\delta \equiv (\Delta x \Delta y)$ and have some absolute gray level difference value, then the probability density ' P_δ ' value of that pixel pair can be calculated by GLDS. Four different set of features for displacements $\delta = (0, 1), (1, 1), (1, 0), (1, -1)$, where $\delta \equiv (\Delta x \Delta y)$, along with their means are calculated. Thus, contrast, angular second moment, entropy, and mean, are generated from GLDS algorithm which is based on absolute differences between pairs of gray levels [247].

5.3.4 Neighborhood Gray Tone Difference Matrix Features (NGTDM Features)

On the basis of visual perception, [248] conceptualize NGTDM to calculate texture measures. The column vector containing G elements are known as an NGTDM. The difference in-between intensity of pixel and the average intensity of the pixel is calculated by sliding window centered at pixel. These values are the entries to the NGTDM. If at point (x, y) the image intensity is f (x, y) and i = 0,1, 2,..G-1 is the intensity level in NGTDM then average intensity over a window centered at (x, y) is

$$\bar{f}_i = \bar{f}(x, y) = \frac{1}{W-1} \sum_{m=-K}^K \sum_{n=-k}^K f(x + m, y + n) \quad (5.31)$$

Where the window $W = (2K + 1)^2$ has size K. The i^{th} value of the NGTDM is:

$$s_i = \sum_{x=0}^{M-1} \sum_{y=0}^{N-1} |i - \bar{f}_i| \quad (5.32)$$

This value is computed for all the pixels having the intensity level i . Here the contrast, coarseness, busyness, complexity and strength are measured as:

$$Coarseness_{NGTDM} = (\epsilon + \sum_{i=0}^{G-1} P_i s_i)^{-1} \quad (5.33)$$

Where ϵ, P_i are the small number to prevent coarseness coefficient becoming infinite and the estimated probability of occurrence of the intensity level i respectively. Here, $P_i = N_i/n$, where N_i denotes the number of pixels which constitute to level i and $n = (N - K)(M - K)$.

$$Contrast_{NGTDM} = \left[\frac{1}{N_t(N_t-1)} \sum_{i=0}^{G-1} \sum_{j=0}^{G-1} P_i P_j (i - j)^2 \right] \left[\frac{1}{n} \sum_{i=0}^G s(i) \right] \quad (5.34)$$

$$Buyness_{NGTDM} = \frac{\sum_{i=0}^G P_i s(i)}{\sum_{i=0}^{G-1} \sum_{j=0}^{G-1} |i-P_j|}, \quad P_i \neq 0, P_j \neq 0 \quad (5.35)$$

$$Complexity_{NGTDM} = \sum_{i=0}^{G-1} \sum_{j=0}^{G-1} \frac{|i-j|}{n(P_i-P_j)} [P_i s(i) + P_j s(j)], \quad P_i \neq 0, P_j \neq 0 \quad (5.36)$$

$$Strength_{NGTDM} = \frac{\sum_{i=0}^{G-1} \sum_{j=0}^{G-1} (P_i+P_j)(i-j)^2}{\epsilon + \sum_{i=0}^{G-1} s_i} \quad (5.37)$$

This study employs 3x3 neighbourhood size for the retrieving features which are namely, contrast, coarseness, busyness, complexity, and strength.

5.3.5 Statistical Feature Matrix (SFM Features)

This method evaluates statistical characteristics of the pair of pixels within an image at several distances [151]. The SFM order is taken as $(L_r + 1) \times (2L_c + 1)$ where L_r, L_c are the constants which are accountable for the maximal inter-sample arrangement space. The d statistical feature of the image is the (i, j) element of the SFM, where $d = (j - L_c, i)$ is an inter-sample spacing distance vector for $= 0, 1, \dots, L_r, j = 0, 1, 3 \dots, 2L_c$. In our study the value of L_r, L_c is assigned as 4. The SFM texture features contributes by producing as contrast, coarseness, roughness and periodicity in the feature pool.

5.3.6 Laws Textures Energy Measure Features (Laws TEM Features)

Laws created a technique for classifying each pixel of a textured image on the basis of texture energy which computes the extent of variation in a definitive window size [249]. In order to extract the Laws TEM features the length ‘ l ’ of the vectors is taken as seven in this work. Also, $= (1,6,15,20,15,6,1)$, $E = (-1, -4, -5,0,5,4,1)$ and $S = (-1, -2,1,4,1, -2, -1)$ are used, where L, E, S are local averaging, edge detector and spot detector respectively. Here convolution of vector was done with one another or with themselves, and LL, EE, SS kernel is used to compute LL -texture energy, EE -texture energy, SS -texture energy respectively. The LE -average texture energy, ES -average texture energy and LS -average texture energy are thereby calculated from $(LE, EL), (ES, SE)$ and (LS, SL) kernels respectively.

5.3.7 Fractal Dimension Texture Analysis (FDTA Features)

Mandelbrot [250] proposed fractional Brownian motion model for expressing the coarseness of natural surfaces. For image resolutions $r = 1,2,3,4$; $H(r)$ (Hurst coefficient) is

computed. Surface smoothness and roughness is indicated by the H value when H is large or small respectively.

5.3.8 Fourier Power Spectrum Features (FPS Features)

The angular sum and the radial sum of the discrete Fourier transform [247] are calculated for representing texture.

5.3.9 Local Binary Pattern Features (LBP Features)

First order circular derivative patterns are generated by concatenating the binary gradient directions [168]. LBP features along with its variants like LBP^{u2} , LBP^{ru2} and LBP^{riu2} are generated as discussed briefly in the following sections [169-174].

5.3.9.1 Local Binary Pattern (LBP)

First order circular derivative patterns are generated by concatenating the binary gradient directions. Each pixel is labeled by this texture operator using relative gray levels of its circular neighborhood pixels. The center pixel coordinate (x, y) of an image is represented as LBP label by equation (5.38)

$$LBP_{P,R}(x, y) = \sum_{p=0}^{p-1} s(g_p - g_c) 2^p \quad (5.38)$$

$$s(x) = \begin{cases} 1, & x \geq 0 \\ 0, & otherwise \end{cases}$$

Where, g_c and g_p stands for gray level of the central pixel and the corresponding gray level of the p^{th} neighborhood of the central pixel respectively. In the $LBP_{P,R}$ operator P, R are the number of pixels in the neighborhood and the radius respectively.

5.3.9.2 Uniform Local Binary Pattern (LBP^{u2})

If the maximum of 2-bitwise transition is reported (1 to 0 or 0 to 1), then the LBP pattern are said to be uniform LBP pattern. The LBP^{u2} histogram consists of different bins for uniform pattern but for all non-uniform pattern only one bin is assigned. If the given pattern is of P bits, then $P(P - 1) + 3$ output bins are produced. In natural images the LBP patterns are generally uniform and so there is reduction in non-uniform patterns. Also, uniform pattern of texture images constitutes of 90% of the entire pattern with (8, 1) neighborhood and close to 70% for (16, 2) neighborhood. The LBP^{u2} gives 59- dimensional texture descriptors.

5.3.9.3 Rotation Invariant Local Binary Pattern (LBP^{ri})

Image rotation can lead to multiple LBP codes. To attend the issue to image rotation LBP^{ri} is used. To make every version of binary codes similar, LBP codes are rotated back to reference pixel position, thereby nullifying the effect resulting from translation of a pixel location. $LBP_{P,R}^{ri}$ is generated by circularly rotating the basic LBP code and considering the pattern which gives minimum value. It is given as:

$$LBP_{P,R}^{ri} = \min \{ROR(LBP_{P,R}, i) | i = 0, 1, 2 \dots p - 1\} \quad (5.39)$$

where, the 'ri' subscript stands for rotation invariant. The $ROR(x, i)$ function circularly moves the P bit binary number ' x ', i times to the right ($|i| < P$). The $LBP_{P,R}^{ri}$ descriptor generates overall 36-bin histograms for every image due to 36 diverse, 8-bit rotation invariant codes.

5.3.9.4 Rotation Invariant Uniform Local Binary Pattern (LBP^{riu2})

A pattern is said to be 'uniform' pattern $U(x)$ if the pattern has uniformity value $U \leq 2$. It is given as:

$$U(x) = \sum_{p=0}^{p-1} F_b(x \oplus ROR(x, 1), p) \quad (5.40)$$

Where, b stands for binary number. For a given binary number x , the circularly consecutive binary bits b is obtained by:

$$F_b(x, y) = ROR(x, i). (2^b - 1) \quad (5.41)$$

The symbols \oplus and $.$ (dot) is the bitwise logical operators 'XOR' and 'AND' respectively. For a given bit sequence i denotes the index of least significant bit (LSB). The rotation of uniform codes towards their minimum values produces $(P + 1)$ patterns. By just counting the number of ones in the 'uniform' patterns, the binary number generates the LBP^{riu2} pattern code. The other patterns are marked 'miscellaneous' and grouped into a single value given as:

$$LBP_{P,R}^{riu2} = \begin{cases} \sum_{p=0}^{p-1} s(g_p - g_c), U(G_p) \leq 2 \\ P + 1, \text{ otherwise} \end{cases} \quad (5.42)$$

The $LBP_{P,R}^{riu2}$ generates 10-bin histograms

5.4 Gaussian Pyramid

In digital world, Gaussian pyramid has been used for extensively in numerous fields [251]. The pyramid is the multi-scale representation of signal which takes place after repetitive

smoothing and subsampling. Image pyramid is useful in image analysis and synthesis, image enhancement, texture analysis. Gaussian pyramid and the Laplacian pyramid have been widely used multi resolution schemes for texture analysis of images.

Image information can be represented by the variety of data structure, although, this choice can be critical to the successful completion of image processing. In the present work, hierarchical structure Gaussian Pyramid (GP) model has been chosen out of several multiresolution techniques as it is computationally economical. The decomposed image at every level has considerable amount of information about the original image.

It comprises of the succession of images of various resolutions which change in regular steps. Here, Gaussian average (Gaussian blur) is used to weight down the subsequent images and then to scale down. Each new pixel contains the local average that corresponds to a pixel neighborhood on a lower level of the pyramid. At the bottom of the pyramid, the resolution is high while it gets low on the top. The succedent level image (G_1) in image pyramid is attained by subsampling the resultant of the convolution of the original image(G_0) and the Gaussian kernel function (low pass filter). Again, at the next level the convolution of the output image of the previous level with Gaussian kernel image is subsampled in order to get the next level image and this process continues for other levels.

The GP for an image $I(i, j)$ is

$$G_0(i, j) = I(i, j) \tag{5.43}$$

$$G_l(i, j) = \sum_{x=-2}^2 \sum_{y=-2}^2 w(x, y) G_{l-1}(2i + x, 2j + y) , 0 \leq l \leq N \tag{5.44}$$

The weighted function $w(x, y)$ mentioned in the equation (5.44) remains same at every level and is known as generating kernel which approximates the Gaussian function. These kernels are symmetric as well as separable.

5.4.1 Gaussian Pyramid Based LBP Features

Input MR images are transformed into multi-resolution image by means of GP. The G_0 to G_4 levels are calculated by convolving images with Gaussian kernel and the texture feature extraction is done using various texture descriptors of LBP. This generates a wide range of numerical values. Since, at every level of multi resolution image contains significant information of the original image, the feature vectors are combined from level 1-4 as mentioned in equation (5.45).

FEATURE EXTRACTION AND DISEASE CLASSIFICATION

Table 5.1: Details of features extracted for classification model

Feature Category		Features	Number of Features
First Order Statistical Features (FOS)		Mean, Median, Standard Deviation, Skewness, Kurtosis	5
Spatial Gray Level Dependence Matrices (SGLDM)		Mean and ranges of angular second moment, contrast, correlation, sum of squares (variance), inverse difference moment (homogeneity), sum average, sum variance, sum entropy, entropy, difference variance, difference entropy, information measures of correlation (logarithmic coefficient of correlation), information measures of correlation (classical correlation coefficient)	26
Gray Level Difference Statistics (GLDS)		Homogeneity, contrast, energy, entropy	4
Neighbourhood Gray Tone Difference Matrix (NGTDM)		Coarseness, contrast, busyness, complexity, strength	5
Statistical Feature Matrix (SFM)		Coarseness measure, contrast measure, periodicity measure, roughness measure	4
Laws Texture Energy Measures (Laws TEM)		Three texture energy features from LL, EE, SS kernel and three average texture energy features from LE & EL kernels, ES & SE kernels and LS & SL kernels.	6
Fractal Dimension Texture Analysis (FDTA)		Four Fractal Dimension Texture Analysis features	4
Fourier Power Spectrum (FPS)		Angular sum, radial sum	2
LBP & its variants	LBP	Local binary pattern	256
	LBP^{u2}	Uniform local binary pattern	59
	LBP^{ri}	Rotation invariant local binary pattern	36
	LBP^{riu2}	Rotation invariant uniform local binary pattern	10
Gaussian Pyramid based LBP & Its variants	GPLBP Level 1 to Level 4	LBP features extracted after decomposition of image by Gaussian pyramid from level1 to level 4	1024
	$GPLBP^{u2}$ Level 1 to Level 4	LBP^{u2} features extracted after decomposition of image by Gaussian pyramid from level1 to level 4	236
	$GPLBP^{ri}$ Level 1 to Level 4	LBP^{ri} features extracted after decomposition of image by Gaussian pyramid from level1 to level 4	144
	$GPLBP^{riu2}$ Level 1 to Level 4	LBP^{riu2} features extracted after decomposition of image by Gaussian pyramid from level1 to level 4	40

Total= 1861 features

$$F_L = \sum_{l=1}^{l=4} G_l \quad (5.45)$$

All features considered in the study are summarized in Table 5.1.

5.5 Feature Management and Feature Selection

5.5.1 Normalization of Calculated Features

All the prior calculated features are normalized in the range [0, 1] in order avoid the influence resulted from unbalanced texture feature values, by the formula defined below [252].

$$n(\chi^i) = \frac{(\chi^i - m_i)}{\sigma_i} \quad (5.46)$$

Where, m_i represent mean while σ_i is the standard deviation of the feature i .

5.5.2 Feature Selection

The feature selection process is an automatic process of selecting most relevant attributes necessary for enhancing accuracy and efficiency of classification procedure, typically used in the pattern recognition applications [253]. It is essentially helpful in reducing the training time when the model is presented with high dimensionality data (many features) with only a minute effect on total information. The motto of it is filter out ‘ m ’ attributes from the total no of ‘ n ’ attributes in order to get optimal subset.

If ‘ n ’ is the total no of ROIs and ‘ m ’ is the number of calculated features then to classify classes C_i by identifying the most characterizing features from the total observed data requires reduction of the M -dimensional observation space in such a way that “optimally” characterizes C_i . Empirically, it is difficult to get best subspaces exhaustively. Many search algorithms in past has been used applying individual features, sequential forward search, sequential forward floating search etc., to find the best subspace. However, most of the classification systems which are unsupervised have maximum statistical dependency of subspace of data distribution on target class C and vice-versa.

Peng et al. [198] proposed the hybrid approach called as mRMR (minimum Redundancy Maximum Relevance) which is been used in the present study. This method reduces the count of features by assigning each one a rank and then the class assigning is done.

5.6 Lesion Classification Module

Classification is a categorization process of the huge sets of objects that share similar attributes in order to recognize, differentiate and understand. Artificial Neural Networks (ANN) consisting of multiple nodes, are vaguely inspired from biological neural networks in learning. The input is given to the node or processing elements (PE) which perform some operation thereby passing its output to other neurons generating the node value called activation. Each link is associated with some weight which gets re-calibrated at every training step. ANN can handle much more variability as it has many different coefficients which can be used to optimize the model.

In the present work, Pattern Recognition tool in Neural Network (NN) Toolbox (of MATLAB®) has been used for developing the classification model to differentiate the selected anomalies from MR image of the brain.

ANN Classifier:

In image processing field, classification of input data is based on pattern recognition obtained by statistical metrics for calculating textural primitives using machine learning. This field has been extensively studied and explored at various levels. Pattern Recognition (PR) App [254] is used as a framework for brain lesion categorization of MR images. The optimal set of attributes obtained by normalization and feature selection modules explained in section 5.5, are considered as input in the classification framework. Each classifier is designed with two-layer feedforward neural network with sigmoid hidden and SoftMax output neurons. The network is trained with scaled conjugate gradient backpropagation. Five hundred input neurons are selected based on dimensionality of input data. Two output neurons are selected for two class classifier and four output neurons are selected for four class classifiers. Empirically, six neurons are selected in hidden layer which gives better result. For training and testing of the neural networks, the original dataset is divided into two parts in the ratio of 70% and 30%. First one is training dataset (TR data) which is used for the training purpose of neural networks and the other one is testing set (TE data) which is used for testing of individual as well as proposed fusion network. Original TR data is presented to the individual network designed by PR app which further subdivides images into three sets namely; training, testing and validation datasets. Since we have already reserved 30% of data for testing purpose, we allow only 5 % data selection from TR data for testing field of PR app during training. Remaining 80% and 15% data out of all original TR data are selected as training and validation data respectively.

It is realized that each time classifier gives different overall and particular class accuracy, when the network gets trained for same input dataset and tested with same testing dataset. It is because the weights assigned to the neurons of the NN are different every time when NN is retrained with the same training data set. Due to different weights assignments for the same training dataset, accuracy of NN in classifying the lesions changes every time the NN is retrained. After evaluation it is observed that each time weights differs due to the two reasons: (1) PR App itself randomly divides original training database (TR) into training, testing and validation which impacts datasets consisting of different input and target vectors every time the NN is retrained (2) Neuron initialization with random weight during each retraining process. Thus, this results in huge variation in accuracy implying the unfaithful multiclass classification of pathology. For the input vector, NN yields the probability values for each class and the class bearing maximum probability values gets selected. Sometimes, only a minor variation in probability leads to the selection of particular class. Classification for such cases can be said to have poor confidence level. For high confidence level, probability value yielded for any particular class should be far greater than the probability values yielded by the classifier for other classes. To determine the confidence level (CL) of the classifier for a given input quantitatively, the given formula is used:

$$CL = \left(\frac{P_1 - P_2}{P_1} \right) \times 100 \quad (5.47)$$

Where P_1, P_2 denotes the first and the second highest probability values yielded by the classifier. High confidence level, that is, larger than 50% are considered better suited for classification. In order to refine the reliability of the model, 10 classifiers (NN) are assembled together and this has been named as Fusion Network, which yields high accuracy with high consistency and confidence level. Each classifier is trained with same training dataset but different initial weights. For the same input vectors, all of these classifiers have different probability values for each class. Since these classifiers are independent of each other, therefore the probabilities yielded by them will also be independent. So, if the probability values attained by each classifier is averaged, the class having maximum probability value for most of the classifiers is selected as the class of the particular pathology. Proposed Fusion Network is represented in Figure 5.2.

5.7 Assessment Criteria

The elementary 2D data structure used for interpretation in context of brain lesion classification system is confusion matrix. It represents the output of the classifier in a systematic

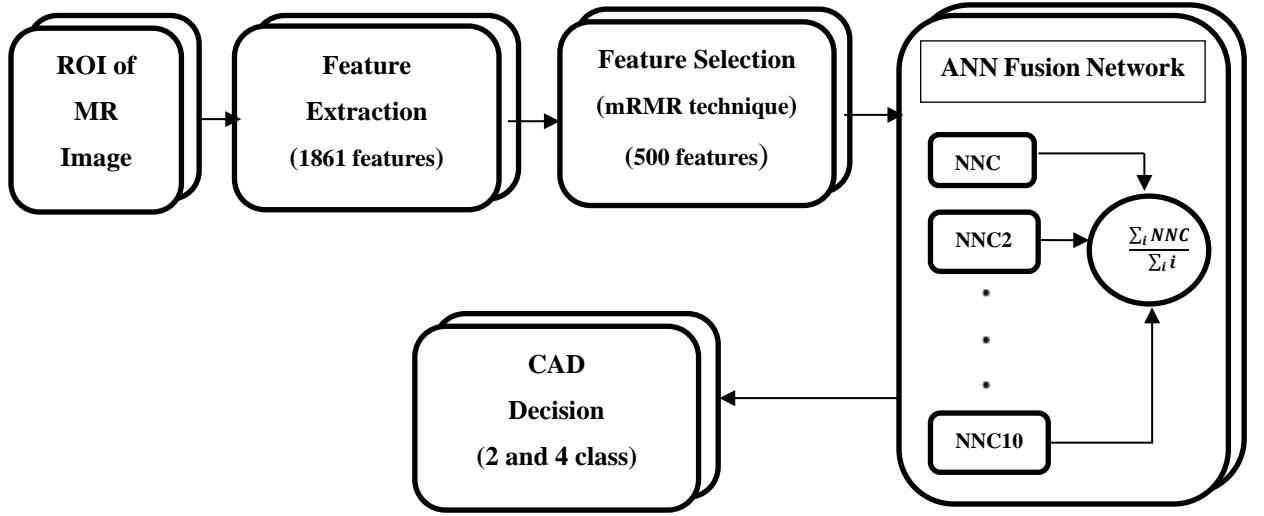


Figure 5.2: Proposed CAD system with Fusion network for classification of brain lesion MR images

tabular form, where the rows and columns depict the class prediction by radiologists (ground truth) and the classifier output respectively of an image. Classification results are then compared with the ground truth.

The diagonal element of the confusion matrix represents the correctly classified instances of each class by the classifier. The incorrectly classified instances are listed as the off-diagonal components. The capability of the system to correctly discriminate between classes is known as the performance of the classification system.

The performance of the model is given in form of class (local) accuracy specific to particular class and the classification accuracy of the model which is complete (global) accuracy inclusive of all the classes. These measures are calculated by the given formulas.

$$Class(n) = \text{Number of instances of class } (n) \text{ in dataset} \quad (5.48)$$

$$Single \text{ class accuracy for } n^{th} \text{ class} = \frac{TP(n)}{Class(n)} \quad (5.49)$$

Where $TP(n)$ represents the correctly classified instances of class (n)

Overall Accuracy: It is the overall correctness of the classification system and it is calculated as the total number of correctly classified region of interest.

$$Overall \text{ classification accuracy} = \left(\frac{\sum_n TP(n)}{\sum_n Class(n)} \right) \times 100 \quad (5.50)$$

5.8 Experimentation

In light of developing a better computer aided diagnostics tool for multiclass brain lesion classification, the following experiments are conducted in succession. Thereafter the analysis performance scrutiny is done for two class and multiclass brain lesion classification.

The following experiments are performed for evaluation of both classifiers. The performance comparison of the methods is also done for analysis of CAD systems.

Experiment no.1: Testing and evaluation of proposed classification fusion network for normal and pathological brain on MATLAB platform.

For training and testing, MR data comprising of normal brain and pathological brain has been selected separately in the ratio of 70% to 30%. Consequently, it does not allow same images to be present in both training and testing.

Experiment no. 2: Testing and evaluation of proposed classification fusion network for multiclass classification on MATLAB platform.

The dataset of three different classes of pathology namely tumor, hemorrhage and infarct are segregated along with the normal brain MR images. Here also, training and testing datasets are already divided in 70% to 30 % ratio respectively and hence the chances of subject images to be present in both training and testing are nil.

Experiment 1 simply helps in binary classification of MR brain images into two distinct categories namely normal and pathological brain. It is necessary to further examine the pathological brain images which may be detected by this experiment and hence a further experiment is required to classify the pathological images. However, in experiment 2 all these different aspects of the brain image analysis are simultaneously considered so that in a single attempt, final results may be obtained. Therefore, Experiment 2 would ideally be the only experiment required for the purpose. However, if only the health status of the brain is to be accessed then experiment 1 may be sufficient.

We have in this part of the thesis presented the methodologies and results for both of these experiments, either of which may be used as per choice of the analyst.

5.9 Results and Discussions

5.9.1 Experiment No. 1:

Testing and evaluation of proposed classification fusion network for normal and pathological brain on MATLAB platform - This work is basically directed to develop a CAD system constituting of feature extraction and classification algorithms for identification of abnormality on brain MR images thereby aiding the radiologists in decision making process. The stepwise procedure of the methodology is explained in the following sections.

Image dataset: The brain MR image database used for this experiment constitute of T1-weighted and T2-weighted image. The images are of all three planes, i.e. axial, sagittal, and coronal. Out of 488 images, 230 of them constitute normal dataset while 258 are of pathological brain MRI. All the images are taken from same machine (G E Healthcare 1.5 Tesla MR Scanner) and of same resolution.

Pre-processing and Skull Stripping: In this step all the images including normal and abnormal are first resized to 256x256 and then for better training of classifier, skull of brain MR Images is removed using morphological operations.

Feature Extraction unit: This unit draws out the intensity and textural attributes embed in the lesion image. Ten feature extraction methods are selected to extract relevant features from selected MR brain images which are: FOS, SGLDM, GLDM, NGTDM, SFM, Laws TEM, FDTA, FPS, LBP and Gaussian Pyramid based LBP with its variants e.g. LBP^{u2} , LBP^{ri} , LBP^{riu2} . Table 5.1 shows the details of features extracted. Total 1861 features extracted from above methods. These features contribute to the proposed classifier after applying the feature extraction techniques on all 488 images which are used for training and testing purpose.

Feature management and selection unit using mRMR: This unit holds up the responsibility first normalizing all the extracted attributes within the range of 0-1. In present work, mRMR technique is used for dimensionality reduction which improves the performance of the classifier. mRMR is an optimal feature selection technique and it gives rank to all extracted features according to importance of features in classifying between classes. Top 500 features are then selected empirically for input to different classification networks based on ANN. These selected features are also given to the fusion network which is a composition of ten assembled ANN classifier.

Table 5.2: Performance of 10 neural networks individually for two class classification

Neural Networks	NI Accuracy	PI Accuracy	Overall Accuracy
NNC1	89.7	92.3	91.1
NNC2	85.3	88.5	87.0
NNC3	85.3	84.6	84.9
NNC 4	88.2	91.0	89.7
NNC 5	91.2	91.0	91.1
NNC 6	92.6	92.3	92.5
NNC 7	82.4	87.2	84.9
NNC 8	86.8	89.7	88.4
NNC 9	86.8	92.3	89.7
NNC 10	88.2	87.2	87.7

Here NI, PI and NNC are normal image and pathological image, neural network classifier respectively

Classification:

Table 5.2 specifies the accuracy attained by the 10 NN trained with same training database and tested with same testing dataset. It is observed that the individual accuracy of NN varies from 82.4% to 92.6% for Normal brain parenchyma and from 84.6% to 92.3% for MR images with lesions i.e. for pathological brain. Overall accuracy of the NN is observed to have large variation from the minimum of 84.9 % to a maximum of 92.5%. So, to take decision based on these classifiers is very difficult due to its poor confidence level. To improve the classification system a fusion network is developed in which all ten neural networks are combined in such a manner which classifies the input brain MR images with higher confidence level for most of the input images. The confidence level (*CL*) as explained earlier in this chapter is calculated using equation (5.47) for each input test MR images and for all individual neural networks along with the proposed fusion network. Table 5.3 depicts the number of test input MR images which lies between different confidence levels for all networks.

From the Table 5.3 it is observed that 4, 8, 5, 7, 10, 7, 9, 6, 5 and 11 test input MR images have confidence level less than 50% for all the 10 NN respectively which imply that for some test input instances, the probabilities yielded for different classes by NN are too close to each

Table 5.3: Confidence level of 10 NNs and the proposed CAD system for two class classification

Neural Networks	Number of Test Inputs		
	<i>CL</i> > 90%	50 < <i>CL</i> < 90%	<i>CL</i> < 50%
NNC 1	131	11	4
NNC 2	118	20	8
NNC 3	120	21	5
NNC 4	114	25	7
NNC 5	112	24	10
NNC 6	121	18	7
NNC 7	116	21	9
NNC 8	118	22	6
NNC 9	123	18	5
NNC 10	109	26	11
Proposed Fusion Network	140	4	2

Here CL and NNC are confidence level and neural network classifier respectively

other that the class may wrongly be classified by these classifiers. So, the fusion network as shows in Figure 5.2 is developed in such a manner which can be used effectively to overcome the aforesaid problem.

Table 5.4: Confusion matrix of the proposed fusion network implemented in testing of dataset for two class classification

Class	NI	PI
	Ground truth	Ground truth
NI Predicted	65	5
PI Predicted	3	73
Individual Class Accuracy	95.6%	93.6%
Overall Accuracy	94.5%	

Result and Discussion Table 5.4 shows the classification result of the proposed fusion network for two class classification system. The individual class accuracy is consistent and is 95.6% and 93.6% in normal and pathological images respectively. The overall accuracy came out to be 94.5%. From this it can be concluded that the individual class and overall accuracy of the fusion network is consistent and are better than the individual classifiers.

5.9.2 Experiment No. 2:

Testing and evaluation of proposed classification fusion network for multiclass classification on MATLAB platform- This experiment includes the hybrid learning approach by employing mRMR method in conjunction with Artificial Neural Network (ANN) along with the proposed Fusion Network. The system comprises of three components: (i) Feature Extraction unit (ii) Feature management unit using mRMR which select the most dominant ones from the feature pool. The chosen features act as input to individual ANN classifiers as well as to proposed Fusion Network classifier (iii) Classification unit using proposed Fusion Network.

Images Dataset: The brain MR image database comprised of T1-weighted and T2-weighted image. The images are of all three planes, i.e. axial, sagittal, and coronal. For this classifier model, input samples of 510 images (176 Normal regions of brain, 123 Tumor brain, 107 Hemorrhagic brain and 104 Infarct brain MRI) are taken. Since, Normal Regions represent highly varying anatomical regions. Non-enhancing lesions are sometimes misclassified as NRs. Therefore, NR are included as the separate class during classification. Again, all the images are from same machine (G E Healthcare 1.5 Tesla MR Scanner) and of same resolution.

Pre-processing and Skull Stripping: In this step all the images including normal, tumor, hemorrhage and infarct are first resized to 256x256 and then for better training of classifier, skull of brain MR Images is removed using morphological operations.

Feature Extraction and Feature Selection: Ten feature extraction methods are selected to extract relevant features from selected MR brain images which are: FOS features, SGLDM, GLDM, NGTDM, SFM, Laws TEM, FDTA, FPS, LBP and Gaussian Pyramid based LBP with its variants e.g. LBP^{u2} , LBP^{ri} , LBP^{riu2} . Table 5.1 shows the details of features extracted. Total 1861 features extracted from above methods. These features contribute to the proposed classifier after applying the feature extraction techniques on 510 images which are used for training and testing purpose. These extracted features are then normalized within the range of 0-1.

Dimensionality reduction contributes to the performance of the classifier hence optimal feature selection mRMR technique is used in present work as it outputs the relevance oriented least redundant features. Top 500 feature are selected empirically for classification of four classes of brain pathology. These selected features are then given to the fusion network which is a composition of ten assembled ANN classifier.

Classification: Artificial Neural Network (ANN) based classification model is designed with single hidden layer and multi-processing unit varying from one to hundred neurons. But the model having single hidden layer and 6 processing elements is giving best performance without sacrificing the speed of the network. The network is trained with scaled conjugate gradient backpropagation method. All the experiments of classification run on PC having Intel® Core (TM) i3 CPU 2.40 GHz processor with 6 GB RAM. Out of total 510 images, the training data is of 357 images which comprises 123, 86, 75 and 73 normal, tumor, hemorrhage and infarct images respectively. The testing data is composed of 153 images which is segregated as 53, 37, 32 and

Table 5.5: Performance of 10 neural networks individually for multiclass classification

Neural Networks	NR Accuracy	TI Accuracy	HI Accuracy	II Accuracy	Overall Accuracy
NNC 1	79.2	86.5	75.0	80.6	80.4
NNC 2	90.6	89.2	90.6	90.3	90.2
NNC 3	77.4	83.8	87.5	80.6	81.7
NNC 4	88.7	81.1	84.4	74.2	83.0
NNC 5	88.7	73.0	90.6	71.0	81.7
NNC 6	84.9	91.9	68.8	90.3	84.3
NNC 7	81.1	91.9	90.6	87.1	86.9
NNC 8	73.6	86.5	90.6	80.6	81.7
NNC 9	83.0	83.8	78.1	87.1	83.0
NNC 10	88.7	91.9	90.6	90.3	90.2

Here NI, TI, HI, II and NNC are Normal image, Tumor image, Hemorrhage image, Infarct image and neural network classifier respectively

31 images of normal, tumor, hemorrhage and infarct images respectively. The ratio of 7/3 has been selected between training and testing data. Table 5.5 gives the individual class accuracies attained by the 10 NN trained with same training database and tested with same testing dataset. Also, it presents the overall accuracy of each classifier. Normal images are also included in this classification system as normal regions are highly varying anatomical regions which can sometimes be misclassified. Normal image accuracy varies from 73.6% to 90.6% for individual networks. In case of tumor, the accuracy of classifiers varies from 73% to 91.9% while there is a variation range of 75% to 90.6% for hemorrhage. Infarct accuracy values varies from 71% to 90.3% in between different classifiers. The acquired results demonstrate that the overall accuracy of each classifier varies from 80.4% to 90.2%. It can be concluded that there is a huge variation in accuracy of each pathology by the different classifiers. So, for refining the reliability of classification system, confidence level (CL) of 10 NN is calculated by using equation (5.47), explained earlier in this chapter and that is depicted in Table 5.6. It represents, the total number of test inputs having confidence level smaller than 50% are 13, 6, 8, 6, 11, 12, 9, 10, 10 and 18 for all the 10 NN respectively which imply that for some test input images, the probabilities yielded for different classes by NN are very close to one another such that the class may be

Table 5.6: Confidence level of 10 NNs and the proposed CAD system for multiclass classification

Neural Networks	Number of Test Inputs		
	$CL > 90\%$	$50 < CL < 90\%$	$CL < 50\%$
NNC 1	113	27	13
NNC 2	129	18	6
NNC 3	120	25	8
NNC 4	114	33	6
NNC 5	118	24	11
NNC 6	109	32	12
NNC 7	114	30	9
NNC 8	107	36	10
NNC 9	123	20	10
NNC 10	114	21	18
Proposed Fusion Network	145	5	3

Table 5.7 Confusion matrix of the proposed fusion network implemented in testing of dataset for multiclass classification

	NI	TI	HI	II
NI	51	0	1	1
TI	1	35	0	1
HI	1	2	29	2
II	0	0	2	27
Individual Class Accuracy	96.2%	94.6%	90.6%	87.1%
Overall Accuracy	92.8%			

misclassified by the NN.

The proposed fusion network as shows in Figure 5.2 overcomes this problem. This fusion network is trained and tested on the same set of data which were used for individual neural networks.

Results and Discussion

Table 5.7 represents the confusion matrix of the output of proposed fusion. The individual class accuracies of NI, TI, HI, II are 96.2%, 94.6%, 90.6%, 87.1% respectively. The overall accuracy of the fusion network is depicted as 92.8% which also higher in comparison with in individual neural networks. The performance of the proposed fusion is better in all the cases of lesions taken up for conducting the experiment. It can be clearly observed that the proposed fusion network outperforms the individual neural network classifiers.

5.10 Conclusion

Medical images play important role in diagnosis of diseases. Human perception is variable, so to remove the conflict and to ease the burden of recognition, classification is highly required. Classification through any CAD model is of great help to radiologist and researchers. ANN are such supervised pragmatic model which are used for class prediction and back propagation neural network (BPNN) has been proved more effective than other schemes in ANN. The proposed fusion model yields its highest accuracy of 94.5% in classification between normal and pathological brain and 92.8% in four multiclass classification.

CHAPTER 6

CONCLUSIONS AND FUTURE SCOPE

This chapter presents the conclusions based on the performance of the proposed segmentation methods and the classification approach discussed in previous chapters. In this chapter, the description of achieved objectives are presented in brief. The database, consisting of brain MR images of tumor, hemorrhage, infarct and normal subjects, obtained from DOON MRI & Diagnostics, Dehradun are considered to evaluate the performance of the proposed methodologies. The overall perspective from the result of these databases is included. The limitations and future possibilities of the present work are also investigated.

The comparison based on the comparative analysis of both the proposed segmentation method and classification approach illustrated in Appendix A and B, respectively is also presented here. This chapter also presents several possible directions of the proposed approach to be investigated in the future.

6.1 Conclusions

This thesis has focussed on segmenting the pathological region of interest (ROIs) as well as extracting the diagnostic features from the MR images of the brain and detecting or classifying lesions in brain MR images. Segmentation and classification of the three major fatalities have been taken up in this study, namely tumor, hemorrhage and infarct. Additionally, normal images are taken up as a different class during classification. Since visual perception of MR images during prognosis of disease contouring and classification is subject to inter-observer variability, so most of the effort has been directed towards designing and development of effective methods to extract particular region precisely and accurately as well as to differentiate between lesions which sometimes look alike.

MR imaging is the major tool for the detection of various human pathologies in brain. Basic MR sequences such as T1-weighted and T2-weighted images along with CT images are used by clinicians for diagnosis purpose. It is found during imaging investigations (during preoperative planning or recurrence/progression of lesions taken up in this study) that MR images may be corrupted by the geometric distortions (scaling, translation and rotations) due to the patients' movement or by zooming of MR sequence while visualizing. Partial volume artifact, geometric distortion, inter slice gaps, misalignment within image series are the challenges which complicate the segmentation process. These effects are imprinted on image and cannot be easily

visualized leading to faulty reading. Also, during investigation it was found that on MRI, lesions containing protein, calcification, fat and melanin cause hyperintensity on T1-weighted images, occasionally get mistaken for hemorrhage, due to their similar appearance. Differentiation of HI (hemorrhagic infarct) from ICH (Intra cerebral hemorrhage) is another issue of concern which mimic each other. Intracerebral hemorrhage (ICH) sometimes overlaps with a hemorrhagic infarct and hence needs to be distinguished as the line of treatment will then vary. Segmentation ambiguity increases if the lesion is not perfectly clear, i.e. it has fuzzy visibility due to varied reasons like machine or subject developed artifacts, presence of homogeneous lesion isointense near the similar intensity brain parenchyma, presence of edema surrounding lesion near similar background. Furthermore, contouring lesions manually in hundreds of MRI slices demands high attention and patience. It is a laborious task prone to subjective variations.

Based on the experimental results, following conclusions have been drawn at various stages of the present work, which are summarized as below:

Evaluation of the proposed segmentation approach

Most of the segmentation methods used for extracting the boundaries of region or object of interest are active contour-based approaches. Generally, region-based ACM evolution is dependent on global information due to which in presence of intensity inhomogeneity these models fails. Although few variations are presented in literature to incorporate local information empirically in the image, but their demerit is the involvement of complicated procedures resulting to highly time intensive procedures.

The MRBAC segmentation model is developed for delineating the pathological regions which is a variant of LGDF model. Classical LGDF model findings were evaluated on few images and are disputable in certain cases of MRI lesions. It does not fit well when presented with the image where the background and foreground with slight intensity variations or when the object boundaries are very weak. Also, defining the initial contour location was done empirically which is time consuming process and requires extensive manual intervention. The proposed method conserves the merits of traditional technique along with adopting the new feature for contour initialization. It speeds up the whole process as it requires the involvement of technicians or radiologists who can quickly rough mark the boundary, which is a computationally simplistic process. It demands less manual input. So, instead of empirically feeding data (ρ value) for defining the initial contour location, the proposed method directly feeds the rough marking as initial level set and update local intensity information (mean and standard deviation) until convergence. If the change in evolving

contour of the level set function between successive iteration is less than the termination criterion, in our case 0.3, then contour evolution is stopped automatically.

From the objective analysis, it is found that the developed method is closely follows the ground truth demarcated by the radiologist. Experimental results shown in Appendix Table A.1 illustrates that the proposed MRBAC approach in shows significant improvement in terms of averaged segmentation accuracy (ACC) (0.947 ± 0.015 , 0.883 ± 0.037 , 0.922 ± 0.012), Jaccard Similarity Index (JSI) (0.898 ± 0.030 , 0.778 ± 0.070 , 0.853 ± 0.024 and Dice Coefficient (DC) values (0.946 ± 0.017 , 0.873 ± 0.044 , 0.920 ± 0.014) of tumor, infarct and hemorrhage respectively. Appendix Table A.2 illustrates the Region Growing method averaged segmentation ACC (0.933 ± 0.007 , 0.842 ± 0.024 , 0.902 ± 0.015), JSI(0.873 ± 0.011 , 0.705 ± 0.059 , 0.820 ± 0.023) and DC values (0.932 ± 0.006 , 0.825 ± 0.041 , 0.901 ± 0.014) of tumor, infarct and hemorrhage respectively while Appendix Table A.3 illustrates the Distance Regularized Level Set Evolution (DRLSE) approach averaged segmentation ACC method as (0.887 ± 0.062 , 0.854 ± 0.039 , 0.908 ± 0.021), JSI (0.783 ± 0.121 , 0.729 ± 0.065 , 0.826 ± 0.042) and DC (0.873 ± 0.079 , 0.842 ± 0.044 , 0.904 ± 0.025) values of tumor, infarct and hemorrhage respectively. Also, from the experiments performed separately for tumor, infarct and hemorrhage, it has been found that the proposed method takes a dip in case of averaged segmentation FP and HD value than compared with the Region Growing and DRLSE methods. In addition, it takes less time to segment the images than others as given in Appendix Table A.4. Remarkable results are given by MRBAC in segmenting hypointense, hyperintense, isointense-heterogeneous as well as infused lesions having acute concavities and irregular boundaries on T1-weighted and T2-weighted MR images. Thus, it is concluded from these results that the proposed segmentation method outperforms the other state-of-art methods in terms of accurate extraction of object boundaries of interest.

Evaluation of the proposed classification approach:

Lesion ambiguity during classification is affected by hypo to iso intensity patterns, texture patterns and associated edema with them. Further, due to improper visualization, sometimes lesions are misclassified as normal regions (NR) and hence lesion prediction totally depends on expertise and experience of radiologist. ANN classification system is designed and developed for classification model of homogeneous, heterogeneous and diffused pathology for detection of lesions (brain tumors, brain hemorrhage and brain infarct) on routinely acquired T1 and T2-weighted MR images. Classification model is tested on two separate modules: 1st one for two

class classification system and the 2nd one for four class classification system.

For extracting image attributes useful in representation and description, statistical texture features are calculated from the attribute extraction techniques namely IBF, GLCM, SGLDM, GLDS, NGTDM, SFM, Laws TEM, FDTA, FPS, LBP and its variants, four level Gaussian Pyramid based LBP features with Gaussian Pyramid of its variants. In order to remove the redundancy and speed up the whole process, feature selection is done after feature extraction in the present study. For selecting only useful attributes, mRMR feature selection technique is employed in this work. Out of 1861 feature, only the top 500 features were selected after applying mRMR technique. After normalization, selected feature set are presented to proposed Fusion Network, which is an assembly of ten individual networks, each having two-layer feedforward neural network with 6 neurons in hidden layer and 4 neurons in output layer. All Hidden layers uses sigmoid activation function and output layers uses SoftMax activation function. The individual neural networks are trained with scaled conjugate gradient backpropagation method. The accuracy of proposed Fusion Network classifier comes out to be 94.5% and 92.8% for two class classification between normal and pathological brain MRI and multiclass classification between normal, tumor, hemorrhage and infarct brain MRI respectively. The developed classification module is of value to radiologist and neurologist by assisting in decision making and treatment planning.

Thus, in brief, the overall contribution of present work was the development of interactive and efficient model formulation for early and accurate recognition of three most commonly occurring abnormalities, accentuating death incidences.

6.2 Scope for Future Work

Although relevant contributions have been made towards the objectives of segmentation and lesion detection from MRI image, following are some suggestions for future work in this area:

1. The proposed segmentation approach is a region based active contour approach which differs at the initialization stage. This initialization can be adopted to edge base models to analyze the performance of such models.
2. Different initialization techniques may be included like the initialization through FCM method, thresholding techniques and its impact on performance can be studied.
3. Segmentation approach is not fully automatic; efforts can be made in developing the fully automatic system for segmentation of MR image.

4. Different enhancement methods can be applied before feature extraction to obtain highly discriminating features.
5. In order to have a generalized performance of the system, the system can be tested on more pathologies with bigger datasets acquired from different MRI centers to include medical variety (variance in sex, age, compliance, anamnestic data etc.) in the clinical studies.
6. This study has not touched areas like disease severity, distinction between damage and progressive anomalies. Further work in these areas can be suggested.
7. Due to non-availability of 3D datasets, the proposed method is developed for 2D datasets. In future 3D modelling for lesion detection can be done. However, data collection may take a lot of time.

PUBLICATIONS FROM THE RESEARCH WORK

Journal Papers

1. Sweta Tripathi, R.S. Anand and E. Fernandez, " Classification of Normal and Abnormal Brain in MR Images, " *International Journal of Emerging Technologies and Innovative Research*, Vol.5, Issue 5, page no. 610-614, MAY 2018 (published).
2. Sweta Tripathi, R.S. Anand and E. Fernandez," A Review of Brain MR Image Segmentation Techniques," *International Journal of Research and Analytical Reviews (IJRAR)* (accepted for publication through conference).
3. Sweta Tripathi, R.S. Anand and E. Fernandez," Lesions Stratification Framework by Segmentation and Classification of Brain MR Image," *Future Computing and Informatics Journal (Elsevier)*, 2018. (under review).

Conference Papers

1. Sweta Tripathi, R.S. Anand and E. Fernandez," A Review of Brain MR Image Segmentation Techniques", *International Conference on Recent Innovations in Applied Science, Engineering & Technology (AET-2018)*, pp162-169, 16th-17th June 2018.
2. Sweta Tripathi, R.S. Anand and E. Fernandez, "Segmentation of Brain Lesions in MR Images", *International Conference on Recent Innovations in Electrical, Electronics & Communication Engineering - (ICRIEECE)* July 27th & 28th 2018 (IEEE conference)

REFERENCES

- [1] T. D. Nielsen, "Survey of 1000 cases of apoplexia cerebri," *Acta psychiatrica neurologica scandinavica*, vol. 30, p. 169, 1956.
- [2] M. J. Harrison., "Clinical distinction of cerebral haemorrhage and cerebral infarction," *Postgraduate Medical Journal*, vol. 56, pp. 629-632, 1980.
- [3] C. C. Chen, P. H. Chapman, H. Kooy and J. S. Loeffler, "Neuroimaging in Radiosurgery Treatment Planning and Follow-up Evaluation," *Principles and Practice of Stereotactic Radiosurgery* , pp. 9-23, 2008.
- [4] S. Gilman, "Imaging the brain," *The New England Journal of Medicine*, vol. 338, no. 12, pp. 812-820, 1998.
- [5] M. Symms, H. Jager, K. Schmierer and T. Yousry, "A review of structural magnetic resonance neuroimaging," *Journal of Neurology and Neurosurgery Psychiatry*, vol. 75, no. 9, p. 1235–1244, September 2004 .
- [6] <http://www.e-radiography.net/mrict/fund%20mr1/MRI%20fund1.htm>
- [7] A. G. Osborn, "Diagnostic Neuroradiology," *St Louis Mosby Yearbook*, pp. 584-603, 1994.
- [8] G. S. Young, "Advance MRI of adult brain tumors," *Neurological Clinics*, vol. 25, pp. 947-73, 2007
- [9] O. Adeoye and J. Broderick, "Advances in the management of intracerebral hemorrhage," *Nature Reviews Neurology*, vol. 6, no. 11, pp. 593-601, Nov 2010.
- [10] M. R. Patel, R. R. Edelman and S. Warach, "Detection of Hyperacute Primary Intraparenchymal Hemorrhage by Magnetic Resonance Imaging," *Stroke*, vol. 27, no. 12, pp. 2321-2324, December 1996.
- [11] S. Satoh and S. Kadoya, "Magnetic resonance imaging of subarachnoid hemorrhage," *Neuroradiology*, vol. 30, no. 5, pp. 361-366, November 1988.
- [12] E. E. Smith, J. Rosand and S. Greenberg, "Hemorrhagic Stroke," *Neuroimaging Clin N AM*, vol. 15, no. 2, pp. 259-72, 2005.
- [13] D. W. Chakeres and R. N. Bryan, "Acute subarachnoid hemorrhage: in vitro comparison of magnetic resonance and computed tomography," *AJNR Am J Neuroradio*, vol. 7, no. 2, pp. 223-8, 1986.
- [14] A. L. Romanova, A. J. Nemeth, M. D. Berman, J. C. Guth, E. M. Liotta, A. M. Naidech and M. B. Maas, "MRI versus CT for identification and quantification of intraventricular haemorrhage", *J Stroke Cerebrovasc*, vol. 23, no. 8, pp. 2036-2040, 2014.

-
- [15] J. S. Whang, M. Kolber, D. K. Powell and E. Libfeld, "Diffusion-weighted signal patterns of intracranial haemorrhage," *Clin Radiol*, vol. 70, no. 8, pp. 909-916, 2015.
- [16] J. Hodel, R. Aboukais, B. Dutouquet, E. Kalsoum, M. A. Benadjaoud, D. Chechin, M. Zins, A. Rahmouni, A. Luciani, J. P. Pruvo, J. P. Lejeune and X. Leclerc, "Double Inversion Recovery MR Sequence for the Detection of Subacute Subarachnoid Hemorrhage," *American Journal of Neuroradiology*, vol. 36, no. 2, pp. 251-258, 2015.
- [17] S. Oda, M. Shimoda, A. Hirayama, M. Imai, F. Komatsu, H. Shigematsu, J. Nishiyama, K. Hotta and M. Matsumae, "Retrospective review of previous minor leak before major subarachnoid hemorrhage diagnosed by MRI as a predictor of occurrence of symptomatic delayed cerebral ischemia," *J Neurosurg*, vol. 128, no. 2, pp. 499-505, February 2017.
- [18] W. Bradley, "Hemorrhage and brain iron," *Magnetic Resonance Imaging 2nd ed. Mosby*, pp. 721-769, 1992.
- [19] M. Wintermark, P. Maeder, M. Reichhart, P. Schnyder, J. Bogousslavsky and R. Meuli, "MR pattern of hyperacute cerebral hemorrhage," *J Magn Reson Imaging*, vol. 15, no. 6, pp. 705-709, June 2002.
- [20] G. Korbakis, S. Prabhakaran, S. John, R. Garg, J. J. Conners, T. P. Bleck and V. H. Lee, "MRI Detection of Cerebral Infarction in Subarachnoid Hemorrhage," *Neurocrit Care*, vol. 24, no. 3, pp. 428-435, 2016.
- [21] B. Lanzman and J. J. Heit, "Advanced MRI Measures of Cerebral Perfusion and Their Clinical Applications," *Top Magn Reson Imaging*, vol. 26, no. 2, pp. 83-90, April 2017.
- [22] T. Ebisu, S. Naruse, Y. Horikawa, C. Tanaka and T. Higuchi, "Nonacute subdural hematoma fundamental interpretation of MR images based on biochemical and in vitro MR analysis," *Radiology*, vol. 170, no. 2, pp. 449-453, 1989.
- [23] E. S. Fobben, R. I. Grossman, S. W. Atlas, D. B. Hackney, H. I. Goldberg, R. A. Zimmerman and L. T. Bilaniuk, "MR characteristics of subdural hematomas and hygromas at 1.5 T," *AJR Am J Roe*, vol. 153, no. 3, pp. 589-595, 1989.
- [24] I. Linfante, R. Llinas, L. Caplan and S. Warach, "MRI features of intracerebral hemorrhage within 2 hours from symptom onset," *Stroke*, vol. 30, no. 11, pp. 2263-2267, November 1999.
- [25] D. M. Mandell, M. M. Basha, Y. Qiao, C. P. Hess, F. Hui, C. Matouk, M. H. Johnson, M. J. A. P. Daemen, A. Vossough, M. Edjlali, D. Saloner, S. A. Ansari, B. A. Wasserman and D. J. Mikulis, "Intracranial Vessel Wall MRI Principles and Expert Consensus Recommendations of the American Society of Neuroradiology," *American Journal of Neuroradiology*, pp. 1-12, July 2016.

-
- [26] Srinivasan, M. Goyal, F. A. Azri and C. Lum, "State-of-the-Art Imaging of Acute Stroke," *Radiographics*, vol. 26, no. 1, pp. 75-95, 1 October 2006.
- [27] L. Allen, A. Hasso, J. Handwerker and H. Farid, "Sequence-specific MR imaging findings that are useful in dating ischemic stroke," *Radiographics*, vol. 32, no. 5, pp. 1285-1297, Sep-Oct 2012.
- [28] P. M. C. Choi, J. V. Ly, V. Srikanth, H. Ma, W. Chong, M. Holt and T. G. Phan, "Differentiating between Hemorrhagic Infarct and Parenchymal Intracerebral Hemorrhage," *Radiology Research and Practice*, 2012.
- [29] J. Bogousslavsky, F. Regli, A. Uske, and P. Maeder, "Early spontaneous hematoma in cerebral infarct: is primary cerebral hemorrhage overdiagnosed?," *Neurology*, vol. 41, no. 6, pp. 837-840, 1991
- [30] R. N. Al-Okaili, J. Krejza, S. Wang, J. H. Woo and E. R. Melhem, "Advanced MR Imaging Techniques in the Diagnosis of Intraaxial Brain Tumors in Adults," *RadioGraphics*, vol. 26, pp. 173-189, 1 Oct 2006.
- [31] M. W. Vernooij, M. A. Ikram, H. L. Tanghe, A. J. Vincent, A. Hofman, G. P. Krestin, W. J. Niessen, M. M. Breteler and A. v. d. Lugt, "Incidental Findings on Brain MRI in the General Population," *The New England Journal of Medicine*, vol. 357, pp. 1821-1828, 2007.
- [32] A. Raslan and A. Bhardwaj, "Medical management of cerebral edema," *Neurosurgical Focus*, vol. 22, no. 5, pp. 1-12, 2007.
- [33] M. Jafari and S. Kasaei, "Automatic Brain Tissue Detection in MRI Images Using Seeded Region Growing," *Australian Journal of Basic and Applied Sciences*, vol. 8, pp. 1066-1079, 2011.
- [34] K. Xie, J. Yang, Z. Zhang and Y. Zhu, "Semi-automated brain tumor and edema segmentation using MRI," *Eur J Radiol*, vol. 56, no. 1, pp. 12-19, Oct 2005.
- [35] J. Luts, A. Heerschap, J. A. Suykens and S. V. Huffel, "A combined MRI and MRSI based multiclass system for brain tumour recognition using LS-SVMs with class probabilities and feature selection," *Artificial intelligence in Medicine*, vol. 40, no. 2, pp. 87-102, 2007.
- [36] M. Weber, S. Zoubaa, M. Schlieter, E. Jüttler, H. Huttner, K. Geletneky, C. Ittrich, M. Lichy, A. Kroll, J. Debus, F. Giesel, M. Hartmann and M. Essig, "Diagnostic performance of spectroscopic and perfusion MRI for distinction of brain tumors.," *Neurology*, vol. 66, no. 12, pp. 1899-1906, 2006.

-
- [37] P. Dhawan, H. K. Huang and D. Kim, "Principles and Advanced Methods in Medical Imaging and Image Analysis," *World Scientific. Singapore*, 2008.
- [38] A. Jain, R. Duin and J. Mao, "Statistical pattern recognition: a review," *IEEE Transactions on Pattern Analysis and Machine Intelligence*, vol. 22, no. 1, pp. 4-37, 2000.
- [39] R. M. Haralick, K. Shanmugam and I. Dinstein, "Textural features of image classification," *IEEE Transactions on Systems, Man and Cybernetics*, vol. 3, no. 6, pp. 610-621, 1973.
- [40] G. Castellano, L. Bonilha, L.M. Li and F. Cendes, "Texture analysis of medical images," *Clinical Radiology*, vol 59, pp. 1061–1069, 2004
- [41] M. E. Algorri and F. Flores-Mangas, "Classification of anatomical structures in mr brain images using fuzzy parameters," *IEEE Transactions on Biomedical Engineering*, vol. 51, no. 9, pp. 1599-1608, 2004.
- [42] K. V. Leemput, F. Maes, D. Vandermeulen and P. Suetens, "Automated model-based tissue classification of MR images of the brain," *IEEE Transactions on Biomedical Engineering*, vol 18, no. 10, pp. 897-908, 1999.
- [43] H. S. Zadeh and H.S. Windham, "A comparative analysis of several transformations for enhancement and segmentation of magnetic resonance image scene sequences," *IEEE Transactions on medical Engineering*, vol. N3, no. 10, pp. 302-318, 1992.
- [44] H. S. Zadeh and H.S. Windham, "Optimal Linier transformation for MRI feature extraction," *IEEE Transactions on medical Engineering*, vol. 15, pp. 749-767, 1996.
- [45] V. chen and S. Ruan, "Graph cut based segmentation of brain tumors from MR images," *International Journal on Sciences and Techniques of Automatic Control & Computer Engineering*, vol. 3, pp. 1054-1063, 2 December 2009.
- [46] W. Deng, W. Xiao, H. Deng and J. Liu, "MRI brain tumor segmentation with region growing method based on the gradients and variances along and inside of the boundary curve," *3rd International Conference on Biomedical Engineering and Informatics (BMEI)*, pp. 393-396, 2010.
- [47] J. S. Suri, "Two dimensional fast magnetic resonance brain segmentation," *IEEE Engineering in Medicine and Biology Magazine*, vol. 20, no. 4, pp. 84-95, 2001.
- [48] A.S. Capelle, C. F. Maloigne and O. Colot, "Segmentation of brain tumors by evidence theory: on the use of the conflict information," In *proceedings: Seventh International Conference on Information fusion, Stockholm, Sweden*, pp. 264-271, 2004.
- [49] T Lie, X Jia, Y Zhang, L He, H Meng and A K Nandi, "Significantly fast and robust fuzzy C-means clustering algorithm based on morphological reconstruction and

- membership filtering”, *IEEE Transactions on fuzzy systems*, vol.26, no.5, pp.3027-3041, 2018.
- [50] T Lei, X Jia, Y Zhang, S Liu, H Meng and A K Nandi, “ Superpixel-based fast fuzzy C-means clustering for color image segmentation”, *IEEE Transactions on fuzzy systems*, DOI: 10.1109/TFUZZ.2018.2889018,2018.
- [51] L. M. Fletcher-Heath, L. O. Hall, D. B. Goldgof and F. R. Murtagh, “Automatic segmentation of Non-enhancing Brain tumor in magnetic resonance images,” *Artificial intelligence in medicine*, vol.21, pp. 43-63, 2001.
- [52] S. Dickson, B. T. Thomas and P. Goddard, "Using Neural Networks to Automatically Detect Brain Tumours in MR Images," *International Journal of Neural Systems*, vol. 8, no. 1, February 1997.
- [53] Y. Zhu and Z. Yan, "Computerized tumor boundary detection using a hopfield neural network," *IEEE Transactions on Medical Imaging*, vol. 16, no. 1, pp. 55-67, 1997.
- [54] 54. M. M. Letteboer, O. F. Olsen, E. B. Dam, P. W. A. Willems, M. A. Yicrgever and W. J. Niessen, “Segmentation of tumors in magnetic resonance using an interactive multiscale watershed algorithm,” *Academic Radiology*, vol, 10, no.11, pp. 1125-1138, 2004.
- [55] M. Mancas and B. Gosselin, "Iterative watersheds and fuzzy tumor visualization,," in *In Proceedings: Fourteenth IEEE Visualization*, pp.81-83, 2003.
- [56] M. B. Cuadra, C. Pollo, A. Bardera, O. Cuisenaire, J. G. Villemure and J. P. Thiran, "Atlas-based segmentation of pathological brains using a model of lesion growth," *IEEE Transactions on Medical Imaging*, vol. 23, no. 10, pp. 1301-1314, 2004.
- [57] M. Prastawa, E. Bullitt, S. Ho and G. Gerig, "A brain tumor segmentation framework based on outlier detection," *Medical Image Analysis*, vol. 8, no. 3, pp. 275-283, Sep 2004.
- [58] M. H. F. Zarandia, M. Zarinbala and M. Izadib, "Systematic image processing for diagnosing brain tumors: A Type-II Fuzzy Expert System Approach," *Applied Soft Computing*, vol. 11, no. 1, pp. 285-294, January 2011.
- [59] J. Liu, J. K. Udupa, D. Odhner, D. Hackney, G. Moonis, "A system for brain tumor volume estimation via MR imaging and fuzzy connectedness," *Computerized Medical Imaging and Graphics*, vol. 29, no. 1, pp. 21-34, 2005.

-
- [60] M. W. Grohman and P. A. Dhawan, "Fuzzy convex set-based pattern classification for analysis of mammographic micro calcifications," *Pattern Recognition*, vol. 34, pp.469-1482, 2001.
- [61] G. P. Mazzara, R. P. Velthuisen, J. L. Pearlman, H. M. Greenberg and H. Wagner, "Brain tumor target volume determination for radiation treatment planning through automated MRI segmentation," *International Journal of Radiation, Oncology, Biology and Physics*, vol. 59, no. 1, pp. 300-312,2004.
- [62] R. A. Lerski, K. Straughan and L. R. Schad, "MR Image texture analysis: An approach to tissue characterization," *Magnetic Resonance Imaging*, vol. II, pp. 873-887, 1993.
- [63] D. Mahmoud-Ghoneim, G. Toussaint, J. M. Constans and J. D. de Certaines, " Three dimensional texture analysis in MRI: A preliminary evaluation in Gliomas," *Magnetic Resonance Imaging*, vol. 21, no. 9, pp. 983-987,2003.
- [64] C. Pachai, Y. M. Zhu, J. Grimaud, M. Hermier, A. Drornigny-Badin, A. Boudraa, G. Gimenez, C. Confavreux and J. C. Froment," A pyramidal approach for automatic segmentation of multiple sclerosis lesions in brain MRI," *Computerized Medical Imaging and Graphics*, vol, 22, no. 5, pp. 399-408, 1998.
- [65] A. Pitiot, A. W. Toga, N. Ayache and P. Thompson, "Texture based MRI segmentation with a two-stage hybrid neural classifier," *International Joint Conference on Neural Networks*, vol. 3. pp. 2053-2058, 2002.
- [66] N. Sarkar and B. B. Chaudhuri, "An efficient approach to estimate fractal dimension of textural images," *Pattern Recognition*, vol. 25, no. 9, pp. 1035-1041, 1992.
- [67] A. Bru, J. M. Pastor, I. Fernaud, I. Bru, S. Melle and C. Berenguer, "Super-rough dynamics on tumor growth," *Physical Review Letters*, vol. 81, no.18, pp. 4008-4011, 1998.
- [68] K. M. Iftkharuddin, W. Jia and R. Marsh, "Fractal analysis of tumor in brain MR images," *Machine Vision and Applications*, vol. 13, no. 5-6, pp. 352-362, 2003.
- [69] J. M. Zook and K. M. Iftkharuddin, "Statistical analysis of fractal-based brain tumor detection algorithms," *Magnetic Resonance Imaging*, vol. 23, pp. 671-678, 2005.
- [70] R. M. Rangayyan, I. Kamenetsky, H. Benediktsson, "Segmentation and analysis of the glomerular basement membrane in renal biopsy samples using active contours: a pilot study," *Journal of Digital Imaging*, vol. 23, no. 3, pp. 323-331, 2010.
- [71] T. Chaira and S. Anand, "A novel intuitionistic fuzzy approach for tumour/ hemorrhage detection in medical images," *Journal of Scientific and Industrial Research*, vol. 70, pp. 427-434, 2011.

-
- [72] N. Joshi, R. Srikanth and A. G. Ramakrishnan, "Model based Bayesian approach for MR image segmentation," in *In proceedings: Fifth International Conference on Advances in Pattern Recognition*, pp. 331-335, 2003.
- [73] A. Kumar and S. Gupta, "Content based video object segmentation and tracking using a novel probabilistic approach for low bit rate applications," in *IEEE International Conference on Multimedia and Expo (ICME 2001)*, pp. 904-907, 2001.
- [74] V. Caselles, R. Kimmel, and G. Sapiro, "Geodesic active contours," *International Journal of Computer Vision*, vol. 22, no. 1, pp. 61-79, 1997.
- [75] J. Prince and C. Xu, "Snakes, shapes, and gradient vector flow," *IEEE Transactions on Image Processing*, vol. 7, no. 3, pp. 359 - 369, March 1998.
- [76] T. Wang, I. Cheng and A. Basu, "Fluid vector flow and application in brain tumor segmentation," *IEEE Transactions on Biomedical Engineering*, vol. 56, no. 3, pp. 781-789, 2009.
- [77] X. Xie and M. Mirmehdi, "MAC: Magnetostatic Active Contour Model," *IEEE Transactions on Pattern Analysis and Machine Intelligence*, vol. 30, no. 4, pp. 632-646, 2008.
- [78] S. P. Dakua and J. S. Sahambi, "Weighting function in random walk based left ventricle segmentation," *In Proceedings: Eighteenth IEEE International Conference on Image Processing*, vol. 48, no. 1, pp. 2133-2136, 2011.
- [79] S. Kaur and J.S. Sahambi, "Curvelet initialized level set cell segmentation for touching cells in low contrast images," *Computerized medical imaging and graphics* vol. 49, pp. 46-57, 2016.
- [80] R. Malladi, J. Sethian and B. Vemuri, "Shape modeling with front propagation: a level set approach," *IEEE Transactions on Pattern analysis and machine Intelligence*, vol. 17, no. 2, pp. 158-175, 1995.
- [81] O. Gloger, M. Ehrhardt, T. Dietrich, O. Hellwich, K. Graf and E. Nagel, "A three stepped coordinated level set segmentation method for identifying atherosclerotic plaques on MR-images," *Communications in Numerical Methods in Engineering*, vol. 25, no. 6, pp. 615-638, 2009.
- [82] N. R. Pal and S. K. Pal, "A review on image segmentation techniques," *Pattern Recognition*, vol. 26, no. 9, pp. 1277-1294, 1993.
- [83] R. C. Gonzalez and R. E. Woods, *Digital Image Processing*, Prentice-Hall India, 2001.
- [84] S. R. Vantaram and E. Saber, "Survey of contemporary trends in color image segmentation," *Journal of Electronic Imaging*, vol. 21, no. 4, pp. 1-28, 2012.

-
- [85] A. Devos, A. W. Simonetti, M.V. Graaf, L. Lukas, J. A. Suykens, L. Vanhamme, L. M. Buydens, A. Heerschap and H. S. Van, "The use of multivariate MR imaging intensities versus metabolic data from MR spectroscopic imaging for brain tumour classification," *Journal of Magnetic Resonance*, vol. 173, no. 2, pp. 218-228, 2005.
- [86] D. L. Pham and J. L. Prince, "An adaptive fuzzy C-means algorithm for image segmentation in the presence of intensity inhomogeneities," *Pattern Recognition Letters*, vol. 20, no. 1, pp. 57-68, 1999.
- [87] M. N. Ahmed, S. M. Yamany, N. Mohamed, A. A. Farag and T. Moriarty, "A modified fuzzy c-means algorithm for bias field estimation and segmentation of MRI data," *IEEE Transactions on Medical Imaging*, vol. 21, no. 3, pp. 193-199, 2002.
- [88] Songcan and Z. Daoqiang, "Robust image segmentation using FCM with spatial constraints based on new kernel-induced distance measure," *IEEE Transactions on Systems, Man, and Cybernetics*, vol. 34, pp. 1907-1916, 2004.
- [89] M. S. Yang and H. S. Tsai, "A Gaussian kernel-based fuzzy c-means algorithm with a spatial bias correction," *Pattern Recognition Letters*, vol. 29, no. 12, pp. 1713-1725, 2008.
- [90] J. Kang, L. Min, Q. Luan, X. Li and J. Liu, "Novel modified fuzzy c-means algorithm with applications," *Digital Signal Processing*, vol. 19, no. 2, pp. 309-319, 2009.
- [91] S. Krinidis and V. Chatzis, "A Robust Fuzzy Local Information C-Means Clustering Algorithm," *IEEE Transactions on Image Processing*, vol. 19, no. 5, pp. 1328-1337, 2010.
- [92] M. Hassan, A. Chaudhry, A. Khan and J. Y. Kim, "Carotid artery image segmentation using modified spatial fuzzy c-means and ensemble clustering," *Computer Methods and Programs in Biomedicine*, vol. 108, no. 3, pp. 1261-1276, 2012.
- [93] S. R. Kannan, A. Sathya, S. Ramathilagam and R. Devi, "Novel segmentation algorithm in segmenting medical images," *Journal of Systems and Software*, vol. 83, no. 12, pp. 2487-2495, December 2010.
- [94] L. Chen, C. L. P. Chen and M. Lu, "A multiple-kernel fuzzy C-means algorithm for image segmentation," *IEEE Transactions on Systems, Man, and Cybernetics, Part B: Cybernetics*, vol. 41, no. 5, pp. 1263-1274, 2011.
- [95] Y. Prasad and K. K. Biswas, "Fuzzy rough based regularization in Generalized Multiple Kernel Learning," *Computers & Mathematics with Applications*, vol. 66, no. 10, pp. 1770-1781, 2013.

-
- [96] D. Yang, L. Wang., X. Hei and M. Gong, "An efficient automatic SAR image segmentation framework in AIS using kernel clustering index and histogram statistics," *Applied Soft Computing*, vol. 16, pp. 63-79, March 2014.
- [97] J. R. Beveridge, J. Griffith, R. R. Kohler, A. R. Hanson and E. M. Riseman, "Segmenting images using localized histograms and region merging," *International Journal of Computer Vision*, vol. 2, no. 3, pp. 311-347, January 1989.
- [98] F. Calderero and F. Marques, "Region merging techniques using information theory statistical measures," *IEEE Transactions on Image Processing*, vol. 19, no. 6, pp. 1567 - 1586, 2010.
- [99] A. R. Abdel-Dayem, and M. R. El-Sakka, "Carotid artery ultrasound image segmentation using fuzzy region growing," *Image Analysis and Recognition*, vol. 3656, pp. 869-878, 2005.
- [100] L. Bischof and R. Adams, "Seeded region growing," *IEEE Transactions on Pattern Analysis and Machine Intelligence*, vol. 16, no. 6, pp. 641 - 647, June 1994.
- [101] J. Fan, D. K. Y. Yau, A. K. Elmagarmid and W. G. Aref, "Automatic image segmentation by integrating color-edge extraction and seeded region growing," *IEEE Transactions on Image Processing*, vol. 10, no. 10, pp. 1454-1466, 2001.
- [102] J. Fan, G. Zeng, M. Body and M.-S. Hacid, "Seeded region growing: an extensive and comparative study," *Pattern Recognition Letters*, vol. 26, no. 8, pp. 1139-1156, June 2005.
- [103] A. Thakur and R. S. Anand, "A local statistics based region growing segmentation method for ultrasound medical images," *International Journal of Signal Processing*, vol. 1, no. 2, pp. 141-146, 2004.
- [104] P. K. Jain and S. Susan, "An adaptive single seed based region growing algorithm for color image segmentation," *Annual IEEE India Conference (INDICON)*, 2013
- [105] S. Beucher and MF. Meyer, "The morphological approach to segmentation: the watershed transformation," *Optical Engineering*, vol. 34, pp. 433-433, December 1992.
- [106] Y. L., Huang and D. R. Chen, "Watershed segmentation for breast tumor in 2-D sonography," *Ultrasound in Medicine & Biology*, vol. 30, no. 5, pp. 625-632, 2004.
- [107] K. Haris, S.N. Efstratiadis, N. Magiaveras, and O. Pappas, "Hybrid image segmentation using watersheds," in *Proceedings: Visual Communications and Image Processing*. pp. 1140-1151. 1996.

-
- [108] K. Haris, S. Efstratiadis, N. Maglaveras and A. Katsaggelos, "Hybrid image segmentation using watersheds and fast region merging," *IEEE Transactions on Image Processing Issue*, vol. 7, no. 12, pp. 1684 - 1699, Dec 1998.
- [109] R.S. Sengar, A.K. Upadhyay, M. Singh and V.M. Gadre, "Segmentation of two dimensional electrophoresis gel image using the wavelet transform and the watershed transform," in *Proceedings: IEEE National Conference on Communications*, pp. 1-5, 2012.
- [110] R. S. Sengar, A. K. Upadhyaya, M. Singh and V. M. Gadre, "Analysis of 2D-gel images for detection of protein spots using a novel non-separable wavelet based method," *Biomedical Signal Processing and Control*, vol. 25, pp. 62-75, March 2016.
- [111] V. Shrimali, R. S. Anand and V. Kumar, "Current Trends in Segmentation of Medical Ultrasound B-mode Images: A Review," *IETE Technical Review*, vol. 26, no. 1, pp. 8-17, 2009.
- [112] Y. Zhang, S. Wu, G. Yu, and D. Wang, "A hybrid image segmentation approach using watershed transform and FCM," In *Proceedings: 4th International Conference on Fuzzy Systems and Knowledge Discovery*, pp. 2-6, 2007.
- [113] M. Kass, A. Witkin and D. Terzopoulos, "Snakes: active contour model," *International Journal of Computer Vision*, vol. 1, no. 4, pp. 321-331, 1988.
- [114] S. Osher and J. A. Sethian, "Fronts propagating with curvature-dependent speed: Algorithms based on Hamilton-Jacobi formulations," *Journal of Computational Physics*, vol. 79, no. 1, pp. 12-49, 1988.
- [115] L. Gong, L. Ng, S. D. Pathak, I. Tutar, P. S. Cho, D. R. Haynor and Y. Kim, "Prostate ultrasound image segmentation using level set-based region flow with shape guidance," in *In Proceedings: Medical Imaging*, pp. 1648-1657, 2005.
- [116] M. Seera, M. L. D. Wong and A. K. Nandi, "Classification of ball bearing faults using a hybrid intelligent model," *Applied Soft Computing*, vol.57, pp. 427-435, 2017.
- [117] N. Paragios and R. Deriche, "Geodesic active contours and level sets for the detection and tracking of moving objects," *IEEE Transactions on Pattern Analysis and Machine Intelligence*, vol. 22, no. 3, pp. 266-280, 2000.
- [118] M. Weber, A. Blake and R. Cipolla, "Sparse finite elements for geodesic contours with level-sets," in *T. Pajdla and J. Matas, J.(eds) Computer Vision, ed: Springer Berlin Heidelberg*, vol. 3022, pp. 391-404, 2004.

-
- [119] L. Chunming, X. Chenyang, G. Changfeng and M.D. Fox, "Level set evolution without re-initialization: a new variational formulation," In *Proceedings: IEEE Conference on Computer Vision and Pattern Recognition*, vol. 1, pp. 430-436, 2005.
- [120] D. Peng, B. Merriman, S. Osher, H. Zhao and M. Kang, "A PDE-based fast local level set method," *Journal of Computational Physics*, vol. 155, no. 2, pp. 410-438, 1999.
- [121] S. Osher and R. Fedkiw, "Level set methods and dynamic Implicit surfaces," *Springer Verlag. New York*, 2003.
- [122] J.A. Sethian, "Level Set Methods and Fast Marching Methods", *Cambridge University Press. UK*. 1999.
- [123] L. Chunming, X. Chenyang, G. Changfeng and M.D. Fox, "Distance regularized level set evolution and its application to image segmentation," *IEEE Transactions on Image Processing*, vol. 19, no. 12, pp. 3243-3254, 2010.
- [124] T.F. Chan and L.A. Vese, "Active contours without edges," *IEEE Transactions on Image Processing*, vol. 10, no. 2, pp. 266-277, 2001.
- [125] D. Mumford and J. Shah, "Optimal approximations by piecewise smooth functions and associated variational problems," *Communications on Pure and Applied Mathematics*, vol. 42. no. 5, pp. 577-685, 1989.
- [126] X. Renbo, L. W.BINH., Jibin. and I. Lun, "An optimal initialization technique for improving the segmentation performance at Chan-Mesa model," in *Proceedings: IEEE international Conference on Automation and Logistics*. pp. 411-415, 2007.
- [127] J.E. Solem., NC. Overgaard and A. Hayden, "Initialization techniques for segmentation with the Chan-Vase model," In *Proceedings: 18th international Conference on Pattern Recognition*, pp. 171-174. 2006.
- [128] L. Vese and T. Chan, "A multiphase level set framework for image segmentation using the Mumford and Shah model," *International Journal of Computer Vision*, vol. 50, no. 3, pp. 271-293, 2002.
- [129] Y. Shi and W. C. Karl, "A fast level set method without solving PDEs," in *In Proceedings: IEEE International Conference on Acoustics, Speech, and Signal Processing*, pp. 97-100, 2005.
- [130] P. Yongsheng, J.D. Birdwell and S.M. Djouadi, "Efficient implementation of the Chan-Vese models without solving PDEs," In *Proceedings: IEEE 8th Workshop on Multimedia Signal Processing*, pp. 350-354, 2006.

-
- [131] Li, C.-Y. Kao, J. C. Gore and Z. Ding, "Minimization of Region-Scalable Fitting Energy for Image Segmentation," *IEEE Transactions on Image Processing*, vol. 17, no. 10, pp. 1940-1949, October 2008.
- [132] Y. Tian, F. Duan, M. Zhou and Z. Wu, "Active contour model combining region and edge information," *Machine Vision and Applications*, vol. 24, no. 1, pp. 47-61, 2013.
- [133] J. Yuan, "Active contour driven by region-scalable fitting and local Bhattacharyya distance energies for ultrasound image segmentation," *IET Image Processing*, vol. 6, no. 8, pp. 1075-1083, 2012.
- [134] K. Zhang, H. Song. and L. Zhang, "Active contours driven by local image fitting energy," *Pattern Recognition*. vol. 43, no. 4. pp. 1199-1206. 2010.
- [135] X Shan, X Gong and A K Nandi, "Active contour model based on local intensity fitting energy for image segmentation and bias estimation", *IEEE Access*, DOI:10.1109/ACCESS.2018.2863719, vol.6, no.1, pp.49817-49827, 2018.
- [136] K. Zhang, L. Zhang, H. Song and W. Zhou, "Active contours with selective local or global segmentation: A new formulation and level set method," *Image and Vision Computing*, vol. 28, no. 4. pp. 668-676, 2010.
- [137] P. F. Felzenszwalb and D. P. Huttenlocher, "Efficient graph-based image segmentation," *International Journal of Computer Vision*, vol. 59, no. 2, pp. 167-181, 2004.
- [138] B. Peng, L. Zhang and D. Zhang, "A survey of graph theoretical approaches to image segmentation," *Pattern Recognition*, vol. 46, no. 3, pp. 1020-1038, 2013.
- [139] T. M. Nguyen and Q. M. J. Wu, "Fast and Robust Spatially Constrained Gaussian Mixture Model for Image Segmentation", *IEEE Transactions on Circuits and Systems for Video Technology*, vol. 23, no. 4, pp. 621 – 635, April 2013
- [140] A. Ajaz, B. Aliahmad and D. Kumar, "A novel method for segmentation of infrared scanning laser ophthalmoscope (IR-SLO) images of retina," *Proceedings of the 39th Annual International Conference of the Engineering in Medicine and Biology Society (EMBC 2017)*, Jeju Island, South Korea, 11-15 July 2017.
- [141] S. Mishra, D. Devendra, S. Chatterjee and M. H. Kolekar, "An efficient GMM and active contour based unsupervised person re-identification," *Int. Conf. on Advances in Computing, Communications and Informatics*, 2017.
- [142] P. A. Yushkevich and G. Gerig, "ITK-SNAP: An Intractive Medical Image Segmentation Tool to Meet the Need for Expert-Guided Segmentation of Complex Medical Images," *IEEE Pulse*, vol. 8, no. 4, pp. 54-57, July-Aug. 2017.

-
- [143] J. C. Bezdek, L. O. Hall and L. P. Clarke, "Review of MR image segmentation techniques using pattern recognition," *Medical Physics*, vol. 20, no. 4, pp. 1033-1048, 1993.
- [144] M. Just and M. Thelen, "Tissue characterization with T1, T2 and proton density values: results in 160 patients with brain tumors," *Radiology*, vol. 169, no. 3, pp. 779-785, 1988.
- [145] D. Wang and D. M. Doddrell, "A segmentation-based partial volume compensated method for an accurate measurement of lateral ventricular volumes on T1-weighted magnetic resonance images," *Magnetic Resonance Imaging*, vol. 19, pp. 267-272, 2001.
- [146] X. Zeng, L. H. Staib, R. T. Schultz and J. S. Duncan, "Segmentation and measurement of the cortex from 3-D MR images using coupled surfaces propagation," *IEEE Transactions on Medical Imaging*, vol. 18, no. 10, pp. 927 - 937, 1999.
- [147] H. Sharma, N. Zerbe, D. Heim, S. Wienert, S. Lohmann, O. Hellwich and P. Hufnagl, "Cell nuclei attributed relational graphs for efficient representation and classification of gastric cancer in digital histopathology," *Proc. SPIE 9791, Medical Imaging*, vol. 9791, pp. 1-19, 2016.
- [148] G. D. Tourassi, "Journey towards computer aided diagnosis: Role of image texture analysis: Role of Image texture analysis," *Radiology*, vol. 213, no. 2, pp. 317-320, 1999.
- [149] A. Materka and M. Strzelecki, "Texture analysis methods-review," *COST B II report, Technical University of Lodz, Institute of Electronics, Brussels*, 1998.
- [150] S. Poonguzhali, B. Deepalakshmi and G. Ravindran, "Optimal Feature Selection and Automatic Classification of Abnormal Masses in Ultrasound Liver Images," in *International Conference on Signal Processing, Communications and Networking*, Chennai India, pp. 503-506, 2007.
- [151] C. M. Wu, Y. C. Chen and K. S. Hsieh, "Texture feature for classification of ultrasonic liver images," *IEEE Transactions on Medical Imaging*, vol. 11, no. 2, pp. 141-152, 1992.
- [152] S. Arivazhagan and L. Ganesan, "Texture classification using wavelet transform," *Pattern Recognition Letters*, vol. 24, no. 9-10, pp. 1513-1521, 2003.
- [153] S. Chatterjee and M. H. Kolekar, "Feature extraction and segmentation techniques in static hand gesture recognition system", book chapter of book on Hybrid Intelligence for Image Analysis and Understanding, John Wiley Publication, UK, 2017
- [154] V. González-Castro, M. C. V. Hernández, P. A. Armitage and J. M. Wardlaw, "Texture-based Classification for the Automatic Rating of the Perivascular Spaces in Brain MRI," *Procedia Computer Science*, vol. 90, pp. 9-14, 2016
- [155] R. M. Haralick, "Statistical and structural approach to texture," *Proceedings of the IEEE*, vol. 67, no. 5, pp. 786 - 804, 1979.

-
- [156] D. Glotsos, J. Tohka, P. Ravazoula, D. Cavouras and G. Nikiforidis, "Automated diagnosis of brain tumours Astrocytomas using probabilistic neural network clustering and support vector machines," *International Journal of Neural Systems*, vol. 15, no. 1-2, pp. 1-11, 2005.
- [157] H. Selvaraj, S. T. Selvi, D. Selvathi and L. Gewali, "MRI slices classification using least squares support vector machine," *International Journal of Intelligent Computing in Medical Sciences and Image Processing*, vol. 1, pp. 21-33, , 2009.
- [158] A. Kharrat, K. Gashmi, M. B. Messaoud, N. Benamrane and M. Abid, "A Hybrid Approach for Automatic Classification of Brain MRI using genetic algorithm and support vector machine," *Leonardo Journal of Sciences*, vol. 17, no. 1, pp. 71-82, 2010 .
- [159] S. N. Deepa and B. A. Devi, "Second order sequential minimal optimization for brain tumor classification," *European Journal of Scientific Research*, vol. 64, pp. 377-386, 2011.
- [160] E.I. Zacharaki, S. Wang, S. Chawla, D. S. Yoo, R. Wolf, E. R. Melhem and C. Davatzikos, "Classification of brain tumor type and grade using MRI texture in a Machine Learning technique," *Magnetic Resonance in Medicine*, vol. 62, pp. 1609-1618, 2009.
- [161] P. Georgiadiis, D. Cavouras, I. Kalatzis, A. Daskalakis, G. C. Kagadis, M. Malamas, G. Nikiforidis and E. Solomou, " Non-linear least square feature transformations for improving the performance of probabilistic neural networks in classifying human brain tumors on MRI," *Lecture Notes on Computer Science*, vol. 4707, pp. 239-47, 2007.
- [162] P. Georgiadiis, D. Cavouras, I. Kalatzis, A. Daskalakis, G. Kagadis, K. Sifaki, M. Malamas, G. Nikiforidis and E. Solomou, "Improving brain tumor characterization on MRI by probabilistic neural networks and non-linear transformation of textural features," *Comput Methods Programs Biomed*, vol. 89, no. 1, pp. 24-32, Jan 2008.
- [163] S. H. Kim, J. M. Lee, K. G. Kim, J. H. Kim, J. Y. Lee, J. K. Han and B. I. Choi, "Computer aided image analysis of focal hepatic lesions in ultrasonography: preliminary results," *Abdominal Imaging*, vol. 34, no. 2, pp. 183-191 , 2009.
- [164] D. Sheet, H. Garud, A. Suveer, M. Mahadevappa and J. Chatterjee, "Brightness Preserving Dynamic Fuzzy Histogram Equalization," *IEEE Transactions on Consumer Electronics*, vol. 56, no. 4, pp. 2475-2480 , 2010.
- [165] A. P. Dhawan, Y. Chitre and C. Kaiser-Bonasso, "Analysis of mammographic microcalcifications using gray-level image structure features," *IEEE Transactions on Medical Imaging*, vol. 15, no. 3, pp. 246-259, 1996.

-
- [166] V. Khare, J. Santosh, A. Sneh and M. Bhatia, "Performance comparison of neural network training methods based on wavelet packet transform for classification of five mental tasks", *Journal of Biomedical Science and Engineering*, vol.3, pp.612-617, 2010.
- [167] V. Khare, J. Santhosh, J. and A. Sneh, "Performance Comparison using Two ANN Methods for Classification of EEG signals," *International Conference on signal processing Communication & Networking, Chennai*, Jan 4-6, 2008.
- [168] T. Ojala, M. Pietikainen and T. Maenpaa, "Multiresolution gray-scale and rotation invariant texture classification with local binary patterns," *IEEE Transactions on Pattern Analysis and Machine Intelligence*, vol. 24, no. 7, pp. 971 - 987, 2002.
- [169] T. Ahonen, A. Hadid and M. Pietikainen, "Face description with local binary patterns: Application to face recognition," in *IEEE Transactions on Pattern Analysis and Machine Intelligence*, Finland, 2006.
- [170] T. Ahonen, J. Matas, C. He and M. Pietikäinen, "Rotation invariant image description with local binary pattern histogram Fourier features," in *Proceedings: Sixteenth Scandinavian Conference on Image Analysis (SCIA 2009)*, Oslo, Norway, Lecture Notes In Computer Science, pp. 55-75, 2009.
- [171] G. Zhao and M. Pietikainen, "Dynamic texture recognition using local binary patterns with an application to facial expressions," *IEEE Transactions on Pattern Analysis and Machine Intelligence*, vol. 29, no. 6, pp. 915-928, 2007.
- [172] A. Oliver, X. Lladó, J. Freixenet and J. Martí, "False positive reduction. in mammographic mass detection using local binary patterns," in *Medical Image Computing and Computer-Assisted Intervention (MICCAI), Lecture Notes in Computer Science*, vol.1 , pp. 286-293, 2007.
- [173] D. Unay and A. Ekin, "Intensity versus texture for medical image search and retrieval," in *2008 5th IEEE International Symposium on Biomedical Imaging: From Nano to Macro*, 2008.
- [174] S. Liao, M. W. K. Law and A. C. S. Chung, "Dominant local binary patterns for texture classification," *IEEE Transactions on Image Processing*, vol. 18, no. 5, pp. 1107-1118, 2009.
- [175] F. Bianconi, A. Fernandez, "Evaluation of the effects of Gabor filter parameters on texture classification," *Pattern Recognition*, vol. 40, pp. 14-16, 2007.
- [176] M. Kyperountas, A. Tefas and I. Pitas, "Salient feature and reliable classifier selection for facial expression classification," *Pattern Recognition*, vol. 43, no. 3, pp. 972-986, 2010.

-
- [177] S. R. Nirmala, S. Dandapat and P. K. Bora, "DTCWT based blood vessel extraction in retinal image analysis," *International journal of Biomedical Engineering and Consumer Health Informatics (IJBECHI)*, vol. 3, no. 1, pp. 1-5, 2011.
- [178] D. Clausi and H. Deng, "Fusion of Gabor filter and co-occurrence probability features for texture recognition," *IEEE Transactions on Image Processing*, vol. 14, no. 7, pp. 925-936, 2005.
- [179] D. P. Mital, "Texture segmentation using Gabor filter", in *Proceedings: Fourth International Conference on Knowledge-Based Intelligent Systems and allied Technologies*, vol.1, pp. 109-112, 2000.
- [180] J. A. R. Recio, L. A. R. Fernández and A. F. sarriá, "Use of Gabor filters for texture classification of digital images," *Fisica de la Tierra*, vol. 17, pp. 47-59, 2005.
- [181] D. Zhang, A. Wong, M. Indrawan-Santiago and G. Lu, "Content-based image retrieval using Gabor texture features," in *Proceedings: IEEE Pacific Rim Conference on Multimedia*, pp. 392-395, 2000.
- [182] B. S. Manjunath and W. Y. Ma, "Texture features for browsing and retrieval of image data," *IEEE Transactions on Pattern Analysis and Machine Intelligence*, vol. 18, no. 8, pp. 837-842, 1996.
- [183] M. M. R. Krishnan, P. Shah, A. Choudhary, C. Chakraborty, R. R. Paul and A. K. Ray, "Textural characterization of histopathological images for oral sub-mucous fibrosis detection," *Tissue and Cell*, vol. 43, no. 5, pp. 318-330, 2011.
- [184] S. Herlidou, Y. Rolland, J. Bansard, E. L. Rumeur and J. d. Certaines, "Comparison of automated and visual texture analysis in MRI: characterization of normal and diseased skeletal muscle," *Magn Reson Imaging*, vol. 17, no. 9, pp. 1393-1397, Nov 1999.
- [185] S. Murala and Q. M. J. Wu, "Local ternary co-occurrence patterns: A new feature descriptor for MRI and CT image," *Neurocomputing*, vol. 119, no. 7, pp. 399-412, November 2013.
- [186] S. Li, H. Wu, D. Wan and J. Zhu, "An effective feature selection method for hyperspectral image classification based on genetic algorithm and support vector machine," *Knowledge-Based Systems*, vol. 24, no. 1, pp. 40-48, 2011.
- [187] H Guo and A K Nandi, "Breast cancer diagnosis using genetic programming generated feature", *Pattern Recognition*, vol. 39, no.5, pp. 980-987, 2006.
- [188] M. L. Raymer, W. F. Punch, E. D. Goodman, L. A. Kuhn and A. K. Jain, "Dimensionality reduction using genetic algorithms," *IEEE Transactions on Evolutionary Computation*, vol. 4, no. 2, pp. 164-171, 2000.

-
- [189] H. Frohlich, O. Chapelle and B. Scholkopf, "Feature selection for support vector machines by means of genetic algorithms," in *Proceedings: Fifteenth IEEE International Conference on Tools With Artificial Intelligence*, Sacramento, CA, USA, pp. 142-148, 2003.
- [190] V. Jain and J. S. Saharnbi, "Neural Network and Wavelets in Arrhythmia Classification", *Lecture Notes in Computer Science*, vol. 3285, pp. 92-99, 2004.
- [191] L. Wiskott, J. M. Fellous, N. Krüger and C. V. D. Malsburg, "Face Recognition by Elastic Bunch Graph Matching," *IEEE transactions on pattern analysis and Machine Intelligence*, vol. 19, no. 7, pp. 775-779, 1997.
- [192] S. Buchala, N. Davey, T. M. Gale and R. J. Frank, "Analysis of linear and non-linear dimensionality reduction methods for gender classification of face images," *International Journal of systems and Science*, vol 36, no.14, pp.931-942, 2005.
- [193] Y. Zhang and L. Wu," An MR images classifier via principle component analysis and kernel support vector machine," *Progress in electromagnetics Research*, vol 130, pp.369-388, 2012.
- [194] U. Sinha and H. Kangarloo, "Principal Component Analysis for Content-based Image Retrieval," *Radio Graphics*, vol. 22, no. 5, pp. 1271-1289, 2002.
- [195] M. Jafari and S. Kasaei, "Automatic brain tissue detection in MRI images using seeded region growing segmentation and neural network classification," *Australian Journal of Basic and Applied Sciences*, vol. 8, pp. 1066-1079, 2011.
- [196] G. Alexe, G. S. Dalgin, S. Ganesan, C. DeLisi and G. Bhanot, "Analysis of breast cancer progression using principal component analysis and clustering," *Journal of Biosciences*, vol. 32, no. 1, p. 1027–1039, 2007.
- [197] D. Kumar and P Unikrishnan, "Class Specific Feature Selection for Identity Validation using Dynamic Signatures," *J Biomet Biostat 4: 160. doi:10.4172/2155-6180.1000160*
- [198] H. Peng, F. Long and C. Ding, "Feature selection based on mutual information criteria of max-dependency, max-relevance and min-redundancy," *IEEE transactions on pattern analysis and machine intelligence*, vol27, no.8, 1226-1238, 2005.
- [199] G. Chandrashekar and F. Sahin, "A survey on feature selection methods," *Computers and electrical engineering*, vol.40, no.1, pp. 16-28, 2014.
- [200] E. Niaf, O. Rouviere, F. Mege-Lechevallier, F. Bratan and C. Lartizien, "Computer aided diagnosis of prostate cancer in peripheral zone using multiparametric MRI," *Physics in Medicine and Biology*, vol. 57, no. 12, pp. 3833-3851, 2012.

-
- [201] J. Ding, H. Cheng, C. Ning, J. Huang and Y. Zhang, "Quantitative measurement for thyroid cancer characterization based on elastography," *Journal of Ultrasound in medicine*, vol. 30, no. 9, pp. 1259-1266, 2011.
- [202] W. Gomez, W. C. A. Pereira and A. F. C. Infantosi, "Analysis of co-occurrence texture statistics as a function of gray-level quantization for classifying breast ultrasound," *IEEE transactions on Medical Imaging*, vol. 31, no. 10, pp. 1889-1899, 2012.
- [203] A. Balodi, M. L. Dewal, R. S. Anand and A. Rawat, "Texture based classification of the severity of mitral regurgitation," *Computers in Biology and Medicine*, vol. 73, no. 1, pp.157-164, 2016.
- [204] R. Cuingnet, J. A. Glaunès, M. Chupin, H. Benali and O. Colliot, "Spatial and Anatomical Regularization of SVM: A General Framework for Neuroimaging Data," *IEEE Transactions on Pattern Analysis and Machine Intelligence*, vol. 35, no. 3, pp. 682-696, 2013.
- [205] G. Deshpande, P. Wang, D. Rangaprakash and B. Wilamowski, "Fully Connected Cascade Artificial Neural Network Architecture for Attention Deficit Hyperactivity Disorder Classification From Functional Magnetic Resonance Imaging Data," *IEEE Transactions on Cybernetics*, vol. 45, no. 12, p. 2668–2679, 2015.
- [206] Mahima and N. B. Padmavathi, in International Conference on Intelligent Computing, Instrumentation and Control Technologies (ICICICT), Kannur,India, 2018.
- [207] M.W. Aslam, Z. Zhu and A. K. Nandi, "Automatic modulation classification using combination of genetic programming and KNN," *IEEE Transaction on Wireless Communications*, 11 (8). pp. 2742 - 2750. ISSN: 1536-1276, 2012
- [208] R. K. Tripathy and S. Dandapat, "Detection of Cardiac Abnormalities from Multilead ECG using Multiscale Phase Alternation Features," *Journal of Medical Systems*, Vol. 40, No. 6, April 2016.
- [209] H.L. Shashidhara and V. M. Gadre, "Neural Network Based Model for Function Learning," in *Proceedings of Seventh International Conference on Advances in Computing and Communications ADCOM'99*, pp.200-205, December 1999.
- [210] C. I. Christodoulou, C. S. Pattichis, M. Pantziaris, and A. Nicolaidis, "Texture based classification of atherosclerotic carotid plaques," *IEEE Transactions on Medical Imaging*, vol. 22, no. 7, pp. 902-912, 2003.
- [211] C. Cortes and V. Vapnik, "Support-vector networks," *Machine Learning*, vol. 20, no. 3, pp. 273-297, 1995.

-
- [212] M. C. Lee and S. J. Nelson, "Supervised pattern recognition for the prediction of contrast-enhancement appearance in brain tumors from multivariate magnetic resonance imaging in spectroscopy," *Artificial Intelligence in Medicine*, vol. 43, no. 1, pp. 61-74, 2008.
- [213] A. Devos, L. Lukas, J. A. K. Suykens, L. Vanhamme, A. R. Tate, F. A. Howe, C. Majós, A. Moreno-Torres, M. V. Graaf, C. Arús and S. V. Huffel, "Classification of brain tumours using short echo time 1H MR spectra," *Journal of Magnetic Resonance*, vol. 170, no. 1, pp. 164-175, 2004.
- [214] Z. Li, H. Suk., D. Shen and L. Li, "Sparse Multi-Response Tensor Regression for Alzheimer's Disease Study With Multivariate Clinical Assessments," *IEEE Transactions on Medical Imaging*, vol. 35, no. 8, pp. 1927-1936, 2016.
- [215] Q. Wang, E. K. Liacouras, E. Miranda, U. S. Kanamalla and V. Megalooikonomou, "Classification of brain tumors using MRI and MRS," *In proceedings: The SPIE Conference on Medical Imaging*, 2007.
- [216] Y. D. Cho, G. H. Choi, S. P. Lee and J. K. Kim, "1H-MRS metabolic patterns for distinguishing between meningiomas and other brain tumors," *Magnetic Resonance Imaging*, vol. 21, no. 6, pp. 663-672, 2003.
- [217] E. A. El-Dahshan, T. Hosny, A. Badeeh and M. Salem, "Hybrid MRI techniques for brain image classification," *Digital Signal Processing*, vol. 20, pp. 433-441, 2009.
- [218] R. N. Al-Okaili, J. Krejza, J. H. Woo, R. L. Wolf, D. M. Rourke, K. D. Judy, H. Poptani and E. R. Melhem, "Intra-axial brain masses: MR imaging based diagnostic strategy initial experience," *Radiology*, vol. 243, no. 2, pp. 539-550, 2007.
- [219] G. Z. Li, J. Yang, C. Z. Ye and D. Y. Geng, "Degree prediction of malignancy in brain glioma using support vector machines," *Computers in Biology and Medicine*, vol. 36, no. 3, pp. 313-325, 2006.
- [220] P. V. Henstock and D. M. Chelberg, "Automatic gradient threshold determination for edge detection," *IEEE Transactions on Image Processing*, vol. 5, no. 5, pp. 784 - 787, 1996.
- [221] T. Acharya and A. K. Ray, *Image segmentation in image processing*, A John Wiley & Sons MC Publication, 2005, pp. 131-156.
- [222] W. Wang, L. Zhu, J. Qin, Y. P. Chui, B. N. Li and P. A. Heng, "Multiscale geodesic active contours for ultrasound image segmentation using speckle reducing anisotropic diffusion," *Optics and Lasers in Engineering*, vol. 54, pp. 105-116, 2014.

-
- [223] H. D. Cheng, J. Shan, W. Ju, Y. Guo and L. Zhang, "Automated breast cancer detection and classification using ultrasound images: A survey," *Pattern Recognition*, vol. 43, no. 1, pp. 299-317, 2010.
- [224] A. A. Farag, "Edge-based image segmentation," *Remote Sensing Reviews*, vol. 6, no. 1, pp. 95-121, 1992.
- [225] J. M. S. Prewitt, "Object enhancement and extraction," *Picture Processing and Psychopictorics*, vol. 10, no. 1, pp. 15-19, 1970.
- [226] I. Sobel, "Neighborhood coding of binary images for fast contour following and general binary array processing," *Computer Graphics and Image Processing*, vol. 8, no. 1, pp. 127-135, 1978.
- [227] W. K. Pratt, *Digital Image Processing*, John Wiley & Sons Inc, 2006.
- [228] J. F. Canny, "Finding Edges and Lines in Images," *Massachusetts Inst of Technical Report*, vol. 1, 1983.
- [229] C. M. Chou, Y. H. Chou, K. C. Han, G. S. Hung, C. M. Tiu, H. J. Chiou and S. Y. Chiou, "Breast lesions on sonograms: computer-aided diagnosis with nearly setting independent features and artificial neural networks," *Radiology*, vol. 226, no. 2, pp. 504-514, 2003.
- [230] C. C. Chu and J. K. Aggarwal, "The integration of image segmentation maps using region and edge information," *IEEE Transactions on Pattern Analysis and Machine Intelligence*, vol. 15, no. 12, pp. 1241-1252, 1993.
- [231] H. S. Bhadauria and M. L. Dewal, "Intracranial hemorrhage detection using spatial fuzzy c-mean and region-based active contour on brain CT imaging," *Signal, Image and Video Processing*, vol. 8, no. 2, pp. 357-364, 2014.
- [232] Q. Li, J. You, L. Zhang and P. Bhattacharya, "A multiscale approach to retinal vessel segmentation using gabor filters and scale multiplication," in *IEEE International Conference on Systems Man and Cybernetics*, pp. 3521-3527, 2006.
- [233] M. Rastgarpour, J. Shanbehzadeh and H. S. Zadeh, "A Hybrid Method Based on Fuzzy Clustering and Local Region-Based Level Set for Segmentation of Inhomogeneous Medical Image," *Journal of Medical Systems*, vol. 38, no. 8, pp. 1-15, 2014.
- [234] H. Zheng and O. Hellwich, "Discrete regularization for perceptual image segmentation via semi-supervised learning and optimal control," in *IEEE International Conference on Multimedia and Expo*, pp. 1982-1985, 2007.
- [235] S. Kichenassamy, A. Kumar, P. Olver, A. Tannenbaum and A. Y. Jr, "Conformal curvature flows: From phase transitions to active vision," *Archive for Rational Mechanics and Analysis*, vol. 134, no. 3, pp. 275-301, 1996.

-
- [236] L. D. Cohen, "On active contour models and balloons," *CVGIP: Image Understanding*, vol. 53, no. 2, pp. 211-218, 1991.
- [237] L. D. Cohen and I. Cohen, "Finite-element methods for active contour models and balloons for 2-D and 3-D images," *IEEE Transactions on Pattern Analysis and Machine Intelligence*, vol. 15, no. 11, pp. 1131-1147, 1993.
- [238] B. Leroy, I. L. Herlin and L. D. Cohen, Multi-resolution algorithms for active contour models, vol. 219, Lecture Notes in Control and Information Sciences M O Berger;R. Deriche;l. Harlin;J Jaflré;J M Morel, Springer Berlin Heidelberg, pp. 58-65, 1996.
- [239] S. Kichenassamy, A. Kumar, P. Olver, A. Tannenbaum and A. Yezzi, "Gradient flows and geometric active contour models," in *Proceedings of IEEE International Conference on Computer Vision*, pp. 810-815, 1995.
- [240] X. F. Wang, D. S. Huang and H. Xu, "An efficient local Chan-Vese model for image segmentation," *Pattern Recognition*, vol. 43, no. 3, pp. 603-618, 2010.
- [241] V. Caselles, F. Catté, T. Coll and F. Dibos, "A geometric model for active contours in image processing," *Numerische Mathematik*, vol. 66, no. 1, p. 1–31, 1993.
- [242] A. Tsai, A. Jr. Yezzi and A. S. Willsky, "Curve evolution implementation of the Mumford-Shah functional for image segmentation, denoising, interpolation and magnification," *IEEE Transactions on Image Processing*, vol.10, no.8, pp.1169-1186, 2001.
- [243] L. Wang, L. He, A. Mishra and C. Li, "Active contours driven by local Gaussian distribution fitting energy," *Signal Processing*, vol. 89, no. 12, pp. 2435-2447, 2009.
- [244] F. Morain-Nicolier, S. Lebonvallet, E. Baudrier and S. Ruan, "Hausdorff Distance based 3D Quantification of Brain Tumor Evolution from MRI Images," in *Proceedings of the 29th Annual International Conference of the IEEE EMBS Cité Internationale*, Lyon, France, pp. 5597-5600, 2007.
- [245] D. Gupta, R.S. Anand and B. Tyagi, "A hybrid segmentation method based on Gaussian kernel fuzzy clustering and region based active contour model for ultrasound medical images," *Biomedical Signal Processing and Control*, vol. 16, pp. 98-112, 2015.
- [246] J.E. Wilhjelm, M. L. Gronholdt, B. Wiebe, S. K. Jespersen, L. K. Hansen and H. Sillesen, "Quantitative analysis of ultrasound B-mode images of carotid atherosclerotic plaque: correlation with visual classification and histological examination," *IEEE Trans. Med. Imaging*, vol. 17, pp. 910-922, 1998.

-
- [247] J. S. Weszka, C.R. Dyer and A. Rosenfeld, "A comparative study of texture measures for terrain classification," *IEEE transactions on Systems, Man and Cybernetics*, vol. SMC-6, no.4, pp. 269-255, 1976.
- [248] M. Amadasun and R. King, "Textural features corresponding to textural properties," *IEEE transactions on Acoustics Speech and Signal Processing*, vol.19, no. 5, pp.1264-1274, 1989.
- [249] K. I. Laws, "Rapid Texture identification," in *24th annual Technical Symposium o. International Society for Optics and Photonics*, pp. 376-381, 1980.
- [250] B. B. Mandelbrot, *The Fractal Geometry of Nature*, Macmillan, vol.173, 1983.
- [251] E. H. Adelson, C. H. Anderson, J. R. Bergen, P. J. Burt and J. M. Ogden, "Pyramid methods in image processing," *RCA Engineer*, vol.29, no. 6, pp. 33-41, 1984.
- [252] C. P. Loizou, C. S. Pattichis, C. I. Christodoulou, R. S. H. Istepanian, M. Pantziaris and A. Nicolaidis, "Comparative evaluation of despeckle filtering in ultrasound imaging of the carotid artery," *IEEE Trans. Ultrason. Ferroelectr. Freq. Control*, vol. 52, pp. 1653–1669, 2005.
- [253] J. Liang, S. Yang and A. Winstanley, "Invariant optimal feature selection: A distance discriminant and feature ranking based solution," *Pattern Recognition*, vol.41, no.5, pp.1429–1439, 2008.
- [254] "Classify patterns with a neural network, available: <http://in.mathworks.com/help/nnet/gs/classify-patterns-with-a-neural-network.html>."

APPENDIX

Table A.1: Averaged performance measures (TP, FP, ACC, JSI, DC and HD) evaluated for the proposed MRBAC segmentation scheme applied on Tumor MRI, Infarct MRI and hemorrhage MRI of brain

MRBAC Method	TP (AVG \pm STD)	FP (AVG \pm STD)	ACC (AVG \pm STD)	JSI (AVG \pm STD)	DC (AVG \pm STD)	HD (AVG \pm STD)
MRBAC_T	0.926 \pm 0.026	0.032 \pm 0.012	0.947 \pm 0.015	0.898 \pm 0.030	0.946 \pm 0.017	3.248 \pm 0.806
MRBAC_I	0.856 \pm 0.096	0.102 \pm 0.095	0.883 \pm 0.037	0.778 \pm 0.070	0.873 \pm 0.044	2.717 \pm 0.468
MRBAC_H	0.919 \pm 0.053	0.077 \pm 0.043	0.922 \pm 0.012	0.853 \pm 0.024	0.920 \pm 0.014	3.194 \pm 0.443

Where,

- MRBAC_T: Proposed approach on Tumor MRI of brain.
- MRBAC_I: Proposed approach on Infarct MRI of brain
- MRBAC_H: Proposed approach on Hemorrhage MRI of brain.

Table A.2: Averaged performance measures (TP, FP, ACC, JSI, DC and HD) evaluated for the proposed Region Growing segmentation scheme applied on Tumor MRI, Infarct MRI and hemorrhage MRI of brain

Region Growing	TP (AVG \pm STD)	FP (AVG \pm STD)	ACC (AVG \pm STD)	JSI (AVG \pm STD)	DC (AVG \pm STD)	HD (AVG \pm STD)
RG_T	0.904 \pm 0.013	0.036 \pm 0.019	0.933 \pm 0.007	0.873 \pm 0.011	0.932 \pm 0.006	3.653 \pm 1.286
RG_I	0.821 \pm 0.145	0.155 \pm 0.113	0.842 \pm 0.024	0.705 \pm 0.059	0.825 \pm 0.041	3.339 \pm 0.808
RG_H	0.929 \pm 0.053	0.134 \pm 0.077	0.902 \pm 0.015	0.820 \pm 0.023	0.901 \pm 0.014	3.740 \pm 0.465

Where,

- RG_T: Region Growing approach on Tumor MRI of brain
 RG_I: Region Growing approach on Infarct MRI of brain
 RG_H: Region Growing approach on Hemorrhage MRI of brain

Table A.3: Averaged performance measures (TP, FP, ACC, JSI, DC and HD) evaluated for the proposed Region Growing segmentation scheme applied on Tumor MRI, Infarct MRI and hemorrhage MRI of brain

DRLSE Method	TP (AVG \pm STD)	FP (AVG \pm STD)	ACC (AVG \pm STD)	JSI (AVG \pm STD)	DC (AVG \pm STD)	HD (AVG \pm STD)
DRLSE_T	0.802 \pm 0.131	0.023 \pm 0.022	0.887 \pm 0.062	0.783 \pm 0.121	0.873 \pm 0.079	3.647 \pm 0.546
DRLSE_I	0.824 \pm 0.081	0.136 \pm 0.136	0.854 \pm 0.039	0.729 \pm 0.065	0.842 \pm 0.044	2.843 \pm 0.563
DRLSE_H	0.896 \pm 0.074	0.084 \pm 0.060	0.908 \pm 0.021	0.826 \pm 0.042	0.904 \pm 0.025	3.581 \pm 0.881

Where,

- DRLSE_T: DRLSE approach on Tumor MRI of brain.
- DRLSE_I: DRLSE growing approach on Infarct MRI of brain
- DRLSE_H: DRLSE approach on Hemorrhage MRI of brain.

Table A.4: Comparative performance of segmentation approach with averaged number of iteration and averaged computational time for all MR brain images

Methods	Averaged resolution	Averaged Iterations	Averaged computation time (s)
Region Growing	256x256	236	20.41
DRLSE	256x256	278	24.64
Proposed MRBAC	256x256	190	16.69